Iterative Learning Control Strategies for Robot-aided Ankle Rehabilitation

Qian Kun

University of Leeds

School of Electronic and Electrical Engineering

Submitted in accordance with the requirements for the degree of

Doctor of Philosophy

March, 2022

Intellectual Property Statement

The candidate confirms that the work submitted is his own and that appropriate credit has been given where reference has been made to the work of others.

Acknowledgements

First of all, I would like to express my deepest gratitude to my supervisor, Professor Shane Xie, who has kept inspiring me to explore far beyond my own expectation. It has always been an enjoyable experience to do researches under Professor Xie's supervision, and he has an outstanding track record in the field of rehabilitation robotics. He has always taught me to strive for a single goal, this inspired me throughout my whole research. He provided me with a good research platform, encouraged me to attend international conferences and helped me to network with leading researchers around the world, which were invaluable experiences and broadened my vision.

I would like to express my gratitude to Associate Professor Zhiqiang Zhang, and Doctor Samit Chakrabarty, who are the co-members of my supervision team. They have provided me invaluable advices and consistent assistance through all stages of my research. Special thanks to their helps on preparing and revising my thesis.

My sincere gratitude goes to the UoL Graduate School and the Institute of Robotics, Autonomous Systems and Sensing (IRASS) for providing me with a great opportunity to pursue my Ph.D. degree. I also want to thank Ms. Louise Coffey, the administrator of the IRASS, for her help and patience on handling tedious paper work for me.

My sincere gratitude and respect go to research fellows in our group, Zhenhong Li and Ahmed Asker, for their advices and help through the four years of my research study. Special thanks to Dr. Li for his guidance in control theory, he is undoubtedly the future leader in this field. My thanks goes to my dear fellow colleagues, Yihui Zhao, Yue Zhang, Tianzhe Bao, Chao Wang, Orla Gilson and Asma Alzaid. Without them I would not have had such a vivid Ph.D. life.

At last but not least, I give my dearest gratitude to my family, especially my parents, who have given me a life to live on and the freedom to pursue my dream. I have owed them so much that I could not pay back in a lifetime. Thank you to all those who helped me during this wonderful four years journey.

I am because you are.

Qian Kun

Leeds, 2021

Abstract

The human ankle plays an important role in daily activities, but it and its actions are vulnerable to physical and neurological injuries. Physiotherapy is labour-intensive and time-consuming, in consequence, the use of robotics to aid ankle rehabilitation has attracted increasing attention. However, currently, robotic equipment is merely an adjunct to the therapist and its automation capability is underutilized. The main technical barrier is that existing control strategies for ankle rehabilitation robots are lack learnability and adaptability, while requiring continuous supervision and guidance from the therapist. By the repetitive nature of the rehabilitation scenario, this thesis aims to propose training strategies based on iterative learning control (ILC) to improve the effectiveness of use of robots in ankle rehabilitation.

To deliver comprehensive ankle treatment, a compliant ankle rehabilitation robot (CARR) is first proposed to provide three-dimensional movements. The usage of soft pneumatic muscle (PM) allows compliant actuation, but also bring difficulties to controller design. To cope with the modelling difficulty of PM, the dynamic linearization approach is introduced and a data-driven adaptive ILC is proposed for precise ankle ranges of motion (ROMs) training. The performance degradation of the conventional ILC scheme is resolved and transient learning behaviour is guaranteed. The tracking accuracy of the CARR has an average improvement of 8.27%, validated experimentally. Subsequently, considering the training safety and the control robustness, a novel ILC scheme is proposed that conjointly solves state constraints, parametric and nonparametric uncertainties of PM. Experiments on the CARR with comparisons to conventional ILC schemes illustrate its efficacy in guaranteeing predefined ROM bounds, and the tracking accuracy is improved by 2.5% for a single PM configuration. After training the ROMs, interactive exercises are essential for rebuilding ankle strength. To tackle the time-varying property of the human ankle, the impedance learn-

ing scheme and the force distribution based torque controller are designed to improve the interaction performance. Compared to conventional impedance control, the task completion is improved by 8% after five repetitions and compliant robot motion is retained. Furthermore, to comprehensively assess the subject's recovery, fuzzy logic is established for online performance evaluation during training. Subsequently, a progressive learning scheme is introduced that modifies the CARR stiffness in accordance with patient-specific evaluations and encourages patients' engagements. By maintaining the decreasing tendency of the CARR stiffness, the average increase of patients' active participation is 62% during experimental studies.

Towards the effectiveness of employing ILC control strategies for robot-aided ankle rehabilitation, this thesis provides profound insights with experimental validations. During passive ROMs training, proposed ILC schemes tackle the modelling difficulty, state constraints and uncertainties that are applicable to soft actuators with analogous characteristics. As the first to design the impedance learning controller and reproduce progressive training strategies for ankle rehabilitation, preliminary results given in this thesis illustrate its feasibility and substantial potential. In conclusion, the ILC training strategies proposed in this thesis are a cornerstone for the realization of full-automatic robot-assisted ankle rehabilitation.

Contents

List of Figures

List of Tables

Abbreviations

D/P	Dorsiflexion/Plantarflexion
I/E	Inversion/Eversion
A/A	Adduction/Abduction
DoFs	Degrees of Freedom
ROMs	Ranges of Motion
ARR	Ankle Rehabilitation Robot
PD	Proportional-Derivative
PID	Proportional-Integral-Derivative
PM	Pneumatic Muscle
IFT	Iterative Feedback Tuning
HRI	Human-Robot-Interaction
CARR	Compliant Ankle Rehabilitation Robot
ILC	Iterative Learning Control
P/D-ILC	Proportional/Derivative-type ILC
SEA	Series Elastic Actuator
DO	Disturbance Observer
FES	Functional Electrical Stimulation
sEMG	Surface Electromyography
I/O	Input/Output
RMSE	Root-Mean-Square-Error

Chapter 1

Introduction

The human ankle joint is one of the most complicated structures in the human body that plays a vital role in support, balance and ambulation [13]. Numerous factors can cause ankle dysfunction and/or limited range of motion (ROM). For instance, overweight, excessive physical activity or a lack of it for seniors, together with congenital lesions and traumatic injuries make the ankle joint one of the most common injured joints in the human body [14]. Sprains are one of the most frequent ankle pathologies, according to National Health Service (NHS) report, there are an estimated 5000 cases a day in the United Kingdom (UK) [15]. Also, over 1.2 million stroke survivors are suffering from hemiplegia and permanent ankle dysfunction across the UK [16]. Without proper recovery, more than 30% of patients will develop various sequelae within three years that affect their motor functions and daily activities [17].

Conventional physiotherapy brings a great burden that long-term efforts are required from both therapists and patients. Meanwhile, training tasks are usually of extensive repetitions and different inducements of injuries make the ankle rehabilitation process long and tortuous [18]. A genuine interest, motivated by the rapid development of robot technologies, has been explored in the design and creation of robotic devices that assist physiotherapy [19]. To largely mimic therapists' operation and deliver effective rehabilitation outcomes, one of the underlying problems is to design appropriate control strategies for robotic devices under different phases of ankle rehabilitation. To start with, this chapter introduces the ankle anatomy, physiotherapy procedures, the proper ankle robot construction and research issues encountered in the course of designing therapist-resembled control strategies for robot-aided ankle rehabilitation. Alongside, the thesis structure and outlines of each chapter are given.

1.1 Ankle Joint Complex

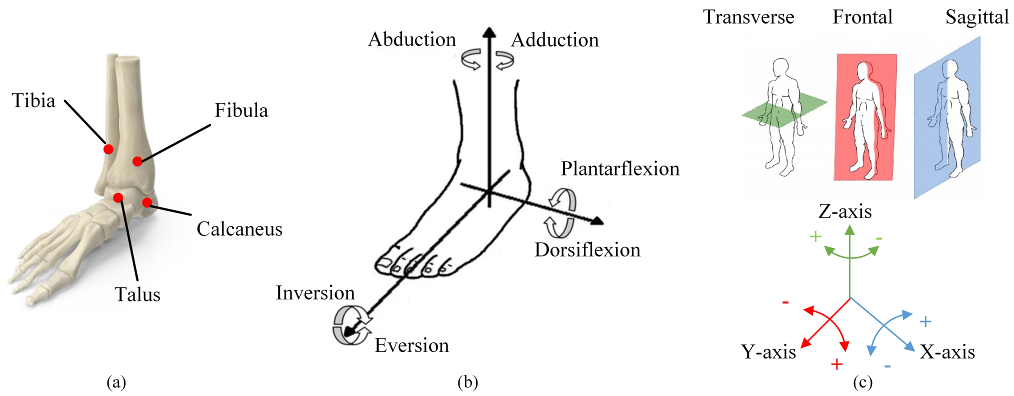

Figure 1.1: Ankle complex anatomy with its rotations. (a) Ankle complex anatomy; (b) Three DoFs [1]; (c) Corresponding anatomical planes and directions [2, 3].

The ankle joint complex consists of the tibia, fibula, talus and calcaneus, as shown in Figure 1.1(a). The commonly referred term “ankle joint” is the articulation between the tibia-fibula unit and the talus. Together with the subtalar joint located between the talus and the calcaneus, the term “ankle” in this thesis encompasses both the ankle joint and subtalar joint, is primarily rotational, and is often described by rotations on three mutually perpendicular anatomical planes. The rotations that occur in the sagittal, frontal and transverse plane are dorsiflexion/plantarflexion (D/P), inversion/eversion (I/E) and adduction/abduction (A/A), respectively. The above-mentioned degrees of freedom (DoFs) are presented in Figure 1.1(b). As suggested by Wu et al. [3], the ankle rotations are defined as X-axis, Y-axis and Z-axis in the sagittal, frontal and transverse plane, together with its positive and negative directions as shown in Figure

Table 1.1: Ankle ROMs and passive torques adapted from [10] and [11].

Type of Motion	Ankle motions			Maximum PAT (Nm)
	ROM	Mean	SD	
Dorsiflexion	20.3° to 29.8°	24.68°	3.25°	34.1 ± 14.5
Plantarflexion	37.6° to 45.75°	40.92°	4.32°	48.1 ± 12.2
Inversion	14.5° to 22°	16.29°	3.88°	33.1 ± 16.5
Eversion	10° to 17°	15.87°	4.45°	40.14 ± 9.2
Adduction	22° to 36°	29.83°	7.56°	NA
Abduction	15.4° to 25.9°	22.03°	5.99°	NA

PAT: Passive ankle torque; SD: Standard deviation; NA: Not available.

1.1(c). In Table 1.1, the ankle ROMs along three rotation axes are summarized [10] and the maximum passive ankle torques obtained by authors in [11] from 32 humans lower legs are given. These data can be considered as the standard criteria for designing aids for ankle rehabilitation.

1.2 Ankle Rehabilitation and Robot-aided Approach

The procedures of conventional ankle physiotherapy are shown in Figure 1.2. It mainly includes 1) recovery-phase with ROMs training and strength exercises; 2) functional-phase with balance and composite motion practice. During recovery, extensive repetitions of coordinated motor activities should be conducted that constitute a significant burden to the therapist [20]. The development of robotic technology offers an alternative solution, that is, a robot-aided rehabilitation approach. Robotic devices can perform repetitive tasks effectively that avoid the labour-intensive issue and built-in sensors also provide the quantitative real-time assessment. With these merits, an increasing number of ankle rehabilitation robots (ARRs) have been developed to deliver long-term, accurate and standardized rehabilitation training for the ankle. Some representative examples are presented in Figure 1.3.

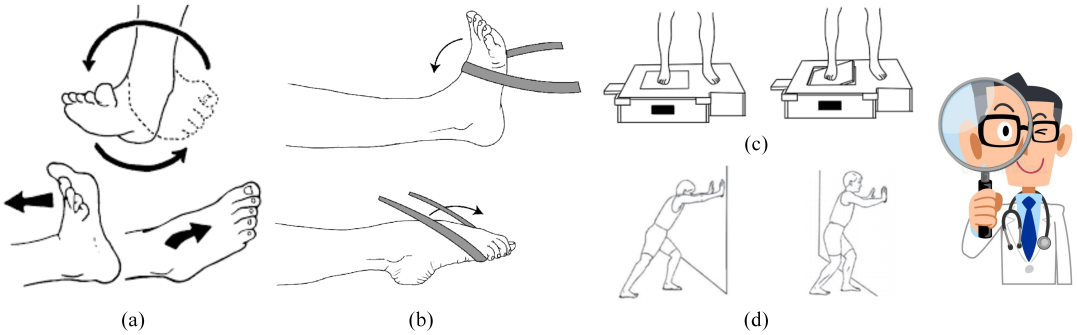

Figure 1.2: Recovery-phase includes [4]: (a) ROM training; (b) Strength exercises with stretch bands. Functional-phase includes: (c) Balance training; (d) Calf involved lower extremity joint stretch.

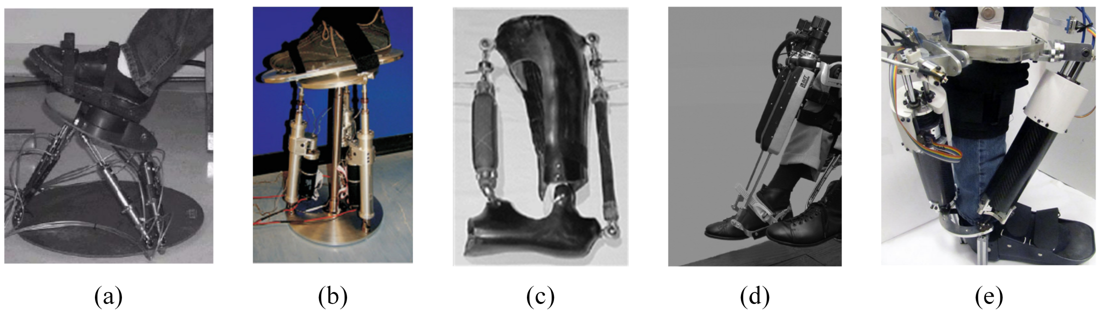

Figure 1.3: ARR examples. (a) Rutgers Ankle [5]; (b) ARBOT [1]; (c) KAFO [6]; (d) Anklebot [7]; (e) AssistOn-Ankle [8]

Based on different rehabilitation purposes, ARRs are mainly divided into two categories: 1) platform-based constructions (Figure 1.3(a) and (b)) that manipulate the ankle with its end effector for single-joint treatments; 2) wearable constructions (Figure 1.3(c)-(e)) that support gait correction and multi-joint exercises. The main advantage of platform-based construction is that isolated movements for single-joint are easier to be learned and therefore have less reliance on neural factors than multiple-joint exercises [21, 22]. However, the rotation centres of existing platform-based ARRs are not aligned with the ankle. Therefore, synergetic movements of the patient's lower extremity are required during training. In contrast, wearable ARRs avoid this problem with reasonable joint configuration. Inheriting the advantages of both constructions, a platform-based ARR with an aligned rotation centre has great potential in robot-aided ankle rehabilitation [23]. To conclude, Figure 1.4 presents the classification of ARRs with relative merits, and the potential research interest is summarized in dash lines.

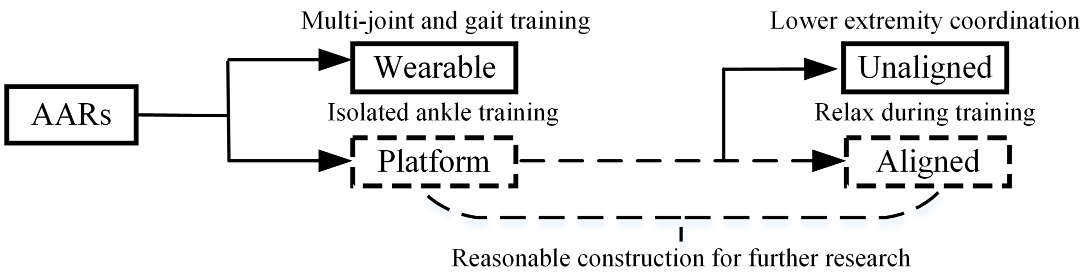

Figure 1.4: Classification of existing AARs and potential research interest (dash lines).

1.3 From Therapist to Robot-aided

During physiotherapy, therapists are manually manipulating patients' ankles to conduct different training tasks. This manipulation has the following features:

- Safety and accuracy: The ROMs of the ankle are predetermined and limited to avoid any possible injuries. Under the measurement of the goniometer, the patient's ankle is manipulated along with such ROMs within a small margin of error [24].
- Patient-specific: Multiple outcome measures, e.g., the goniometer and dynamometer are used by the therapists to assess conditions of ankle strength for different individuals. Subsequently, therapists modify their assistance based on patient-specific recovery state with different training difficulties [25].
- Learnability: After a successful trial, the empirical process can be learned by therapists and used for configuring the follow-on repetitive trials [26]. Meanwhile, clinical tests demonstrate that a series of progressive exercises can promote patients' recovery [27].

Ideally, the robot-aided approach should inherit these features and deliver a therapist-resembled treatment [28]. For this purpose, it is essential to design appropriate control strategies for AARs that establish an efficient transition from therapist to robot-aided training. From the aforementioned features, focuses of advanced ARR control strategies can be summarized as

- During ROMs training, designing trajectory tracking controller that precisely stretches the patient's ankle. Simultaneously, training safety needs to be considered in the controller design for avoiding the possible ankle injury.
- During strength training, the task difficulty should be determined by the level of recovery. Meanwhile, patient-specific control strategies are desired to automatically modify robot assistances for different individuals.
- Allowing incorporation of the repetitive nature of training, advanced control strategies with learning concepts have great potential in rehabilitation scenarios. Besides, it is essential to transfer the progressive training concept into robot-aided approaches.

1.4 Control Strategies of Rehabilitation Training

Up to now, ARRs are mainly intervening ankle rehabilitation process in two ways, passive training and active training, which particularly focus on the recovery-phase (Figure 1.2(a) and (b)). To help patients regain their ankle ROMs, ARRs are required to repetitively manipulate the ankle under a predefined trajectory. Therefore, passive training normally refers to trajectory tracking control. After proper ROMs are restored, muscle strength exercises are conducted to further reinforce patients' motor function [14]. During this stage, the robot assistance is determined by the measurable interactive information. Therefore, active training usually refers to human-robot interaction (HRI) control.

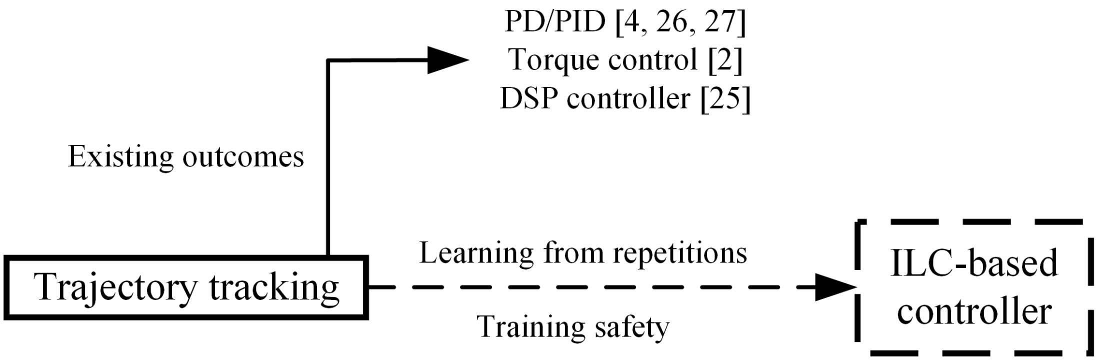

Figure 1.5: Existing outcomes and future development (dash lines) of control strategies for passive ankle training.

1.4.1 Trajectory Tracking Control

During the passive stage, stretching is usually conducted when patients can not autonomously move their ankles. Extensive studies have shown that joint ROM is a vital indicator for functional evaluation and should be the paramount rehabilitation objective [27, 29, 30]. For instance, the Digital Signal Processing (DSP) controller is implemented on an intelligent stretching device [31] and a computed-torque controller is proposed for the ARBOT [1]. Besides, the proportional-derivative (PD) and proportional-integral-derivative (PID) controllers are commonly used in various ARRs for trajectory tracking purposes [7, 32, 33]. However, the aforementioned controllers underuse the repetitive nature of the rehabilitation training. Iterative learning control (ILC), as a superior method for handling the repetitive control process, can gradually enhance the tracking accuracy and is expected to have a better performance [26].

Recently, to enhance training safety, advanced actuators, i.e., pneumatic muscle (PM) and series elastic actuator (SEA), are adopted in ARR developments [8, 34–36]. From a hardware point of view, the compliance and backdrivability of these actuators can provide additional ROMs for the patient's ankle. However, without considering the training safety in the robot controller design, it is still possible for ARRs that drive the patient's ankle to an insecure ROM. To conclude, ILC-based strategies that fully utilize the repetitive nature of ankle ROMs training and ensure the training safety can be regarded as a further research interest, as summarized by dash lines in Figure 1.5.

1.4.2 Human-Robot Interaction Control

After appropriate ROM is regained, passive stretching dominated by the robotic device is inadequate for a comprehensive recovery [37]. As a result, the concept of HRI control strategy is introduced for conducting ankle strength training. As shown in Figure 1.6, the human ankle is considered a plant and controlled by the central nervous system (CNS). For the desired movement, commands are passed to the corresponding muscles via a network of motoneurons. The sensorial information provides feedback that demarcates whether the desired movement is fulfilled or not [38]. However, if the patient has nervous or muscle disorders, the system cannot work properly. With detectable interactive information, the robot-assisted approach can step in (process with dash lines) while providing appropriate assistance if necessary to reshape the system [39].

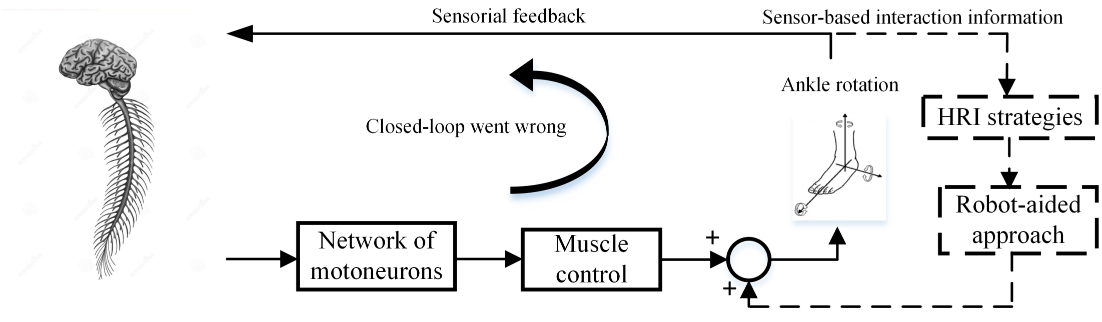

Figure 1.6: Closed-loop of ankle motion [9] and HRI strategy intervention during rehabilitation (dash lines).

The above procedure leads to two major challenges in the design of HRI control strategies for ankle rehabilitation. Firstly, task completion and interaction performance are suggested to be conjointly considered in the active rehabilitation training [40, 41]. However, existing control strategies employ either independent tracking error [42, 43] or interactive information [36, 44] to assess the ankle recovery conditions and

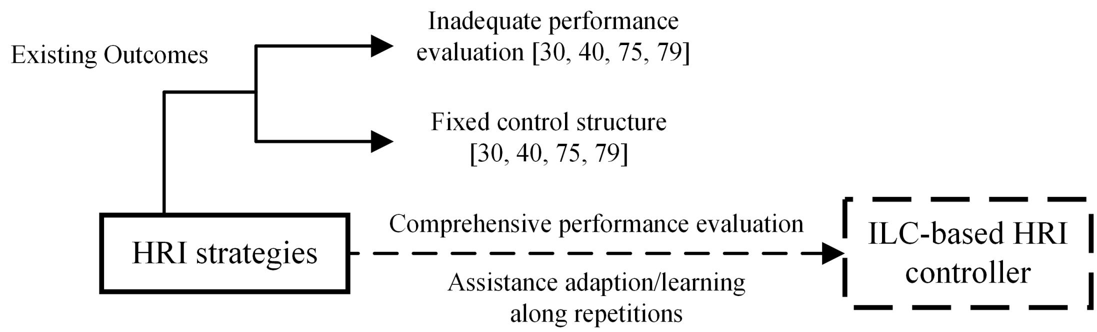

Figure 1.7: Existing outcomes and future development (dash lines) for an optimized HRI control strategy.

modify the robot assistance. Secondary, different from stationary interactive objects, the human ankle has time-varying property and individual differences [45]. Control strategies with fixed parameters [1, 46, 47] are not able to dynamically adjust the robot assistance during repetitive training, which degrades the interaction performance. Therefore, as summarized by dash lines in Figure 1.7, an active control strategy that is able to provide appropriate assistance in the light of comprehensive performance evaluation and ILC-based learning mechanism has further research interest.

1.5 Research Motivations and Objectives

There are four main motivations in developing ARR and designing advanced ILC-based strategies for robot-aided ankle training. Firstly, a felicitously constructed ARR can provide repeatable, isolated and comprehensive ankle training and significantly reduce the therapists' workload. Secondly, passive training can effectively help patients to regain their ankle ROMs while the tracking performance can be enhanced by employing advanced ILC-based schemes. Thirdly, considering system uncertainties and training safety in the controller design can effectively avoid potential injuries of the patient's ankle and improve the control robustness. Lastly, enhanced interaction performance can be gradually achieved via an ILC-based mechanism and patients' engagement can be encouraged by comprehensive performance evaluation and progressive learning-based strategies. As a result, four main objectives of this research are:

1. A novel ARR will be designed to deliver compliant movements for three-dimensional ankle treatment without lower extremity collaborations and obtain real-time feedback of ankle kinematics and dynamics.

2. An advanced ILC scheme will be proposed to gradually enhance the tracking performance with improved transient learning behaviour.

3. A novel ILC scheme will be proposed to guarantee training safety and improve control robustness.

4. Iterative impedance learning will be investigated to handle the time-varying ankle dynamics and improve the interaction performance. Performance-based progressive learning will be proposed to promote patients' engagement based on individual performance evaluation.

1.6 Thesis Outline

This thesis details the work carried out in this research to meet the above objectives. Chapter 3 achieves the first objective with the development of a PM-driven ankle robot prototype. The second objective is achieved by Chapter 4 that proposes a data-driven adaptive ILC scheme for ankle ROMs training. To accomplish the third objective, Chapter 5 establishes a PM dynamic model and Chapter 6 proposes a robust constrained ILC scheme to guarantee the robustness of the controller and the safety of ankle training. The last major objective of this research is the design of an iterative impedance learning scheme and progressive training framework in Chapter 7 and Chapter 8. Specifically, this thesis is organized as follows

Chapter 1 provides an introduction that elaborates the significant demands of ankle rehabilitation and the advantages of incorporating robotic devices. Pointing out that developing proper ARR and designing advanced control strategies are the key to mimicking physiotherapy. In the rehabilitation scenario, ILC is particularly outstanding due to its superiority in handling repetitive control processes. The research objectives are detailed and the thesis outline is presented.

Chapter 2 presents a systematic review regarding the learning-based control strategies for robot-aided ankle rehabilitation. Existing works that adopt learning concepts, e.g., adaptive control, ILC, etc. for conducting both passive and active ankle training are involved. With classification and discussion on different learning-based approaches, ILC shows remarkable performance with some unsolved problems. These open research gaps are summarized and will be addressed in the subsequent chapters.

Chapter 3 introduces the mechanical construction, kinematics and dynamics of a compliant ankle rehabilitation robot (CARR) prototype. The actuated-from-above layout and the usage of four PMs allow the CARR to perform isolated, compliant and comprehensive ankle training. However, PM is a typical soft actuator that contains nonlinearities, unknown parameters and unmodelled uncertainties. The impact of these issues on robot tracking accuracy, training safety and control robustness will be addressed in later chapters.

Chapter 4 proposes a data-driven adaptive iterative learning scheme for conducting ankle ROMs training. Due to the modelling difficulty of PM, a data-driven model is established that only system I/O measures are required. Subsequently, a novel adaptive ILC scheme is proposed to achieve precise tracking and avoid performance degradation. The monotonic tracking error convergence is derived and large learning transients are avoided. Experimental validations on the CARR involve ten healthy participants and control performances are compared with PID and conventional ILC schemes. This chapter contains materials that have been submitted for part of the possible publication as:

- Kun Qian, Zhenhong Li, Wei Meng, Zhiqiang Zhang and Sheng Q. Xie, "Data-driven Adaptive Iterative Learning Control of a Compliant Rehabilitation Robot for Repetitive Ankle Training", IEEE Robotics and Automation Letters. (Major revision)

In addition to modelling difficulty, PM control also suffers from unknown parameters and unmodelled uncertainties. To study these problems, Chapter 5 introduces a phenomenological model for describing PM dynamics. The model uses a three-element form and a self-developed PM platform is constructed for parameter identifications. Validation results indicate that the three-element model can largely represent PM dynamic characteristics, however, the pressure-dependent parameters and unmodelled frictions have to be considered in designing a precise PM tracking controller.

Chapter 6 investigates the robustness of PM state tracking that solves parametric uncertainties and the unmodelled friction based on the three-element model. Besides, for enhanced training safety, state constraints of PM are conjointly considered. A robust constrained ILC scheme is proposed with two ILC laws and an additional robust control part. Through rigorous analysis, state constraints are satisfied, perturbations raised by uncertainties are gradually eliminated and uniform error convergence is guaranteed. Experimental results on the single PM configuration illustrate the efficiency of the proposed scheme and its implementation on the CARR demonstrates its capability of realizing constrained ROM training. This chapter and Chapter 5 contain materials that have been published and have been submitted for part of the possible publication as:

- Kun Qian, Zhenghong Li, Ahmed Asker, Zhiqiang Zhang, and Shengquan Xie, "Robust Iterative Learning Control for Pneumatic Muscle with State Constraint and Model Uncertainty", 2021 IEEE International Conference on Robotics and Automation (ICRA 2021).
- Kun Qian, Zhenhong Li, Samit Chakrabarty, Zhiqiang Zhang and Shengquan

Xie, “Robust Iterative Learning Control for Pneumatic Muscle with Uncertainties and State Constraints”, IEEE Transactions on Industrial Electronics. (Major revision)

Chapter 7 introduces an iterative impedance learning scheme for active ankle training. The unknown ankle dynamic impedance is represented by a linear time-varying (LTV) system. With gradient following and iterative learning scheme, an optimal set of impedance parameters is learned based on a predefined interaction profile. Subsequently, a torque controller with a force distribution algorithm is designed for realizing ankle strength training. The effectiveness of the applied force distribution algorithm is proved in simulation and experiments are conducted with healthy subjects. Compared with a conventional impedance controller with fixed parameters, the impedance learning scheme can gradually improve task completion while maintaining a compliant interaction performance in the presence of ankle passive torque. This chapter contains materials that have been published as:

- Kun Qian, Zhiqiang Zhang, Samit Chakrabarty, and Shengquan Xie, “Iterative Impedance Learning Control for Ankle Rehabilitation”, 2021 International Conference on Mechatronics and Machine Vision in Practice (M2VIP 2021).

Chapter 8 proposes a progressive learning framework for active ankle training. Fuzzy logic is first developed that provides a comprehensive quantitative assessment of patients’ recovery with three sensing indicators. The obtained performance evaluation result is then used to minimize a cost function that consists of the trajectory tracking error and the robot stiffness matrix. Theoretical analysis based on the Lyapunov theory is given and the effect of patient’s performance on the control ultimate bound is discussed. Experiments with ten healthy subjects indicate that reliable and patient-specific performance evaluation can be realized. Moreover, with the progressive learning strategies, active participation will lead to a larger allowable tracking error and lower CARR stiffness matrix that further promotes patients’ engagement.

Chapter 9 summarises the main contributions of this research and provides recommendations for its further development.

1.7 Chapter Summary

Due to the increasing need for ankle rehabilitation, it is significant to develop robot-aided approaches as an effective adjunct for conventional physiotherapy. In this chapter, the ankle anatomy, physiotherapy procedures, robot-assisted approaches, and control strategies are introduced. The main incentives of robot-aided ankle rehabilitation include: 1) reducing the workload of therapists; 2) providing accuracy and safe ROMs training; 3) encouraging the patient's participant to promote recovery. In virtue of the repetitive nature of rehabilitation training, ILC-based control strategies show great potential and will be specified in the next review chapter. The main objectives of this research include: 1) designing novel ARR for effective ankle training; 2) developing advanced ILC scheme for precise ROMs training; 3) enhancing operational safety and control robustness via novel ILC scheme; 4) providing subject-specific training and motivating patients' engagement via ILC-based strategies.

Chapter 2

Review of Learning-Based Control Strategies for Robot-aided Ankle Rehabilitation

This chapter reviews the control strategies for ankle rehabilitation that use a learning-based approach, e.g., adaptive control, ILC, repetitive control (RC), etc. During the passive training phase, learning mechanisms are used to improve the trajectory tracking accuracy of ARRs. Differently, for the active phase, learning schemes are proposed to automatically adjust the amount of robot assistance and realize a better interaction performance. The characteristics of different learning-based controllers are summarized and their outcomes are analysed. It has been found that, in virtue of the repetitive nature of rehabilitation tasks, ILC-based strategies show great potential with its key idea, i.e., practice makes perfect. At the end of this chapter, existing ankle rehabilitation strategies regarding ILC-based approaches and research gaps are summarized.

2.1 Introduction

Learning is an inherent but complex human nature. Through multiple repetitions of specific tasks (physical or virtual), the allocation of limbs, cognitions and reactions are gradually optimized to achieve better results. Extensive studies have demonstrated that proper physical rehabilitation training can help patients relearn skills that would reduce their disabilities [48–50]. Meanwhile, it is suggested that a progressive training framework can accelerate the patient's learning and achieve promoted engagement [51, 52]. Therefore, retaining the advantages of the robotic device, control strategies incorporated with learning mechanisms have been extensively studied for ankle rehabilitation purposes [1, 36, 53]. Note that in the lower limb rehabilitation devices, the ankle can be treated as either a passive or active component. In this review, the lower limb rehabilitation robots with actuation of the ankle are also included.

The basic objective of the rehabilitation robot is to manipulate patients' joint that follows the desired trajectory with acceptable accuracy. At this stage, a precise trajectory tracking controller is essential to accomplish the task [1]. Note that trajectories for the robot to track can either be position or force, depending on the selection of the robot actuator. As patients recover, the effect of passive training will be gradually diminished, and active training needs to be involved for further improving their motor function. For this purpose, different term such as ”patient-cooperative” [36], ”assist-as-needed” [54] and ”variable compliance/resistance” [43] are proposed. These controllers aim to adapt/learn the level of robot assistance and realize the desired interaction performance. To conclude, during different stages of ankle rehabilitation, the purpose of employing the learning mechanism is diverse.

In conventional discrete-time control, each discrete sampling point is used for constructing the adaptive mechanism [55]. However, the rehabilitation scenario brings an important feature that each training session involves multiple repetitive tasks. Therefore, the extra dimension along the task horizon opens up the possibility of ILC and RC-based approaches [35, 56]. In the following review, learning-based discrete-time control methods such as adaptive and fuzzy logic control, as well as the ILC and RC in virtue of repetitive training environment will be included.

In addition to fully utilizing characteristics of the control object, studies on neurorehabilitation also provide a preliminary understanding of human motor learning. One of the fundamental principles of motor learning can be succinctly summarized by a cliche - “practice makes perfect” [57]. In [58], better performance has been found to correlate with the time and amount of practice dedicated to learn a particular skill. On the role of the intensity of practice on stroke rehabilitation, authors in [59] demonstrate that there is a dose-dependent relationship between post-stroke therapy and outcome. Nevertheless, in a pilot study [60], matching low-dose therapy with robotic neurorehabilitation has no significant improvement on patients' reaching performance. It strongly suggests that the benefit of robot-aided therapy, automated administration, is possible to deliver training doses that are far beyond conventional therapy. These studies can be seen, practically, as evidence of the significance of valuing the task horizon during rehabilitation.

2.2 Trajectory Tracking Control

The first stage of ankle rehabilitation mainly contains passive training. Patients are required to be fully relaxed and their ankles are stretched by a predefined robot trajectory. However, during stretching, the passive ankle stiffness can bring disturbance to the robot even when the patient is completely eased [61]. As a result, the robot movement will deviate from the desired trajectory and extra control efforts are required. Meanwhile, researches demonstrate that the simple PD controller has a good control performance for motor-driven ARRs [19], and the control gain characterizes the stiffness of the robot joint. Therefore, to avoid overlarge conflict with the patient's ankle, stiffness adaption schemes are proposed to adjust the control parameters based on tracking error feedback. Besides, the robot dynamic model contains uncertainties that also degrade the control performance. To address this issue, several learning-based approaches are adopted to provide control compensations. Moreover, considering the repetitive nature of rehabilitation training, different learning mechanisms are constructed along task horizon. Based on ILC and RC schemes, uncertain robot dynamics, unknown disturbance and stiffness adaption are resolved by updating the control input in light of the previous control results. An overview of learning-based control schemes for conducting trajectory tracking in ankle rehabilitation is summarized in

Table 2.1: Trajectory tracking control for ankle rehabilitation with learning-based approach.

Control schemes	Actuation	Categories & Feedback	Technical details
Time horizon learning			
Adaptive Control	Motor	Variable stiffness [62] Position	Robot stiffness saturation function.
		Parametric adaption [63] Position + Force	Direct robot dynamic compensation.
		Parametric adaption [64] Position	Robot dynamic linearization and compensation.
		Variable stiffness [65] Position + Force	Multi-objective based stiffness adaption with performance-based decay scheme.
		Proxy-based tuning [66] Position	Proxy-based sliding mode controller with inverse-model-based tuning algorithm.
	PM	Disturbance observer [67] Position	Adaptive backstepping sliding mode control with disturbance observer.
		Variable stiffness + Adaption [68] Position + Force	Biped model based momentum approximation and variable stiffness adaption.

Fuzzy Control	Motor	Fuzzy Decoupling Control [69] Position	Reduced adaptive fuzzy controller with compensation term for decoupled dynamics.
		Muscle-tendon based fuzzy interface [70] Position	Fuzzy interface of ankle joint and torque based on biological model.
	PM	Fuzzy-based DO [44] Position + Force	Fuzzy logic controller with genetic algorithm optimized fuzzy DO.
Other	Motor	Optimization-based tuning [71] Position	Fractional order PID controller with particle swarm optimization-based tuning.
	PM	Proportional myoelectric control [72] Position + sEMG	Subject-specific gain adaption based on muscle activity for proportional control.
Task horizon learning			
Iterative learning	Motor	Adaptive iterative learning [56] Position	Iterative learning controller for compensating robot dynamics and unknown disturbances.
	PM	Iterative feedback tuning [35] Position	Iterative feedback based PID tuning algorithm with normalized criterion.
	Voluntary	Iterative FES [73] Position	Task error based iterative learning for FES volume production.
Repetitive control	Motor	Adaptive + Learning control [74] Position	Variable stiffness adaption and robot dynamic compensation with periodic learning algorithm.

Table 2.2 where learning schemes that are based on time and task horizons are separately placed. Variable stiffness control (VSC) is commonly used to adjust the compliance of the robot and improve the tracking performance. Due to the factor that robot control gains can represent the joint stiffness, such adaption can effectively avoid overlarge conflict between the robot and the human ankle [65]. For this purpose, a piecewise function with stiffness threshold was proposed in [62] for lower limb balance training. With the known stability limit of different subjects, postural stability in presence of external perturbations can be achieved. Together with the torque feedback, authors in [68] developed advanced adaption law for active balance training. An abstracted biped model was established that describes the mathematical relation between zero moment point and physical stiffness. Compared to the constant stiffness strategy, the tracking performance is enhanced by 50%. Besides, VSC was also introduced for a wearable ankle robot [65]. Based on the average anthropomorphic data and the robot dynamic model, optimal stiffness parameters are obtained. To allow extra ROMs for the patient's ankle, a stiffness decay algorithm was proposed in [65] for decreasing the torque generated by the robot while maintaining precise tracking.

For handling uncertain robot dynamics, parametric adaption laws were designed in [63] and [64]. The control performance has been tested on an active ankle foot orthosis (AAFO) [63], with 15 s adaption, the tracking error was able to reduce from 0.0395 rad to 0.0287 rad. With the dynamic linearization approach, the controller in [64] did not require acceleration feedback that may be hard for practical implementation. The specific ankle tracking error in gait training can be reduced to approximately 0.03 rad. Besides, advanced tuning methods such as inverse-model-based [66] and swarm optimization [71] were also studied. Tracking performance of an AAFO has been increased over 80% with controller incorporated in [66]. Also, the tracking performance of a parallel ARR [71] was improved by 9.4% when compared to a conventional PID controller. In addition to above mentioned adaptive control approaches, fuzzy logic is another powerful tool for uncertainty estimation and multi-objective decision. The fuzzy decoupling control that degrades the MIMO robot dynamics to several MISO subsystems was proposed in [69]. Compared to adaptive fuzzy control with full rules, the maximum tracking error of ankle trajectory can be greatly improved. Moreover, an optimized fuzzy disturbance observer (FDO) was employed for handling the nonlinearity of PM in [44]. The single PM length tracking error was 0.024 m and the robot trajectory tracking error can be reduced to 0.086 rad.

Considering the repetitive nature of rehabilitation training, some learning-based approaches along iteration horizon were proposed. ILC is a powerful tool for handling repetitive tasks due to its simple implementation. For a motor-driven ARR introduced in [56], the ILC scheme was proposed for compensating uncertain robot dynamics and unknown sensing noise. Simulation studies were conducted that illustrate the capability of ILC for gradually increasing the tracking performance. Incorporated with dynamic movement primitives, [75] adapted the predefined trajectory with an ILC framework based on position and force feedback. However, ILC serves as a "high-level" trajectory optimizer that iteratively adapts the exercise by transferring the feedback error into an offset. Similarly, another common "high-level" ILC application is commonly used to support FES [73], by iteratively adjusting the stimulation volume based on previous tracking performance, desired joint movement can be gradually achieved. For controlling the compliance PM actuator, iterative feedback tuning (IFT) [35] was introduced to update PID parameters for enhanced tracking performance. Compared to a manually tuned PID controller, the robot tracking error can be reduced from 0.0626 rad to 0.0234 rad within 30 repetitive tasks. RC is similar to ILC, while periodic uncertainties with the known period of a lower limb exoskeleton were handled in [74]. After three training periods, the ankle tracking error can be reduced to 0.03 rad which is better than the PID controller with 0.06 rad error.

To summarize, Table 2.2 details the control performance of existing learning-based trajectory tracking controllers. The tracking errors, as the evaluation index, have been reduced by employing different methods. Specifically, it can be found that controller designs incorporated with task horizon, i.e., IFT [35] and RC [74] reduced the tracking error by 0.04 rad and 0.03 rad when compared to conventional PID controller. After

Table 2.2: Major outcomes of existing trajectory control schemes.

Categories	Major Outcomes (Tracking error reduction (rad))
VSC [68]	Compared to fixed stiffness, reduced from 0.28 to 0.14.
VSC [65]	Compared to fixed stiffness, reduced by 0.048, up to 0.095.
Adaptive [63]	Reduced from 0.04 to 0.029 after 15 s adaption.
Adaptive [64]	Reduced to 0.03 during gait training.
Inverse-model [66]	Compared to unassisted gait, reduced to 0.14.
Optimization [71]	Improved by 9.4% compared to PID.
FDO [44]	Reduced to 0.024 m for single PM and 0.086 for robot.
IFT [35]	Reduced from 0.063 (PID) to 0.023 after thirty iterations.
RC [74]	Reduced from 0.065 (PID) to 0.035 after three periodic training.

several task iterations, the converged tracking errors are 11.5% and 5.83% of the desired trajectories, respectively. However, for those controllers that only consider the time horizon, the tracking errors concerning desired trajectories are, e.g., 20% in [44], 48% in [66] and 36.4% in [64]. The above results demonstrate the potential of ILC/RC-based control strategies in improving the tracking accuracy for passive ankle ROMs training. In conclusion, during trajectory tracking control, the applied learning mechanisms are mainly used to adapt the stiffness of the robot joint, compensate for model uncertainties, and generate the modified control input. By comparison, it can be seen that the ILC-based controllers have better performance by taking full advantage of the task horizon. Anyhow, the ultimate goal for these controllers is to improve the trajectory tracking performance for precisely stretching ankle joints or maintaining gait patterns. Although the patient's effect exists during training, controllers aim to eliminate such effect and achieve the ultimate goal. In other words, the trade-off between assisting patients, encouraging individual participant and improving tracking performance have not been considered. In the next section, studies that tackle the overall interaction performance via HRI strategies are considered which are essential for the follow-up ankle strength training.

2.3 Human-Robot-Interaction Control

Various learning-based tracking controllers are reviewed above, where the patients' impact on the robot are ignored or treated as a disturbance. However, purely conducting trajectory tracking only provide passive assistance without patients' active participation [14, 28]. Clinical studies have shown that patients' enthusiasm and positive mentality are also significant conditions during the rehabilitation process [76]. For this purpose, HRI strategies that considering the patient's interaction have been widely explored. Since interactive information (force/torque, bio-signal and intention estimation) are adopted in the controller design, controllers are changing the dynamic of robots by the interactive feedback. These results are summarized in Table 2.3.

The direct way to incorporate patients' interaction is to implement a hybrid controller with both position and force information. A resistance modification based controller was proposed in [77], where target resistance was defined for improving patients' symmetry ankle strength. Similar in [78], to maintain a constant resistance for encouraging patients' engagement, a hybrid force-position controller with a fuzzy modifier was proposed. Both studies employed the sEMG as an evaluation tool and improvements on patients' ankle strength have been found after several training sessions. The interactive strategy was also considered for Rutgers Ankle [5], while position and force feedback were separately used to determine four assistance levels suggested by the therapist. After six rehabilitation sessions, the training side of patients' ankles had an average 45% improvement on targeting accuracy and stability when game-based training tasks were conducted. However, the above control strategies focus on stationary resistance training along a fixed trajectory. Although interactions were considered, proper compliance can be achieved and satisfactory outcomes were found, controllers were still be eliminating the vast majority of active contributions from patients that may cause potential safety risk and performance degradation.

Table 2.3: Interactive control strategies for ankle rehabilitation.

Control scheme	Actuation	Categories & Feedback	Technical details
Time horizon learning			
Hybrid force/position	Motor	Resistance modification [77] Force	A computer-controlled resistive load is applied for symmetry strenght training.
		Force-position fuzzy control [78] Position + Force	Hybrid controller incorporating fuzzy logic to maintain constant force resistance.
	Pneumatic cylinder	Resistance modification [5] Position + Force	4 resistance levels are designed and modified follow clinical suggestion.
Movement-base adaption	Motor	Impedance shaping [79] Position + Force	Gradual and selective support by shaping impedance with reference trajectory.
		Impedance shaping [42] Position + Force	Subject-specific, trainer-induced leg trajectories learning with assistance.
	PM	Cascade control [47] Position + Force	Cascade control with outer position loop and inner force distribution loop.
		Model-based control [80] Force	Biaxial ankle kinematic model for path generation and real-time modification.

Bio-signal	Motor	Active-compliance control [52] sEMG + Force + Position	Multi-source information fusion based on sEMG, force and position for proprioception.
		Proportional model control [81] sEMG + Force + Position	Hill-model with linear proportional model for variable assistance ratio for training.
Impedance control	Motor	Variable impedance control [43] Position	Variable stiffness and damping parameters determined by position tracking error.
		Variable damping control [7] Position + Force	Shape-preserving interpolant is designed for variable damping stability guarantee.
		Switched admittance control [1] Position + Force	Three training modes based on force feedback with admittance filter.
	PM	Adaptive admittance control [36] Position + Force	Adaption of admittance parameters with passive ankle stiffness model.
		Compliance admittance control [82] Position + Force	Admittance based control with extra joint space compliance adaption.
		Switched model control [46] Position + Force	Four sets of impedance parameters are specified for different stage of recovery.

Task horizon learning			
Progressive learning	Motor	Switched model control [83] Position + Force + Task difficulty	Variable reward for game-based training with different difficult level.
	Pneumatic cylinder	Fixed impedance control [84] Position + Force + Task difficulty	Variable movement path for strength training based on virtual game interface.
Performance-based	Motor	Variable impedance control [53] Multi-index performance	Four performance measures including sEMG for assistance level modification.
		Variable impedance control [85] Multi-index performance	Multi-task training with performance oriented selection and measurement.

To overcome the limitations of fixed trajectories on encouraging patient participation, some movement-based adaptive methods were proposed. Such approaches are commonly adopted in lower extremity exoskeletons since gait characteristics during the swing and stance phases have been well studied. Two impedance shaping schemes were designed in [79] and [42]. Gradual and selective support provided by the robot can be specified when the subject exhibited trajectory errors, such that more active participants are encouraged. Such an adaption process gives the patient additional DoF while the gait path is deviating within a reasonable range. For both studies, experiments demonstrated that the adaptive algorithm can shape the support level to the specific needs of different individuals. All healthy subjects and most patients were able to utilize the visual feedback [79] and catch on to teach-and-replay procedures to increase their active participation. In addition, trajectory adaptions were also developed for two PM-driven robots [47, 80]. A cascade control structure was proposed in [47] with trajectory adaption based on the interaction force. A predefined threshold was chosen as a performance index, while adaptive training leads to a large ankle deviation and change in the direction of ankle movement. Validations on an ARR illustrated the capability of trajectory adaption algorithm and the tracking error during training was 0.0124 rad. However, a force threshold is required to drive the adaption mechanism which is hard to justify. To better understand patients' intentions, a biaxial ankle model [80] was developed for path generation and modification. During experiments, the average ankle trajectory deviations along three DoFs are about 0.1 rad, while there are no significant changes in the interaction force. However, although the employment of the biomedical model provides insight into the patient's intention, the complexity of model parameter optimization limits its practical usage.

The movement-based adaption is highly reliant on the expert knowledge of training tasks, may not suitable for establishing a general framework for handling interaction control problems. Impedance control is proposed for analysing a wide range of interactions by conjointly controlling the relations between position and force [86]. Instead of manually establishing the adaptive parameter range like movement-based approaches, a target impedance model that takes a simple form can be easily defined with ankle biomechanical data. Based on the impedance control framework, "patient-cooperative", "assist-as-needed" and "patient/robot in charge" strategies were proposed by proper selection or adaption of impedance parameters. Position-based impedance control, normally refer as admittance control has been studied in [1, 7, 36, 82]. Three training modes: passive, active stretching and active assistance were defined in [1] with admittance filter which converts force feedback into target trajectory adaptation. Experimental studies found that the robot performance has a 4.6% decrease with the increase of desired stiffness under active stretching mode. In addition, with a 5 Nm interaction torque, the admittance filter can provide an assistive trajectory with an amplitude of 0.2 rad. In [36] and [82], admittance control is incorporated with the passive ankle stiffness model and compliance adaption law. The position tracking loop both employ the PID controller and the tracking error with variable control parameters are 0.0251 rad and 0.0183 rad, respectively. The force-based impedance control was studied in [43] and [46]. Four sets of parameters are defined in [46] for adjusting the target impedance model that provides assistance from low to high. During the interaction, the robot only contributes when a lack of interaction force is detected. In addition, variable impedance based on tracking error modification is proposed in [43]. During experiments, patients' agility is quantified using mean and maximum speed, with both increasing from the constant impedance to variable impedance condition by 29.8% and 59.9%, respectively. Patients' engagement is quantified by the overall and maximum muscle activation data, both of which showed a 10% reduction in patients' effort.

Different from trajectory tracking, where the desired trajectory is considered as an invariant object for designing the learning law, the desired interaction performance is now the control objective. However, normalized interaction performance and fixed control parameters are difficult to maintain effectiveness for different patients. Therefore, researchers then focus on mimicking physical therapy procedures with analysing training performance during previous tasks. Specifically, these studies adopted learning mechanisms along the task horizon and kept the low-level controller simple. Easy-to-difficult is commonly used for continuously maintaining training efficiency that has been used in [84] and [83]. After conducting 12 weeks and 36 sessions of training for three children with cerebral palsy [84], increased plantarflexion strength with an overall average of 0.15 Nm/kg has been found. Moreover, their gait speeds have improved on average by 11.06 cm/s. In [83], 27 volunteers with chronic hemiparetic stroke were involved in a three-week training. The average isolated ankle speed has been increased by 1.37% with 27% reduced jerk and the average gait speed has been improved by 7.3% with increased gait cadence by 1.38%.

For achieving patient-specific approach, [53] and [85] chose multiple indexes for evaluating the performance of different individuals, and the follow-on training tasks are modified with a normalized performance criterion. With performance-based progressive strategies in [53], the average motor status score for upper limb during acute rehabilitation has been improved from 3.99 to 8.15 for the experimental group and 2.0 to 3.42 for the control group. For outpatient rehabilitation, clinical scores are approximately 25 for both groups. Moreover, similar clinical outcomes can be found in [85] where the ankle targeting speed was increased by 2.2 deg/s and targeting accuracy was improved by 43.6% after conducting progressive ankle training.

To summarize, Table 2.4 details the major outcomes of existing learning-based HRI controllers. Hybrid control requires explicit knowledge of task states while gait exoskeleton is commonly implemented. Although two bio-models [36, 80] were developed for estimating patient's intention, the adapted trajectory has to be carefully handled by the inner position loop and high interaction force is likely to cause instability to the robot. Under a clinical environment, easy-to-difficult and performance-based adaption are commonly used along task horizons. However, the empirical suggestion by the therapist is the basis of these learning processes, the feasibility and effectiveness of incorporating clinical training concepts into ARR controller design require further validation.

Table 2.4: Major outcomes of existing HRI control schemes.

Categories	Major Outcomes (Improving interaction performance)
Hybrid control [78]	Mean trajectory distortion reduced from 38% to 12.5%.
Hybrid control [5]	45% improvement on targeting accuracy and stability.
Motion adaption [47]	Realizing trajectory direction change with 0.013 rad error.
Motion adaption [80]	Model-based trajectory deviation can up to 0.1rad.
Impedance control [1]	5Nm torque result in 0.2 rad trajectory deviation.
Impedance control [36]	Bio-model-based adaption with 0.025 rad error.
Impedance control [43]	Agility improved by 59.9% with 10% less effort.
Impedance control [46]	Realizing smooth switch between robot's intervention.
Progressive [84]	Strength and speed increased 0.15 Nm/kg and 11.06 cm/s.
Progressive [83]	Isolated speed increased by 1.37% with 27% reduced jerk.
Performance-based [53]	MSS improved to 8.15 and 25 for acute and outpatiet
Performance-based [85]	Speed and accuracy improved by 2.2 deg/s and 43.6%

2.4 Discussion

Robot-aided ankle rehabilitation has a variety of advantages over traditional physiotherapy by means of 1) effectively conducting repetitive operations; 2) providing quantitative real-time measures and 3) incorporating virtual resources for enhancing patients' interest. Existing studies also demonstrate the effectiveness of ARRs in clinical practice [19, 61, 85]. In this review, the control strategies of different ARRs that utilize learning-based approaches are focused. Along the time horizon, adaptive and fuzzy control are commonly used while iterative and progressive learning are preferred along the iteration horizon. The control objectives of passive and active ankle training are different that makes the functions of learning mechanisms also different.

For the sake of implementation simplicity, the classical linear controller such as PD and PID has been commonly used. A PD controller with proper gravity compensation can asymptotically stabilize the robot joint at a given set-point if the gravity force can be instantaneously evaluated [87, 88]. However, this condition is not easy to satisfy because the gravity term of ARRs contains both robot and human ankle, which is subject-specific and possibly time-varying [89]. Without gravity compensation, which most of the robots adopt, is the high gain feedback solution [55]. It may saturate the robot joint and excite high frequency mode which should be avoided especially in rehabilitation scenarios. Therefore, different dynamic compensations based on adaptive control, disturbance observer and fuzzy logic are proposed. The main drawback of these methods is that unknown parameters are assumed to be time-invariant that proposed adaption laws only converge the parameters to a system dynamic with acceptable error bound. To copy this issue, one should take full use of the repetitive nature of ROM training that the extra task horizon can be incorporated for learning controller design. As discussed in [56] and [74], ILC shows great potential which can gradually improve the tracking performance of ankle ROMs training. However, conventional ILC schemes face many challenges, e.g., open-loop nature, performance degradation due to fixed control structure and unstable transient learning behaviour. Research on how to effectively incorporate ILC-based strategies with suitable ankle ARR is still in the early stage.

Impedance control is, indeed, a powerful tool to achieve satisfactory interaction performance. The main drawback of existing impedance controllers for ankle rehabilitation is that control parameters are either set as constant or switching between some predefined ranges [1, 7, 46]. Clinical evaluations have shown that the mechanical impedance of the ankle is dynamically changing and varying as subject changes [45]. Therefore, it's inappropriate to define a constant set of impedance parameters for different patients. Some advanced results, variable impedance control [90–92], can be found in the field of HRI controller design which is nontrivial to be migrated into rehabilitation scenario. Impedance variation and learning are inspired by human behaviour, while the human limb's impedance is continuously modified by the CNS based on specific tasks. Ideally, the controller of ARR should have the same learnability that adjusts the impedance parameters spontaneously, to better deal with the complex interactive tasks with patients.

It is also noticed that the repetitive nature has been explored in trajectory tracking controller via ILC, but there is a lack of studies can be found that utilizes such feature for improving active control performance. The main reason is the extreme difficulty in establishing a subject-specific model for human ankle [26]. Moreover, during active training, the main objective of ankle rehabilitation is no longer minimizing either the tracking error or the iteration force, a trade-off between task completion and the active participant should be considered. Therefore, independently using tracking error or interaction force to evaluate the ankle training and modify the robot behaviour is somehow unreliable [40, 41]. In addition, performance-based approaches have been introduced that gradually change the difficulty of the performed tasks [53, 83–85]. Clinical outcomes in these studies demonstrate its great potential in designing effective training strategies from the control perspective. With the basic concept “practice makes perfect ”, how to effectively combine the ILC-based scheme with a progressive training program requires further investigation.

Finally, another important issue in designing ARR control strategy is that system safety has to be further considered. Unexpected movements can not only cause injuries to the patient’s ankle but also destroy the continuous use of the device. In aforementioned ARR controllers, saturation functions [46, 82], predefined parameter bounds [1, 61] and normalized functions [53, 67] are commonly used. However, due to different training requirements, these predefined parameter bounds are hard to justify and require continuous change [1, 61, 67]. Moreover, the effect of saturation functions [46, 82] have not been validated in the stability analysis of robot controllers, in that case, the overall system stability can not be guaranteed.

2.5 Research Gap

To conclude, the existing research gaps are summarized as:

- Take advantage of repetitive training nature, ILC-based methods show enhanced performance in ankle passive rehabilitation [34, 35, 56, 75]. However, there is lack of experimental validation in [56] and the ILC approach serve for "high-level" trajectory modification in [75]. Besides, the iterative fuzzy controller [34] uses a rule-based fuzzy logic that usually suffers from formulation difficulty and long processing time, and the performance of IFT in [35] is limited by its PID-based nature. Together with the performance degradation that commonly exists due to fixed learning structure. The development of an adaptive ILC scheme for ankle passive training is still open.

- To guarantee the operational safety of ankle rehabilitation robot control, saturation functions [46, 82] have been designed. However, these functions are not considered in the controller design so that the overall system stability can not be guaranteed. Besides, predefined control parameter bounds are used in [1, 7, 67] which is inappropriate for different training tasks. For these issues, designing a unified ILC-based approach that can guarantee the movement of ARR within the appropriate range and specify the safety concern in the stability analysis could be a proper solution.

- The impedance controller with fixed parameters [1, 7, 46] overlook the time-varying property of ankle dynamics. To improve interaction performance, adaptive impedance [43] and admittance control [36] are proposed via tracking error adaption and computational ankle passive torque. Nevertheless, task completion and joint torque are separately considered which may degrade the overall effectiveness of ankle training [40]. Hence, incorporating ankle impedance dynamics and learning optimal impedance parameters by minimizing both tracking error and interaction torque is still an open issue in the active ankle rehabilitation strategy.

- Task difficulty adaption [83, 84] and progressive training process [53, 85] have been validated in clinical trial with significant improvement on patients' motor function. However, there is a lack of studies that effectively translate such clinical process into ARR controller design. To start with, a comprehensive evaluation of ankle recovery is required and the clinical scores can be used for reference. Subsequently, appropriate ILC schemes that automatically adjust the robot assistance are required.

2.6 Chapter Summary

This chapter reviews learning-based control strategies for conducting passive and active ankle training. Due to the repetitive nature of rehabilitation training, it has been found that ILC-based schemes have the capability of enhancing trajectory tracking performance and achieving better interaction with patients. However, studies on ILC-based control strategies for ankle rehabilitation are rare. This chapter introduces existing results and summarizes open research gaps.

Chapter 3

The Compliant Ankle Rehabilitation Robot

This chapter addresses the first research objective by designing the CARR prototype for three-dimensional ankle exercises. The robot kinematics and dynamics are presented, as well as its construction. The CARR adopts a parallel structure to provide isolated ankle rehabilitation and, with an actuated-from-above layout, avoids lower extremity coordination during training. Four PM actuators are employed to provide compliant actuation, while rotary encoders and load cells are integrated for real-time measurement. Due to the usage of soft PM actuators, extra control difficulties come forward, i.e., nonlinearity, modelling difficulty, unknown parameters, unmodelled uncertainties and cable-like property.

3.1 Concept Design

As highlighted in Figure 1.5, the platform-based ARR with an aligned rotation centre can be considered as the most suitable mechanism for ankle rehabilitation. The major benefit of such a structure design is that the rehabilitation training can be delivered without the synergetic movement of the patient's lower extremity. In terms of rehabilitation, isolated movements for single-joint have been validated to have better outcomes with less reliance on neural factors than multiple-joint exercises [21, 22]. Besides, from a mechanical point of view [5], the parallel robot has no cumulative error that results

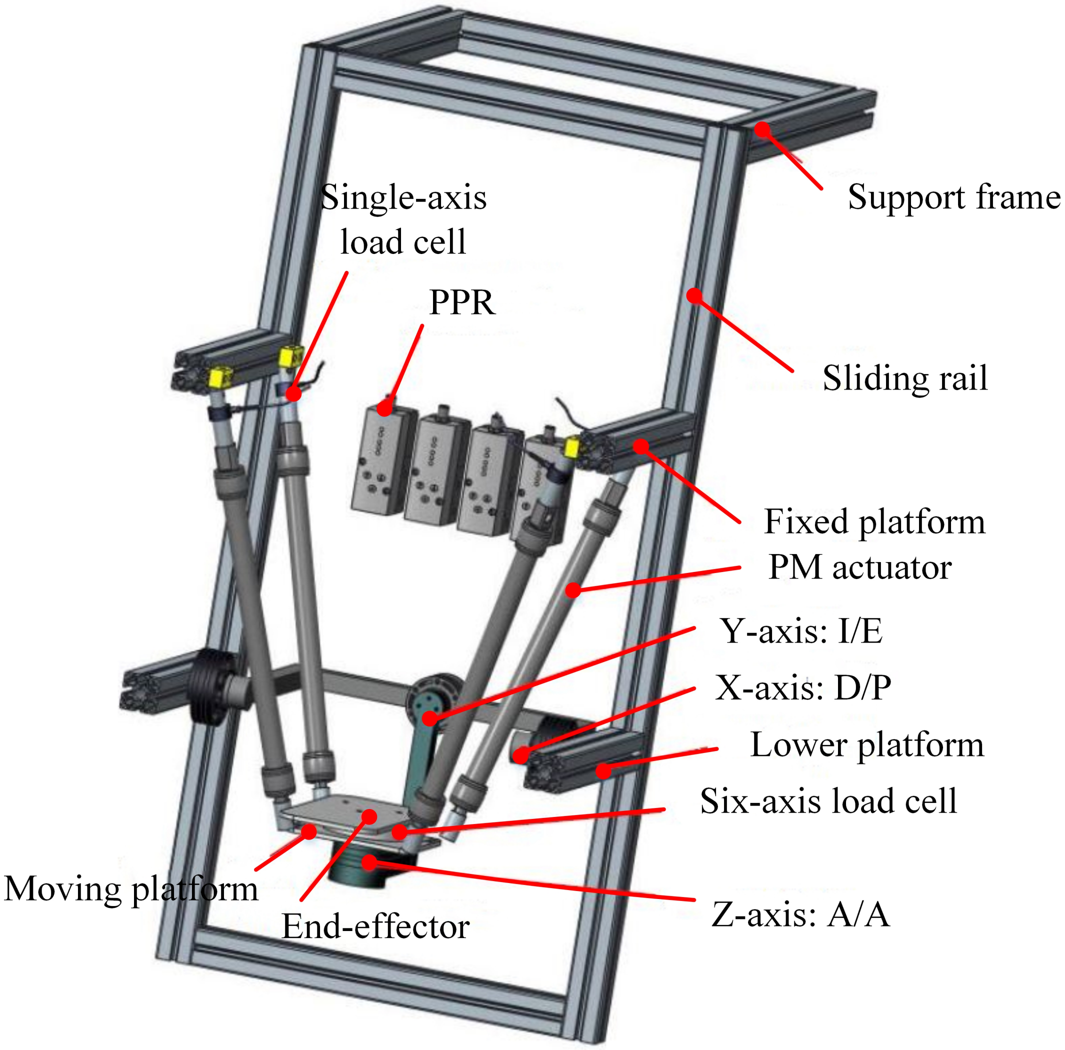

Figure 3.1: The concept design of the CARR.

in a high execution accuracy. In addition, compared to the serial robot, the parallel mechanism employs multiple actuators for manipulating the moving platform that allows a higher load capacity. In conclusion, a platform-based ARR will be adopted in this research for ankle rehabilitation.

The concept design of the CARR is presented in Figure 3.1. The robot consists of two fixed platforms, with a three-link manipulator connected to the lower platform. The moving platform is the end of a three-link manipulator which is connected with the upper fixed platform by four PMs. As an intrinsically-compliant actuator, PM is able to provide compliant actuation that is essential for rehabilitation training. On moving platforms, lightweight footplate is designed and attached as the end-effector. The three-link manipulator consists of three rotary units with encoder measurements, providing ankle ROMs along D/P, I/E and A/A, respectively. The robot body can be horizontally adjusted along the sliding rail for adapting the length of patients' lower limb and the support frame is also adjustable for supporting different sitting posture. To allow for the measurement of patient-robot interaction, a six-axis load cell is mounted between the end effector/footplate and the moving platform. Since the PM can only provide unidirectional actuation force (pulling), a redundant design is adopted with three DoFs which perfectly fits the requirements raised in the first research objective.

3.2 CARR Kinematics

The inverse kinematics of CARR can be easily obtained and provides a unique solution of the length of PMs for a given end effector posture. For passive ROM training with predefined trajectory, the control objective can be simplified to a PM length tracking problem while user's effects are considered as external disturbance. The kinematic geometry of CARR is presented in Figure 3.2, where the coordinate frame for the fixed and moving platform are denoted as $\{F\}$ and $\{M\}$ with origins O_F and O_M, respectively. ${}^F P_i$ and ${}^M P_i$ denote the connection points of the PM actuators on two platforms, $i \in 1, 2, 3, 4$, where their position vectors are defined in (3.1) as well as the position vector $\overrightarrow{O_F O_M}$ and H represents the center distance between the fixed platform and the end effector.

$$\begin{cases} {}^F P_i &= [{}^F x_i \quad {}^F y_i \quad 0]^{\mathrm{T}} \\ {}^M P_i &= [{}^M x_i \quad {}^M y_i \quad 0]^{\mathrm{T}} \\ O &= \overrightarrow{O_F O_M} = [0 \quad 0 \quad -H]^{\mathrm{T}}. \end{cases} \tag{3.1}$$

The rotations around X-, Y- and Z-axis are defined as θ_x, θ_y and θ_z, respectively.

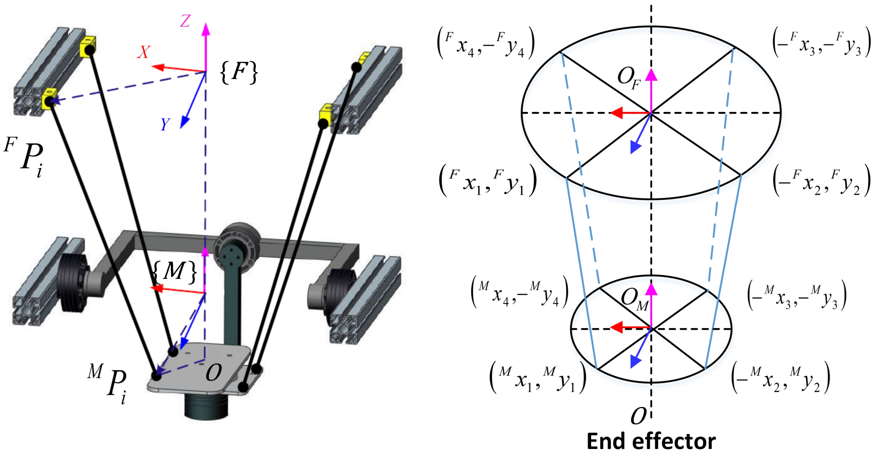

Figure 3.2: Kinematic geometry of the CARR. The X, Y and Z-axis are represented in red, blue and pink, respectively.

Following the rotation sequence ZYX, the rotation matrix R_M^F of the end effector with respect to the fixed platform can then be denoted as (3.2), where C represents the *cosine* function, S represents the *sine* function, and the subscripts represent its corresponded Euler angles, e.g., $C_x = \cos\theta_x, S_y = \sin\theta_y$. The position vector of actuators $L_i \in \mathbb{R}^{3\times 1}$ can then be described as (3.3) and the individual link length l_i is calculated by (3.4). The Jacobian matrix can then be derived by (3.5) which establishes the relationship between the joint velocity and the end-effector velocity. It is then used to derive the individual control force of each PM from a given control torque of the end-effector. Moreover, the advanced force distribution algorithm is also based on the Jacobian matrix and will be discussed in Chapter 7.

$$R_M^F = \begin{bmatrix} C_z C_y & -S_z C_x + C_z S_y S_x & S_z S_x + C_z S_y C_x \\ S_z C_y & C_z C_x + S_z S_y S_x & -C_z S_x + S_z S_y C_x \\ -S_y & C_y S_x & C_y C_x \end{bmatrix} \tag{3.2}$$

$$L_i = O + R_M^F {}^M P_i - {}^F P_i \tag{3.3}$$

$$l_i = \sqrt{L_i^{\mathrm{T}} L_i} \tag{3.4}$$

$$J = (R_M^F {}^M P_i \times \frac{L_i}{l_i})^T. \tag{3.5}$$

The current kinematic configurations of the CARR is summarised in Table 3.2. Since

Table 3.1: Kinematic configuration of the CARR.

Robot configuration	Values of coordinates (abs)	
	X	Y
Distance between upper and lower platform	445 mm	
PM connections on the upper platform	202.5 mm	140 mm
PM connections on the moving platform	65 mm	60 mm

Table 3.2: Achievable ROMs of the CARR, adapted from [12].

Type of Motion	ROM range
D/P	$35.5°$ to $-35.5°$
I/E	$34.4°$ to $-34.4°$
A/A	$45.9°$ to $-45.9°$

the contraction range of PM is limited by 25% of its initial length (0.4 m for currently used PM), the rotations along three DoFs that reach the stroke of actuators are unreachable. Detailed analysis can be found in [12], where the achievable ROMs of the CARR under current configurations are summarized in Table 3.2. By considering normal ankle characteristics presented in Table 1.1, the CARR can deliver comprehensive ankle ROMs along three DoFs.

3.3 CARR Dynamics

Position control based on inverse kinematics neglects the effects of patients that brings difficulties to active training process. With measurable interactive information, the

CARR dynamic model is essential for conducting force control. The dynamics of the CARR in task space can be described by

$$I(\theta)\dot{\omega} + \omega \times I(\theta)\omega + G(\theta) = \tau_r + \tau_h \tag{3.6}$$

where $I(\theta) \in \mathbb{R}^{3\times3}$ and $G(\theta) \in \mathbb{R}^{3\times1}$ are inertial tensor and gravitational force, respectively. The torque generated by the CARR and patient are denoted as $\tau_r \in \mathbb{R}^{3\times1}$ and $\tau_h \in \mathbb{R}^{3\times1}$. Note that $\dot{\omega} \in \mathbb{R}^{3\times1}$ and $\ddot{\omega} \in \mathbb{R}^{3\times1}$ are the rate of Euler angle change and its derivative, it can be calculated by the rotations of the CARR, i.e., $\theta = [\theta_x, \theta_y, \theta_z]^T$ upon

$$\begin{aligned} \omega &= R(\theta)\dot{\theta} \\ \dot{\omega} &= R(\theta)\ddot{\theta} + \dot{R}(\theta)\dot{\theta} \end{aligned} \tag{3.7}$$

with

$$R(\theta) = \begin{bmatrix} C_y C_z & -S_z & 0 \\ C_y S_z & C_z & 0 \\ -S_y & 0 & 1 \end{bmatrix} \tag{3.8}$$

Substituting (3.7) into (3.6) and using $\tilde{\omega}$ as the skew symmetric matrix of ω for cross product gives the simplified CARR dynamics

$$M(\theta)\ddot{\theta} + C(\theta,\dot{\theta})\dot{\theta} + G(\theta) = \tau_r + \tau_h \tag{3.9}$$

where $M(\theta) = I(\theta)R(\theta)$ is the mass matrix and $C(\theta,\dot{\theta}) = I(\theta)\dot{R}(\theta) + \tilde{\omega}I(\theta)R(\theta)$ is the Coriolis and centrifugal term. In subsequent sections, (3.9) is used to represent the CARR dynamics for controller design.

3.3.1 Interaction Torque Measure

Six-axis load cell is used to measure the interaction torque τ_h. Since the load cell is mounted between the footplate and the end-effector, the actual ankle forces and torques along each axis are obtained by transforming measurements from sensor coordinate to ankle coordinate [93] as

$$\begin{bmatrix} f_h \\ \tau_h \end{bmatrix} = \begin{bmatrix} {}^{a}_{lc}R & 0 \\ {}^{a}_{lc}P \times {}^{a}_{lc}R & {}^{a}_{lc}R \end{bmatrix} \begin{bmatrix} f_{lc} \\ \tau_{lc} \end{bmatrix} \tag{3.10}$$

$${}^{a}_{lc}P\times = \begin{bmatrix} 0 & -p_z & p_y \\ p_z & 0 & -p_x \\ -p_y & p_x & 0 \end{bmatrix} \tag{3.11}$$

where f_h and τ_h are the actual ankle force and torque, f_{lc} and τ_{lc} are force and torque measured by the load cell. ${}^{a}_{lc}R$ is a rotation matrix from the human ankle coordinate to the load cell coordinate and ${}^{a}_{lc}P\times$ is a cross product operator such that ${}^{a}_{lc}P \times {}^{a}_{lc}R$ is a skew symmetric matrix.

3.3.2 Inertial Property of the CARR

The inertial property of the CARR is essential for calculating $I(\theta)$ and $G(\theta)$ in (3.6). As shown in Figure 3.1, the moving entirety includes the three-link manipulator, the six-axis load cell and the end-effector (a 3D-printed footplate). Their inertial parameters, i.e., mass, centre of mass and inertia tensor are summarized in Table 3.3.2. The global inertia tensor and gravitational force force can be calculated by

$$I(\theta_x, \theta_y, \theta_z) = \sum_{i=1}^{3} I_i = R_i I_i R_i^T \tag{3.12}$$

$$G(\theta_x, \theta_y, \theta_z) = \sum_{i=1}^{3} G_i = R_i O_i^{COM} m_i \tag{3.13}$$

where I_i and G_i are the inertia tensor and gravitational force of i-th link, respectively. The rotation matrix of i-th link coordinate respect to the global is denoted as R_i, O_i^{COM} represents the coordinate of the COM of i-th link and m_i is the mass of the i-th link. The global coordinate frame is located at the rotation centre of the end effector with the X-axis pointing to the right, the Y-axis pointing forwards and the Z-axis pointing upwards with respect to the patient. Since three links in Table 3.3.2 are connected in series, the Denavit-Hartenberg (D-H) convention [93] is employed to attach the

Table 3.3: Inertial property of the CARR. COM: centre of mass. IT: inertia tensor.

Link (1-3 from top to bottom)	Mass (kg)	COM (mm)	IT (kg m^2 $\times 10^{-3}$)
	1.61	$(0, 0, -122)$	$\begin{bmatrix} 74.8 & 0 & 0 \\ 0 & 41.5 & 0 \\ 0 & 0 & 33.7 \end{bmatrix}$
	1.01	$(0, -133, -88)$	$\begin{bmatrix} 40.7 & 0 & 0 \\ 0 & 13.7 & -6.1 \\ 0 & -6.1 & 27.3 \end{bmatrix}$
	1.76	$(0, 10.5, -119)$	$\begin{bmatrix} 29.4 & 0 & 0 \\ 0 & 27 & 1.8 \\ 0 & 1.8 & 5 \end{bmatrix}$

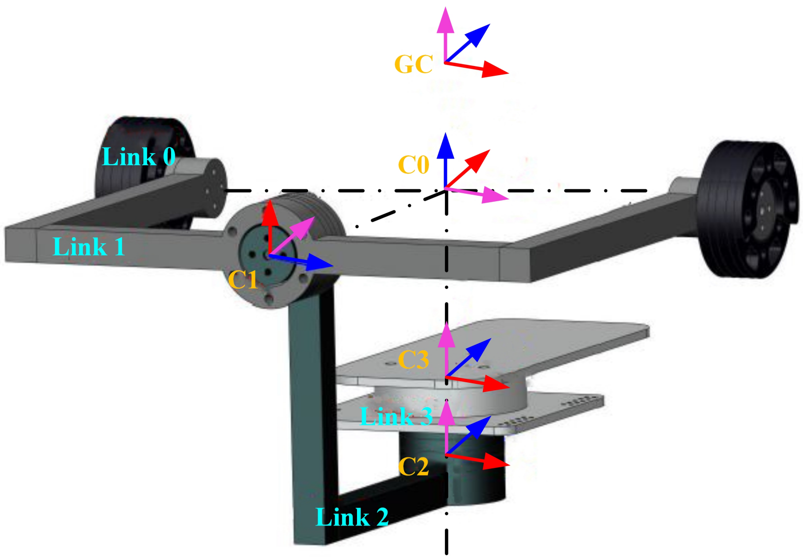

Figure 3.3: Coordinate frames of the different parts of the three-link manipulator.

global frame to the links. In this convention, each homogeneous transformation A_i is represented as a product of four basic transformations, that is

Table 3.4: D-H parameters for transformation between different frames.

Frame	α_i	a_i	d_i	θ_i
Global	$\frac{\pi}{2}$	0	0	$\frac{\pi}{2}$
Link 1	$\frac{\pi}{2}$	0	0	$\theta_x + \frac{\pi}{2}$
Link 2	$\frac{\pi}{2}$	0	0	$\theta_y + \frac{\pi}{2}$
Link 3	0	0	0	θ_z

$$
\begin{aligned}
A_i &= R_{z,\theta_i}\mathrm{Trans}_{z,d_i}\mathrm{Trans}_{x,a_i}R_{x,\alpha_i} \\
&= \begin{bmatrix} C_{\theta_i} & -S_{\theta_i} & 0 & 0 \\ S_{\theta_i} & C_{\theta_i} & 0 & 0 \\ 0 & 0 & 1 & 0 \\ 0 & 0 & 0 & 1 \end{bmatrix}
\begin{bmatrix} 1 & 0 & 0 & 0 \\ 0 & 1 & 0 & 0 \\ 0 & 0 & 1 & d_i \\ 0 & 0 & 0 & 1 \end{bmatrix}
\begin{bmatrix} 1 & 0 & 0 & a_i \\ 0 & 1 & 0 & 0 \\ 0 & 0 & 1 & 0 \\ 0 & 0 & 0 & 1 \end{bmatrix}
\begin{bmatrix} 1 & 0 & 0 & 0 \\ 0 & C_{\alpha_i} & -S_{\alpha_i} & 0 \\ 0 & S_{\alpha_i} & C_{\alpha_i} & 0 \\ 0 & 0 & 0 & 1 \end{bmatrix} \\
&= \begin{bmatrix} C_{\theta_i} & -C_{\alpha_i}S_{\theta_i} & S_{\alpha_i}S_{\theta_i} & a_iC_{\theta_i} \\ S_{\theta_i} & C_{\alpha_i}C_{\theta_i} & -S_{\alpha_i}C_{\theta_i} & a_iS_{\theta_i} \\ 0 & S_{\alpha_i} & C_{\alpha_i} & d_i \\ 0 & 0 & 0 & 1 \end{bmatrix}
\end{aligned}
\tag{3.14}
$$

where α_i, a_i, d_i and θ_i are the link twist, link length, link offset and joint angle, respectively. By determining the parameters α_i, a_i and d_i of the i-th link with respect to the $(i-1)$-th link, together with the transformed joint angle θ_i, the transformation between two links can be established. Since D-H convention requires $(n+1)$ coordinate frames to be defined for n-DoF manipulator, an additional frame (C0) is given, as shown in Figure 3.3. The origins of coordinate frames of Link 0-Link 3 and the global frame intersect at the centre of rotation of the end effector, which are separately defined in Figure 3.3. The corresponded D-H parameters are then presented in Table 3.3.2. Since only rotations exist between two connected links and no relative displacements exist while rotating, the value of a_i and d_i are always zero. The A_i in equation (3.14) can be simplified by

$$R_i = R_{Gi} = \begin{bmatrix} C_{\theta_i} & -C_{\alpha_i}S_{\theta_i} & S_{\alpha_i}S_{\theta_i} \\ S_{\theta_i} & C_{\alpha_i}C_{\theta_i} & -S_{\alpha_i}C_{\theta_i} \\ 0 & S_{\alpha_i} & C_{\alpha_i} \end{bmatrix} \tag{3.15}$$

Note that R_i of different links require the corresponding number of transformations, where the notation R_{Gi} is employed for specification. It can then be derived that

$$\begin{aligned} R_1 &= R_{G1} = R_{G0}R_{01} \\ R_2 &= R_{G2} = R_{G1}R_{12} \\ R_3 &= R_{G3} = R_{G2}R_{23} \end{aligned} \tag{3.16}$$

where R_{G0}, R_{01}, R_{12} and R_{23} are calculated with the parameters in Table 3.3.2. The inertia tensor and gravitational force in (3.12) and (3.13) can then be calculated. Subsequently, the parameters of the CARR dynamic model (3.9) are available.

3.4 Controller Design of the CARR

As a typical soft actuator, PM has attracted lots of attention in rehabilitation robotic during the last decades [94]. PM is inherently compliant with extra contractable range and efficiency in power-force conversion. The CARR inherits these advantages, as a tradeoff, additional challenges in designing controllers are raised. Firstly, the nonlinearity of PM makes precise modelling difficult, while the performance of conventional PD/PID controllers is limited [35]. Secondly, it has been found that even with an established dynamic model, the model parameters of PM are unknown and time-varying in different internal pressure intervals [95, 96]. Furthermore, the friction caused by the contraction of braided fabric and other unmodelled uncertainties have to be considered in PM controller design [97, 98]. Lastly, PM has a cable-like property that only provides pulling force. Without continuous tension, the control stability of the CARR that regards the training safety will be affected [94]. Therefore, the following chapters aim to address the research gaps reviewed in Chapter 2 as well as consider these practical control difficulties of PM.

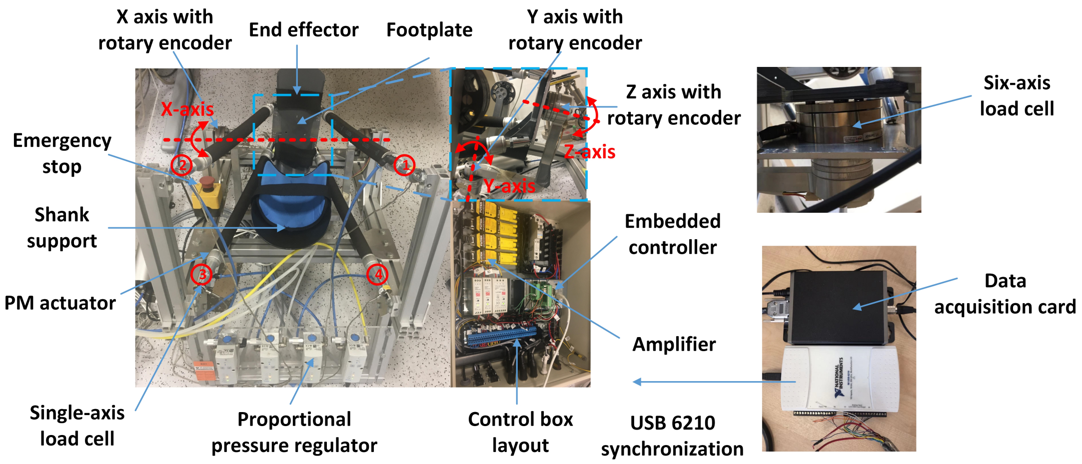

Figure 3.4: The construction of the CARR.

3.5 CARR Construction

The physical construction of the CARR is shown in Figure 3.4. It is actuated by four parallel PM actuators (Festo DMSP-20-400N) with three rotational DOFs for ankle D/P, I/E and A/A. Each PM actuator is controlled by an independent proportional pressure regulator (PPR: Festo VPPM-6L-L-1-G18-0L6H) with an initial length of 400mm, an internal diameter of 20mm and a maximum contraction force over 1500N. Three rotary encoders (ams AS5048A) are installed to measure angular displacements along Euler X-, Y- and Z-axis, which are denoted by red, blue and pink arrows, respectively. Four single-axis load cells (Futek LCM 300) together with four amplifiers (Futek CSG110) are implemented for individual PM force measure and a six-axis load cell (ATI Omega85) is mounted between end-effector and footplate for detecting interaction force. An embedded controller (NI Compact RIO-9022) is adopted to achieve real-time control and three independent data acquisition modules (NI-9401, NI-9205 and NI-9263) are used for digital I/O, analog input and analog output, respectively. For the six-axis load cell, the data acquisition box (ATI 9105-DAQ) is used and NI USB-6210 is employed for synchronizing the load cell data with other real-time measures. All control interfaces in subsequent sections are developed on a host computer

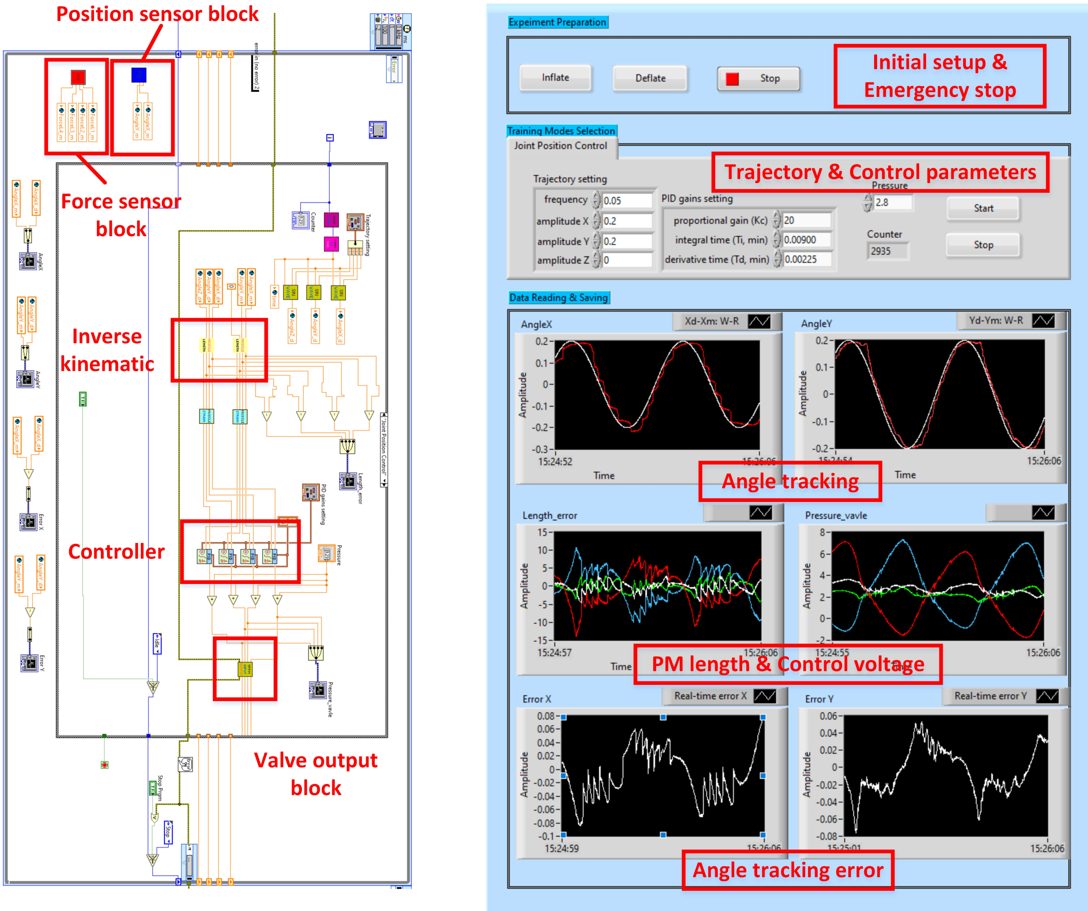

Figure 3.5: The control diagram and interface under LabVIEW environment.

based on LabVIEW and communicates with the embedded controller through TCP/IP protocol. Figure 3.5 presents the basic control diagram and interface where the sensing blocks, control blocks and real-time monitors are highlighted in red. The selections of CARR components mainly depend on the needs of the ankle treatment. The type of PM (length and diameter) affects the ROM and torque of the CARR. With the selected PM, the ROM of the CARR can reach 36° in both ankle D/P and I/E rotation and 45° in ankle A/A rotation [12]. Moreover, the torque capacity of the CARR can reach 100 Nm, 150 Nm and 40 Nm for ankle D/P, I/E and A/A rotation, respectively [12]. In accordance with the normal ankle ROM and passive torque as shown in Table 1.1, the CARR can satisfy the training specifications. Hence, to obtain the feedback information, sensors are chosen and based on the operation conditions of above components. The maximum measurement range and accuracy are $360° \pm 0.05°$, $2000\,\mathrm{N} \pm 0.5\%$ and $80\,\mathrm{Nm} \pm 1.25\%$ for the encoder, single-axis and six-axis load cell, respectively. Moreover, the sampling frequency is set as $1000\,\mathrm{Hz}$ that satisfies the control requirement of the PM [36]. Compare to the normal human response speed (a few to tens of milliseconds), the CARR can react faster which implies that the interaction between the patient and CARR can be captured and incorporated into the control strategies.

3.6 Chapter Summary

To meet the first research objective, an ARR prototype is introduced in this chapter. The CARR can provide compliant and three-dimensional ankle treatment without synergic movements of the lower extremity. Meanwhile, kinematic and dynamic measures are both available. CARR kinematics and dynamics are given, with detailed derivations and calculation processes. Additional control challenges raised by PMs are discussed and the physical construction with component details are given.

Chapter 4

Data-driven Adaptive Iterative Learning Control of a Compliant Rehabilitation Robot for Repetitive Ankle Training

To achieve three rational DOFs and soft human-robot interaction, the CARR introduced in Chapter 3 utilizes four PMs as the actuator. However, the strong nonlinearity of PMs brings difficulties in dynamic modelling and precise trajectory tracking. To solve this problem, a data-driven adaptive iterative learning controller (DDAILC) is proposed based on compact form dynamic linearization (CFDL) with estimated pseudo-partial derivative (PPD). Instead of using a PM dynamic model, the estimated PPD is updated merely by online input-output (I/O) measures. Sufficient conditions are established to guarantee the convergence of tracking errors and the boundedness of control input. Experimental studies are conducted on four human participants with two therapist-resembled trajectories. Compared with other data-driven methods, the DDAILC demonstrates significant improvement in tracking performance.

4.1 Introduction

Robot-assisted ankle rehabilitation solutions have been actively researched in the past few decades [14, 19]. As the first stage of ankle rehabilitation, the reacquisition of joint

ROM is essential for the follow-up training [12]. Therefore, a range of platform-based parallel robots are developed for ankle ROM training purposes [23], such as ARBOT in [1] and Rutgers ankle in [5]. However, these existing platform-based robots have inconsistent rotation centre with the ankle joint which discounts the recovery performance [99]. Meanwhile, a large proportion of existing devices employ non-backdrivable rigid actuators, e.g., electric motors and cylinders, which causes non-compliant human-robot interaction [100]. To overcome aforementioned limitations, the CARR was introduced in Chapter 2 that the required torque is actuated above the end effector by PMs with fixed rotation centre. However, as discussed in Chapter 3, the nonlinearity of PM bring difficulties to controller design.

Various tracking control methods have been developed for the existing platform-based ankle robots. A torque-based velocity controller was proposed in [31] to mobilize the impaired foot with a single DOF device, while the MecDEAR [32] achieved position tracking by a PD controller. An interaction controller was also constructed for ARBOT [1], where the passive training is achieved by a PID controller and a high-level admittance controller processes active training. However, the above mentioned control methods are not implementable for CARR. The complicate nonlinear relationship between contraction force, length and internal pressure of PM makes the linear based method in [31] and the standard PD or PID controller in [32] and [1] have limited performance.

Considering the modelling difficulty of CARR and the repetitive nature of ROM training, iterative learning control (ILC) shows great potential. ILC is a typical model-free method for repetitive control object which merely relies on system I/O information and improves the tracking performance gradually [101]. However, studies of ILC on rehabilitation robot are rare. ILC-driven functional electrical stimulation (FES) have been proposed in [102–104]. Nevertheless, the proposed ILC works as a “high-level” controller to adjust the magnitude of FES while the actual position control was achieved by a PID controller. Conventional PID-type ILC has been applied on several rehabilitation devices because of its simple structure and little calculation burden. A P-type ILC

(P-ILC) based feedforward controller has been proposed in [105], and two motor-driven rehabilitation robots [106], [107] achieved multi-joint trajectory tracking by PID-type ILC. However, such contraction mapping based ILC causes unstable transient performance of the system output along iteration domain, meanwhile, the fixed controller structure with unchanged learning gain also degrades the control performance consequently [108].

Inspired by recent works on model-free adaptive control [109–111], this chapter introduces a compact form dynamic linearization (CFDL) technique in iteration domain. Instead of realizing the nonlinear model of PM, the CFDL builds an equivalent data model by using an iteration-dependent time-varying parameter called pseudo partial derivative (PPD). Since PPD is unknown, a data-driven adaptive iterative learning control (DDAILC) algorithm is proposed to estimate the PPD merely using the output measures of the position information. Mathematical analysis is given to guarantee the convergence of algorithm along the iteration domain and bounded-input bounded-output stability along the time domain. Experimental studies are conducted on the CARR for repetitive ROM training with human participants involved. To evaluate the tracking performance of the DDAILC, the comparisons with P-ILC and PID controllers are given.

The main contributions of this work are listed as follows. Instead of modelling the nonlinear PM dynamic, an equivalent data model is established with reasonable assumptions. Only the position measures of the CARR are required to estimate the PPD and design controller. As a nonlinear control algorithm, the implementation of DDAILC on the CARR is the first attempt that applying data-driven learning method to the compliant actuator driven device. To mimic the rehabilitation environment, two therapist-resembled trajectories are chosen with four human participants involved. The DDAILC has significant improvement on the tracking performance.

The rest of this chapter is arranged as follows. Section 4.2 formulates the repetitive ROM training control problem for CARR. In Section 4.3, methodology of the proposed DDAILC for PM is presented with rigorous mathematical proof and convergence analysis. Experimental results and comparisons are conducted in Section 4.4 as well as effectiveness of passive training with human participants. The conclusion is given in Section 4.5.

4.2 Problem formulation

The inverse kinematics of CARR (3.1)-(3.4) provides a unique solution of the length of PMs for a given end effector posture. The length variation caused by compressed air provides actuation of PMs. In consequence, for the PM trajectory tracking control, the internal pressure and length are considered as control input and output respectively. Four individual PM lengths l_i (index $i = 1, 2, 3, 4$) can be obtained via inverse kinematic (3.1)-(3.4). Denote $p_{i,k}(t),\ l_{i,k}(t) \in \mathbb{R}$ as the input pressure and output length of i-th PM at time instant t during k-th iteration, where $t \in \{0, 1, 2, \ldots, N\}$, $N \in \mathbb{Z}^+$and $k = 1, 2, \cdots$. For an iteration invariant desired trajectory $l_i^*(t)$, the tracking error is defined as $e_{i,k-1}(t+1) = l_i^*(t+1) - l_{i,k-1}(t+1)$. The main objective of this chapter is to find a pressure sequence $p_{i,k}(t)$, such that $e_{i,k-1}(t+1) \to 0$ for $t \in \{0, 1, 2, \ldots, N\}$ as $k \to \infty$. The following discrete-time model is constructed for each PM

$$l_{i,k}(t+1) = f\big(l_{i,k}(t), \ldots, l_{i,k}(t-n_l), p_{i,k}(t), \ldots, p_{i,k}(t-n_p)\big) \tag{4.1}$$

where $f(\cdots) : \mathbb{R}^{n_l+n_p+2} \to \mathbb{R}$ is an unknown nonlinear function. $n_l \in \mathbb{Z}^+$ and $n_p \in \mathbb{Z}^+$ are two unknown orders of PM length $l_{i,k}(t)$ and PM pressure $p_{i,k}(t)$, respectively.

Assumption 1 *The partial derivative of $f(\cdots)$ with respect to the $(n_l + 2)$ th output variable is continuous.*

Assumption 2 *System (4.1) satisfies the generalized Lipschitz condition (GLC) along the iteration domain, that is, $\forall t = 0, 1, 2, \ldots, N$, $|\Delta l_{i,k}(t+1)| \leq b|\Delta p_{i,k}(t)|$ for each fixed k and $|\Delta p_{i,k}(t)| \neq 0$, where $\Delta l_{i,k}(t+1) = l_{i,k}(t+1) - l_{i,k-1}(t+1), \Delta p_{i,k}(t) = p_{i,k}(t) - p_{i,k-1}(t)$ and b is a positive constant.*

Remark 1 *The Assumptions 1 and 2 imposed on system (4.1) are easy to satisfy. The Assumption 1 holds if the internal pressure of PM is continuous, the length variation of PM is also continuous. The Assumption 2 is a physical constraint by the inherent nature of PM, i.e., finite change of internal pressure would not lead to infinite change of length.*

Lemma 1 [108] *Suppose Assumptions 1 and 2 hold, for any $|\Delta p_{i,k}(t)| \neq 0$, there must exist an iteration-dependent time-varying parameter $\Phi_{i,k}(t) \in R$, called pseudo partial derivative (PPD), such that the system (4.1) can be transformed into the following compact form dynamic linearization (CFDL) data model*

$$\Delta l_{i,k}(t+1) = \Phi_{i,k}(t)\Delta p_{i,k}(t), \quad \forall t \in 0, 1, 2, \cdots, N, \quad \forall k = 1, 2, \cdots \tag{4.2}$$

with bounded $|\Phi_{i,k}(t)| \leq b$ for any t and k.

Proof:

According to the system model (4.1) and the definitation of $\Delta l_{i,k}(t+1)$ in Assumption 2, one has

$$\begin{aligned}
\Delta l_{i,k}(t+1) =& f(l_{i,k}(t), \ldots, l_{i,k}(t-n_l), p_{i,k}(t), \ldots, p_{i,k}(t-n_p)) \\
& - f(l_{i,k-1}(t), \ldots, l_{i,k-1}(t-n_l), p_{i,k-1}(t), \ldots, p_{i,k-1}(t-n_p)) \\
=& f(l_{i,k}(t), \ldots, l_{i,k}(t-n_l), p_{i,k}(t), \ldots, p_{i,k}(t-n_p)) \\
& - f(l_{i,k}(t), \ldots, l_{i,k}(t-n_l), p_{i,k-1}(t), p_{i,k}(t-1) \ldots, p_{i,k}(t-n_p)) \\
& + f(l_{i,k}(t), \ldots, l_{i,k}(t-n_l), p_{i,k-1}(t), p_{i,k}(t-1) \ldots, p_{i,k}(t-n_p)) \\
& - f(l_{i,k-1}(t), \ldots, l_{i,k-1}(t-n_l), p_{i,k-1}(t), \ldots, p_{i,k-1}(t-n_p))
\end{aligned} \tag{4.3}$$

From the GLC condition and mean value theorem, one can obtain

$$\Delta l_{i,k}(t+1) = \frac{\partial f^*}{\partial p_{i,k}(t)}(p_{i,k}(t) - p_{i,k-1}(t)) + \zeta_{i,k} \tag{4.4}$$

where $\zeta_{i,k}$ represents the last two terms in (4.3), that is, $\zeta_{i,k} = f(l_{i,k}(t), \ldots, l_{i,k}(t-n_l), p_{i,k-1}(t), p_{i,k}(t-1) \ldots, p_{i,k}(t-n_p)) - f(l_{i,k-1}(t), \ldots, l_{i,k-1}(t-n_l), p_{i,k-1}(t), \ldots$

$, p_{i,k-1}(t-n_p))$ and $\frac{\partial f^*}{\partial p_{i,k}(t)}$ is the partial derivative of $f(\cdots)$ respect to n_l+2 variables between $[l_{i,k}(t),\ldots,l_{i,k}(t-n_l),p_{i,k}(t),\ldots,p_{i,k}(t-n_p)]^T$ and $[l_{i,k}(t),\ldots,l_{i,k}(t-n_l),p_{i,k-1}(t),p_{i,k}(t-1),\ldots,p_{i,k}(t-n_p)]^T$. Since $|\Delta p_{i,k}(t)|\neq 0$, there will always be a unique solution $\xi_{i,k}(t)$ that makes

$$\zeta_{i,k}=\xi_{i,k}(t)\Delta p_{i,k}(t) \tag{4.5}$$

Let $\Phi_{i,k}(t)=\frac{\partial f^*}{\partial p_{i,k}(t)}+\zeta_{i,k}(t)$, (4.4) can then be rewritten as

$$\Delta l_{i,k}(t+1)=\Phi_{i,k}(t)\Delta p_{i,k}(t) \tag{4.6}$$

where the boundedness of $\Phi_{i,k}(t)$ can be easily verified by Assumption 2 that completes the proof. ■

Compared with other linearization methods in [112–114], CFDL data model has the following characteristics. 1) It is a pure data-driven approach that does not require specific mathematical model of the controlled PMs; 2) The models (4.1) and (4.2) are transferred at each operating points without omitting any high-order terms, rather than a static approximation model. The $\Phi_{i,k}(t)$ is related with the pressure and length till current time instant t and the k-th iteration; 3) CFDL has simple structure and only one dynamical parameter $\Phi_{i,k}(t)$ has been used. Although the dynamics of $\Phi_{i,k}(t)$ along both domains may be complicated, its numerical behaviour is simple and can be easily estimated.

4.3 DDAILC and convergence analysis

4.3.1 Controller Design

Consider the following objective function of the internal pressure $p_{i,k}(t)$

$$J(p_{i,k}(t))=|l_i^*(t+1)-l_{i,k}(t+1)|^2+\lambda|p_{i,k}(t)-p_{i,k-1}(t)|^2 \tag{4.7}$$

where $\lambda>0$ is a weighting factor. Rewrite (4.2) as

$$l_{i,k}(t+1)=l_{i,k-1}(t+1)+\Phi_{i,k}(t)\Delta p_{i,k}(t). \tag{4.8}$$

From (4.8) and the definition of $e_{i,k-1}(t+1)$, equation (4.7) can be rewritten as

$$J(p_{i,k}(t)) = |e_{i,k-1}(t+1) - \Phi_{i,k}(t)\Delta p_{i,k}(t)|^2 + \lambda|\Delta p_{i,k}(t)|^2. \quad (4.9)$$

Differentiating (4.9) with respect to $p_{i,k}(t)$, and setting $\frac{\partial J}{\partial p_{i,k}(t)} = 0$, one has

$$\Phi_{i,k}(t)e_{i,k-1}(t+1) = |\Phi_{i,k}(t)|^2\Delta p_{i,k}(t) + \lambda\Delta p_{i,k}(t). \quad (4.10)$$

Thus, the DDAILC at the k-th iteration is constructed

$$p_{i,k}(t) = p_{i,k-1}(t) + \frac{\rho\,\Phi_{i,k}(t)}{\lambda + |\Phi_{i,k}(t)|^2}e_{i,k-1}(t+1) \quad (4.11)$$

where $\rho \in (0,1]$ is a step factor to make the control algorithm more general and related to the convergence properties.

Remark 2 *The $\Phi_{i,k}(t)$ is generally used as adaptive parameter in model-free adaptive control. DDAILC extends $\Phi_{i,k}(t)$ to the iteration domain, guaranteeing the algorithm convergence along iteration domain. The non-causal term $e_{i,k-1}(t+1)$ can be obtained from last iteration, which guarantees the stability of the algorithm along time domain within the current iteration.*

Remark 3 *Let $\Phi_{i,k}(t) = \Gamma_P$, where Γ_P is a positive constant, the control law (4.11) becomes a traditional P-ILC law with fixed learning gain. The tracking performance of P-ILC will be compared with the proposed DDAILC in* Section 4.4.

Since $\Phi_{i,k}(t)$ is unknown, an estimation algorithm is then constructed for iteratively updating its estimated value $\hat{\Phi}_{i,k}(t)$. Consider the following objective function of $\hat{\Phi}_{i,k}(t)$,

$$J(\hat{\Phi}_{i,k}(t)) = |\Delta l_{i,k-1}(t+1) - \hat{\Phi}_{i,k}(t)\Delta p_{i,k-1}(t))|^2 + \mu|\hat{\Phi}_{i,k}(t) - \hat{\Phi}_{i,k-1}(t)|^2 \quad (4.12)$$

where $\mu > 0$ is a weighting factor. Differentiating (4.12) with respect to $\hat{\Phi}_{i,k}(t)$, and setting $\frac{\partial J}{\partial \hat{\Phi}_{i,k}(t)} = 0$, the following $\Phi_{i,k}(t)$ estimation algorithm can be derived

$$\hat{\Phi}_{i,k}(t) = \hat{\Phi}_{i,k-1}(t) + \frac{\eta\Delta p_{i,k-1}(t)}{\mu + |\Delta p_{i,k-1}(t)|^2} \times (\Delta l_{i,k-1}(t+1) - \hat{\Phi}_{i,k-1}(t)\Delta p_{i,k-1}(t)) \quad (4.13)$$

where $\eta \in (0, 1]$ is a step factor, being included to make the estimation algorithm more general and flexible.

To ensure that $\Delta p_{i,k} \neq 0$ is satisfied and strengthen the ability of the estimation algorithm (4.13) for tracking iteration-varying parameter, the following reset algorithm [108] is presented

$$\begin{aligned}\hat{\Phi}_{i,k}(t) = \hat{\Phi}_{i,1}(t), \text{if } &|\hat{\Phi}_{i,k}(t)| \leq \varepsilon \text{ or} \\ &|\Delta p_{i,k-1}(t)| \leq \varepsilon \text{ or} \\ &\text{sign}(\hat{\Phi}_{i,k}(t)) \neq \text{sign}(\hat{\Phi}_{i,1}(t))\end{aligned} \tag{4.14}$$

where $\hat{\Phi}_{i,1}(t)$ is the initial value of $\hat{\Phi}_{i,k}(t)$, ε is a small positive constant and sign represents the signum function [108].

Integrating the control algorithm (4.11) and parameter estimation algorithm (4.13) with reset scheme (4.14), the overall DDAILC for the PM length tracking is constructed. Figure 4.1 demonstrates the DDAILC for a single PM. Then, the implementation of the DDAILC for CARR trajectory tracking is presented in Figure 4.2.

Remark 4 *It is noticed that, the proposed DDAILC algorithm contains some tunable parameters. Specifically, in the control updated law* (4.11)*, γ is an important parameter that determines the learning gain. The theoretical analysis will show that a suitable choice of γ can guarantee the stability of the system. Besides, ρ is a controller parameter that can determine the stability condition. In practice, its initial value can be set as 1 and adjust within* $(0, 1]$*. In the reset algorithm* (4.14)*, ε is a small positive constant and often selected as* 10^{-4} *or* 10^{-5}*.*

4.3.2 Convergence Analysis

Assumption 3 *The $\Phi_{i,k}(t)$ satisfies that $\Phi_{i,k}(t) > \sigma > 0, \forall t \in \{0, 1, 2, \cdots, N\}$ and $\forall k = 1, 2, \cdots$, where σ is a positive constant.*

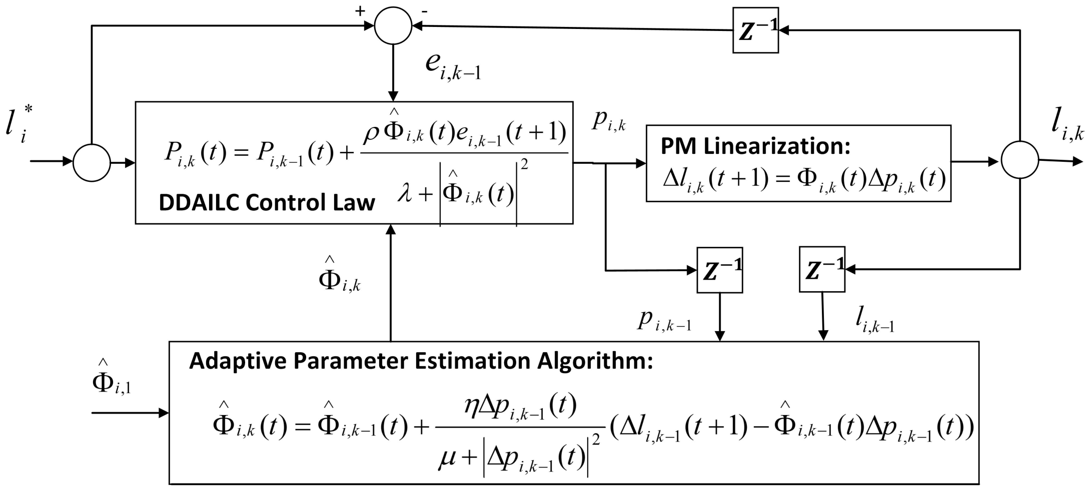

Figure 4.1: Control diagram of the DDAILC on single PM actuator.

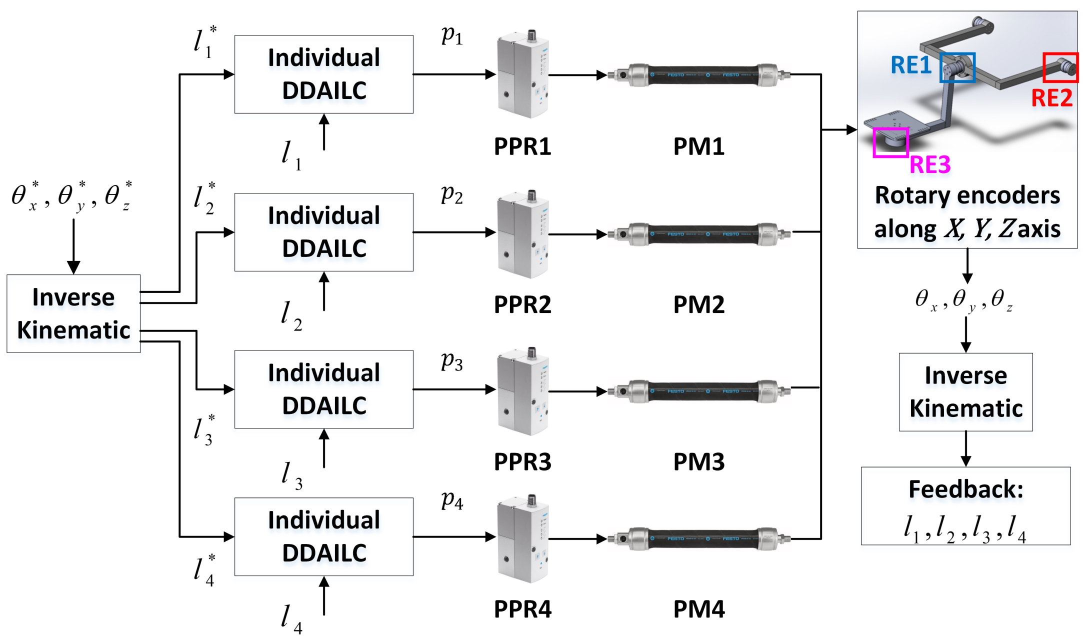

Figure 4.2: Implementation of the DDAILC for CARR trajectory tracking.

Remark 5 *Assumption 3 indicates that the contractile length of PM does not decreases as the corresponding internal pressure increases. Such linear-like characteristic is commonly applied on PM controller design [115].*

Theorem 1 *Suppose Assumptions 1-3 hold for (4.1). With bounded initial error $e_{i,1}(t)$ and initial pressure $p_{i,1}(t)$, if the DDAILC controller (4.11), (4.13) and (4.14) are applied and the weighting factor λ is selected by $\lambda > \frac{b^2}{4}$, the following results hold.*

(1) Estimated PPD $\hat{\Phi}_{i,k}(t)$ is bounded.

(2) Tracking error $e_{i,k-1}(t+1)$ monotonically converge to zero.

(3) Input pressure $p_{i,k}(t)$ and output $l_{i,k}(t)$ are bounded.

Proof. The proof consists of three parts. First, the boundedness of the estimated PPD is given. Then, the pointwise convergence of the length tracking error will be shown. Last, the proof on boundedness of system input and output will be given.
Part (1): The boundedness of $\hat{\Phi}_{i,k}(t)$.
For any $|\hat{\Phi}_{i,k}(t)| \leq \varepsilon$ or $|\Delta p_{i,k-1}(t)| \leq \varepsilon$ or $\text{sign}(\hat{\Phi}_{i,k}(t)) \neq \text{sign}(\hat{\Phi}_{i,1}(t))$, the boundedness of $\hat{\Phi}_{i,k}(t)$ is guaranteed by the reset algorithm (4.14). Otherwise, define the estimation error $\tilde{\Phi}_{i,k}(t) = \hat{\Phi}_{i,k}(t) - \Phi_{i,k}(t)$. Subtracting $\Phi_{i,k}(t)$ from both side of (4.13), one has

$$\begin{aligned}\tilde{\Phi}_{i,k}(t) =& \tilde{\Phi}_{i,k-1}(t) - (\Phi_{i,k}(t) - \Phi_{i,k-1}(t)) + \frac{\eta \Delta p_{i,k-1}(t)}{\mu + |\Delta p_{i,k-1}(t)|^2} \times (\Delta l_{i_k-1}(t+1) \\ & - \hat{\Phi}_{i,k-1}(t) \Delta p_{i,k-1}(t)). \end{aligned} \tag{4.15}$$

Substituting the CFDL model (4.2) into (4.15), it yields

$$\begin{aligned}\tilde{\Phi}_{i,k}(t) =& \tilde{\Phi}_{i,k-1}(t) - (\Phi_{i,k}(t) - \Phi_{i,k-1}(t)) + \frac{\eta \Delta p_{i,k-1}(t)}{\mu + |\Delta p_{i,k-1}(t)|^2} \times (\Phi_{i,k-1}(t) \\ & \times \Delta p_{i,k-1}(t) - \hat{\Phi}_{i,k-1}(t) \Delta p_{i,k-1}(t)) \\ =& (1 - \frac{\eta |\Delta p_{i,k-1}(t)|^2}{\mu + |\Delta p_{i,k-1}(t)|^2}) \tilde{\Phi}_{i,k-1}(t) - (\Phi_{i,k}(t) - \Phi_{i,k-1}(t)). \end{aligned} \tag{4.16}$$

Since $\eta \in (0, 1]$ and $\mu > 0$, the function $\frac{\eta|\Delta p_{i,k-1}(t)|^2}{\mu+|\Delta p_{i,k-1}(t)|^2}$ is monotonically increasing with respect of $|\Delta p_{i,k-1}(t)|^2$ and its minimum value is $\frac{\eta\varepsilon^2}{\mu+\varepsilon^2}$. Thus, there exists a positive constant d_1 such that

$$0 < (1 - \frac{\eta|\Delta p_{i,k-1}(t)|^2}{\mu + |\Delta p_{i,k-1}(t)|^2}) \leq (1 - \frac{\eta\varepsilon^2}{\mu + \varepsilon^2}) = d_1 < 1. \tag{4.17}$$

Substituting (4.17) into (4.16) and take absolute value on both sides, it can be deduced that

$$\begin{aligned} |\tilde{\Phi}_{i,k}(t)| &= \left|1 - \frac{\eta|\Delta p_{i,k-1}(t)|^2}{\mu + |\Delta p_{i,k-1}(t)|^2}\right| |\tilde{\Phi}_{i,k-1}(t)| + |\Phi_{i,k}(t) - \Phi_{i,k-1}(t)| \\ &\leq d_1|\tilde{\Phi}_{i,k-1}(t)| + 2b \\ &\vdots \\ &\leq d_1^{k-1}|\tilde{\Phi}_{i,1}(t)| + \frac{2b}{1 - d_1}. \end{aligned} \tag{4.18}$$

According to Lemma 1, the bounded condition $|\Phi_{i,k}(t)| \leq b$ leads to $|\Phi_{i,k}(t) - \Phi_{i,k-1}(t)| \leq 2b$. Thus, from (4.18), $\tilde{\Phi}_{i,k}(t)$ is bounded which implies that $\hat{\Phi}_{i,k}(t)$ is also bounded.

Part (2): The convergence of $e_{i,k}(t + 1)$.

In light of Lemma 1 and control law (4.11), one has

$$\begin{aligned} e_{i,k}(t + 1) =& l_i^*(t + 1) - l_{i,k-1}(t + 1) - \hat{\Phi}_{i,k}(t)\big(p_{i,k}(t) - p_{i,k-1}(t)\big) \\ =& (1 - \frac{\rho\Phi_{i,k}(t)\hat{\Phi}_{i,k}(t)}{\lambda + |\hat{\Phi}_{i,k}(t)|^2})e_{i,k-1}(t + 1). \end{aligned} \tag{4.19}$$

Since $\lambda + |\hat{\Phi}_{i,k}(t)|^2 \geq 2\sqrt{\lambda}\hat{\Phi}_{i,k}(t)$ and $\Phi_{i,k}(t)$ is bounded by b, there must exist a positive constant d_2 such that

$$0 < d_2 \leq \frac{\Phi_{i,k}(t)\hat{\Phi}_{i,k}(t)}{\lambda + |\hat{\Phi}_{i,k}(t)|^2} \leq \frac{b}{2\sqrt{\lambda}}. \tag{4.20}$$

Since $\rho \in (0, 1]$ and $\lambda > \frac{b^2}{4}$, according to (4.20), there must exist a positive constant $d_3 < 1$ that leads to

$$0 < d_2 \leq \frac{b}{2\sqrt{\lambda}} < 1 \quad \text{and} \quad \left|1 - \frac{\rho\Phi_{i,k}(t)\hat{\Phi}_{i,k}(t)}{\lambda + |\hat{\Phi}_{i,k}(t)|^2}\right| \leq 1 - \rho d_2 \triangleq d_3 < 1. \tag{4.21}$$

Taking absolute value on both sides of (4.19) and using (4.21), it yields

$$\begin{aligned}|e_{i,k}(t+1)| &= \left|1 - \frac{\rho\Phi_{i,k}(t)\hat{\Phi}_{i,k}(t)}{\lambda + |\hat{\Phi}_{i,k}(t)|^2}\right| |e_{i,k-1}(t+1)| \\ &\leq d_3|e_{i,k-1}(t+1)| \\ &\vdots \\ &\leq d_3^{k-1}|e_{i,1}(t+1)|. \end{aligned} \tag{4.22}$$

which indicates that $e_{i,k}(t+1)$ converges to zero in a pointwise manner over the finite time interval N when $k \to \infty$.

Part (3): The boundedness of $l_{i,k}(t)$ and $p_{i,k}(t)$.

Since $l_i^*(t)$ is iteration-invariant, the convergence of $e_{i,k}(t)$ implies that $l_{i,k}(t)$ is also bounded. Using same procedure in (4.21), it can be inferred that

$$|\Delta p_{i,k}(t)| = \left|\frac{\rho\hat{\Phi}_{i,k}(t)e_{i,k-1}(t+1)}{\lambda + |\hat{\Phi}_{i,k}(t)|^2}\right| \leq \left|\frac{\rho}{2\sqrt{\lambda}}\right| |e_{i,k-1}(t+1)| \triangleq d_4|e_{i,k-1}(t+1)| \tag{4.23}$$

where d_4 is a bounded positive constant.

Expanding $p_{i,k}(t)$ into following form

$$\begin{aligned}|p_{i,k}(t)| =& |p_{i,k}(t) - p_{i,k-1}(t)| + |p_{i,k-1}(t) - p_{i,k-2}(t)| + \cdots + |p_{i,2}(t) - p_{i,1}(t)| + |p_{i,1}(t)| \\ =& |\Delta p_{i,k}(t)| + \cdots + |\Delta p_{i,2}(t)| + |p_{i,1}(t)|. \end{aligned} \tag{4.24}$$

According to (4.22), (4.23) and (4.24), one has

$$|p_{i,k}(t)| \leq d_4\frac{1}{1-d_3}|e_{i,1}(t+1)| + |p_{i,1}(t)|. \tag{4.25}$$

Since both initial error and pressure are given bounded, the inequality (4.25) implies that $p_{i,k}(t)$ is bounded $\forall t \in \{0, 1, 2, \cdots, N\}$ and $\forall k = 1, 2, \cdots$. ■

4.4 Experiments and results

4.4.1 DDAILC for Repetitive CARR Control

The control performance for repetitive CARR tracking is first validated without human participants. The particular case, a fixed learning gain P-ILC is applied for comparison.

As a mature data-driven method, the commonly used PID controller in compliant actuator driven device [7, 12, 33] is set as baseline. The trajectory applied in first task is a sinusoidal waveform along X-axis with an amplitude of 0.2 rad and a period of 20 s, the sampling rate is 20 Hz. The fixed learning gain of P-type ILC is $\Gamma_p = 0.8$ and controller parameters of the DDAILC are set as $\rho = 1, \lambda = 1.5, \mu = 1$ and $\eta = 0.2$. Setting the initial input signals for both methods as $p_{i,1}(t) = 0$. For the initial PPD value, it is suggested not to be too large [108], so that it is chosen as $\hat{\Phi}_{i,1}(t) = 2$. The PID gains are $K_p = 20$, $K_i = 9 \times 10^{-3}$ and $K_d = 2.25 \times 10^{-3}$.

The tracking results in different iterations are shown in Figure 4.3. Both ILC methods gradually enhance the CARR tracking, while P-ILC and DDAILC requires 10 and 6 iterations to achieve same performance as baseline, respectively. From error convergence curve in Figure 4.3(c), it is observed that DDAILC smoothly converge the tracking error within 10 iterations. However, after 10^{th} iterations, the convergence curve of P-ILC is decreased apparently slow. The possible reason is that, with unchanged learning gain, the performance of P-ILC is degraded when the tracking error approaches to some limits. The value of $\hat{\Phi}_{i,k}(t)$ along both domains is given in Figure 4.3(d). It can be seen that $\hat{\Phi}_{i,k}(t)$ has significant updates in the early stage of learning and maintains similar curve when error is converged. Compared to the baseline (0.06 rad), after 15 iterations, the P-ILC and DDAILC can improve the performance by 0.01 rad and 0.03 rad, respectively.

4.4.2 Learning Capability of Various Control Objectives

The data-driven nature allows DDAILC to tackle different control objectives while maintaining its performance. Specifically in rehabilitation scenario, different DOFs and ROMs are normally required. To ensure the safety of human subjects, further test is defined along Y-axis with 0.2 rad for 15 iterations, consequently, another 15 iterations increase the amplitude to 0.3 rad.

To eliminate the effects of parameter tuning, control parameters remain unchanged. The tracking results of the second iteration cycle are shown in Figures 4.4. It indic-

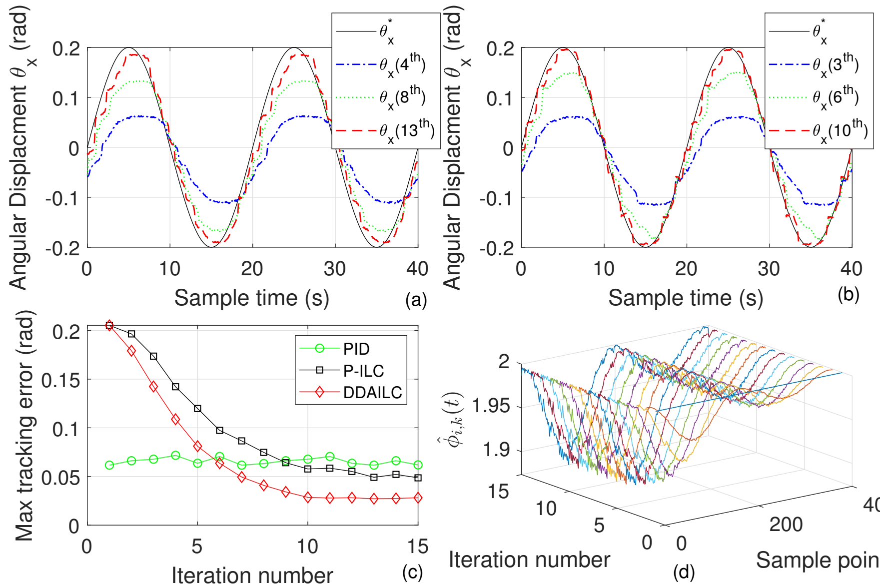

Figure 4.3: Tracking results along X-axis. (a) P-ILC. (b) Proposed DDAILC. (c) Maximum error convergence. (d) The $\hat{\phi}_{i,k}(t)$ of PM1 along both domains.

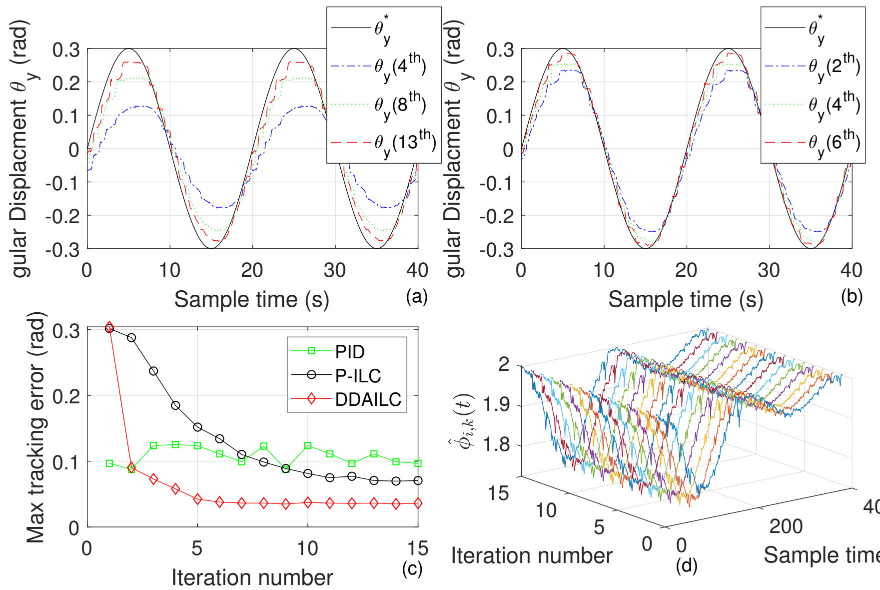

Figure 4.4: Tracking results along Y-axis (0.3 rad). (a) P-ILC. (b) Proposed DDAILC. (c) Maximum error convergence. (d) The $\hat{\phi}_{i,k}(t)$ of PM1 along both domains.

Table 4.1: Participants information

Gender (No.)	Age	Height (cm)	Weight (kg)
M (6)	25.67 ± 2.8	175.17 ± 6.85	71.5 ± 8.87
FM (4)	25.75 ± 3.86	166.25 ± 9.91	57.5 ± 6.61

M: Male, FM: Female. Data format: Mean $\pm$ SD.

ates that both ILC methods can also fulfil a 0.3 rad trajectory as iteration increases. However, with the initial setting, the P-ILC starts a new learning progress and 13 iterations are required. Although the initial pressure is reset, the DDAILC able to use the stored value of $\hat{\Phi}_{i,k}(t)$ and provide an equivalent pressure sequence which quickly drive the CARR to approximate 0.2 rad. Subsequently, only 4 more iterations are required for an perfect tracking. The maximum error convergences in Figure 4.4(c) imply that the tracking error of all methods have slightly increased due to larger control range. However, for DDAILC, the monotonic convergence property is retained with smooth error curve. Furthermore, clearly in Figure 4.4(d), the stored value of $\hat{\Phi}_{i,k}(t)$ works in the first iteration. Compared to the baseline (0.1 rad), after 15 iterations, the P-ILC and DDAILC can improve the performance by 0.03 rad and 0.065 rad, respectively.

4.4.3 Passive Training with Human Participants

To validate the performance of DDAILC when conducting passive training to users, tests were performed on ten healthy human participants and their detailed information are given in Table 4.1. All participants are confirmed with no neurological injury or recent physical impairment that affects normal ROM of their ankle joints. This trial has been approved by the University of Leeds Research Ethics Committee (reference MEEC 18-001). The maximum amplitude of the selected ROM is 0.3 rad and the period is 20 s, the overall angular velocity of CARR during operation is under $20 mrad/s$ that largely mimic clinical environment. Each test contains 15 repetitive movements (7 min) with a inter-group rest. Emergency stops have been developed for both hardware and software aspects to avoid any unexpected accidents.

To imitate physical rehabilitation procedure, two therapist-resembled trajectories [116] are performed:

T1: Joint movement along both X and Y-axis which from initial position to 0.2 rad dorsiflexion/inversion and then 0.2 rad plantarflexion/eversion.

T2: Progressive training along X-axis from 0.2 rad to 0.3 rad.

Although participants are encouraged to relax their ankle joint during training, the individual passive torque produced by the stretch of the muscles, tendons and ligaments is inevitable. This passive torque is not considered in our controller design, which can evaluate the performance of DDAILC with uncertainties. Note that in our previous work [117], the length tracking control was conducted on a simple PM platform along vertical direction. The control performance with such uncertainties have not been validated. Same comparisons are conducted with P-ILC and PID controllers. Hereinafter, P1 will be chosen as an example and the tracking results for both trajectories are shown in Figure 4.5 and Figure 4.7 respectively. For detailed working conditions of each PM, the single muscle length convergence and the value of our designed objective function $J(p_{i,k}(t))$ are given in Figure 4.6 and Figure 4.8. The green, black, red and blue lines represent PM1 to PM4 as shown in Figure 3.1.

The tracking results and error convergence along different axes of T1 are given in Figure 4.5. Without any parameters change, the DDAILC maintains precise tracking performance with 0.03 rad and 0.025 rad maximum tracking error after 10 iterations. Although the P-ILC can also gradually follow the joint trajectory within 15 iterations, 5% and 10% increase of maximum tracking error are found when compared to non-participant results. Moreover, the performance of PID becomes worse where the tracking error for both axes have increased 0.02 rad. Overall, compared to baseline, the DDAILC has improvement on maximum error with 0.03 rad and 0.02 rad along X and Y-axis respectively.

Detailed conditions of each PM are presented in Figure 4.6. During T1, the CARR conducts a diagonally movement where the dynamics of PM1 and PM3 are the same as well as PM2 and PM4. Correspondingly, the convergence curves of aforementioned

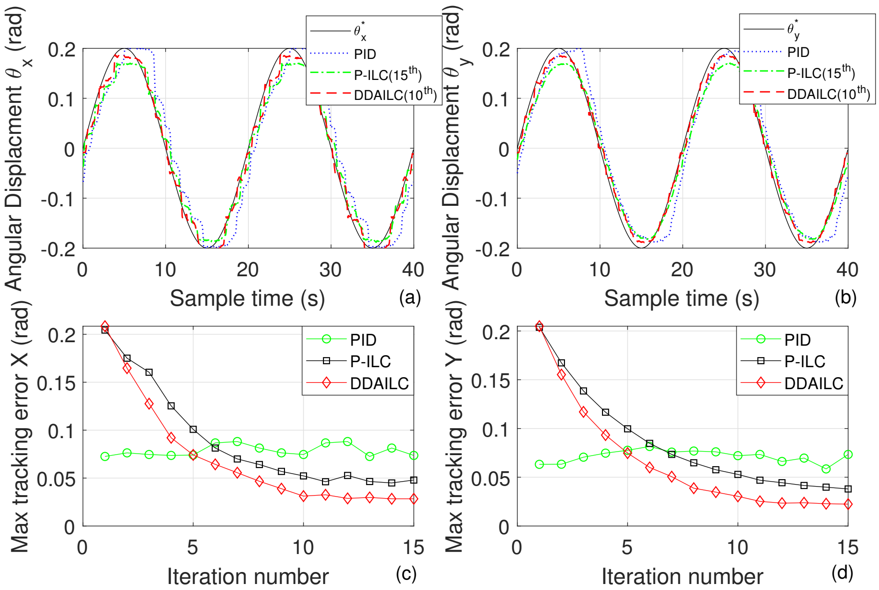

Figure 4.5: Tracking results under T1 movement. (a) X-axis. (b) Y-axis. (c) X-axis error convergence. (d) Y-axis error convergence.

groups in Figure 4.6(a) have the same tendency. Due to different length of contraction, PM2 and PM4 have larger control range with a 4mm maximum tracking error, while PM1 and PM3 are able to limit the error within 2mm. Same conditions can be found in Figure 4.6(b), where PM2 and PM4 decrease the value of $J(p_{i,k}(t))$ from over 0.5 to 0.01 while PM1 and PM3 converge it from 0.03 to 0.002.

Actual trajectories of T2 under different controllers are given in Figure 4.7. With the readable value of $\hat{\Phi}_{i,k}(t)$, the convergence speed of DDAILC for the progressive trajectory has greatly improved. From Figure 4.7(c), it can be seen that P-ILC and PID both have significant increase on maximum tracking error when the control range is increased. For the numerical results, the PID has an increase of maximum error from 0.08 rad to 0.1 rad and P-ILC reduces it to 0.06 rad. However, the DDAILC can further enhance the tracking error by 0.02 rad.

Differ from T1, the convergence curves of each muscle are regrouped in Figure 4.8 by PM1 - PM2 and PM3 - PM4. The maximum length error of four PMs are around 2mm for the first trial and 3.5mm for the follow-up trial, which is tiny enough for perform an

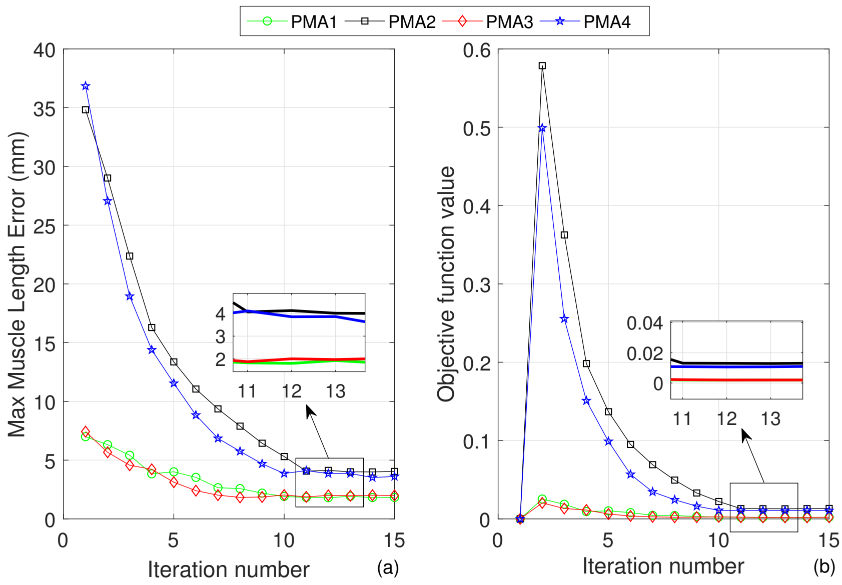

Figure 4.6: Muscle length errors and designed objective functions under T1 movement. (a) Muscle length convergences. (b) The $J(p_{i,k}(t))$.

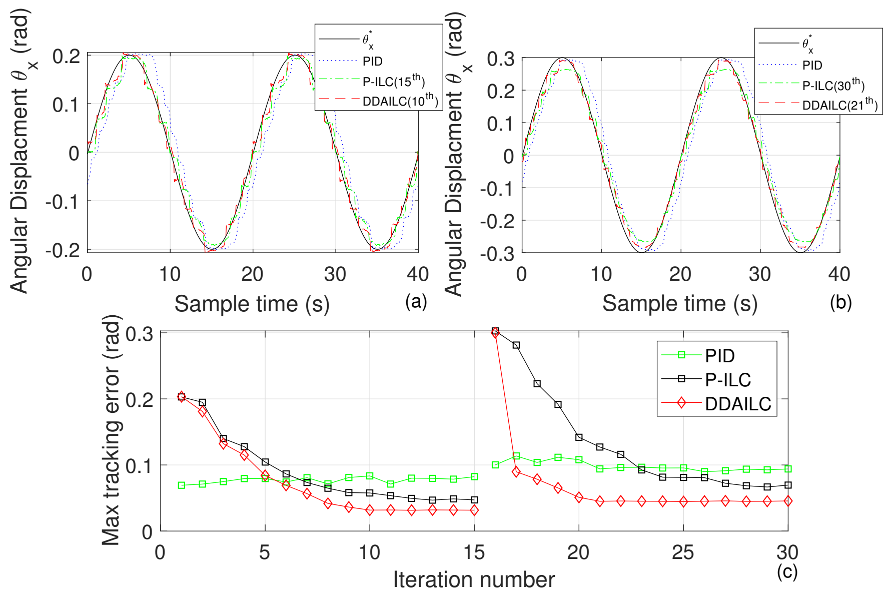

Figure 4.7: Tracking results of P1 under T2 movement. (a) Tracking results for first trial (0.2rad). (b) Tracking results for the follow-up trial (0.3rad). (c) Overall convergence curve along two trials.

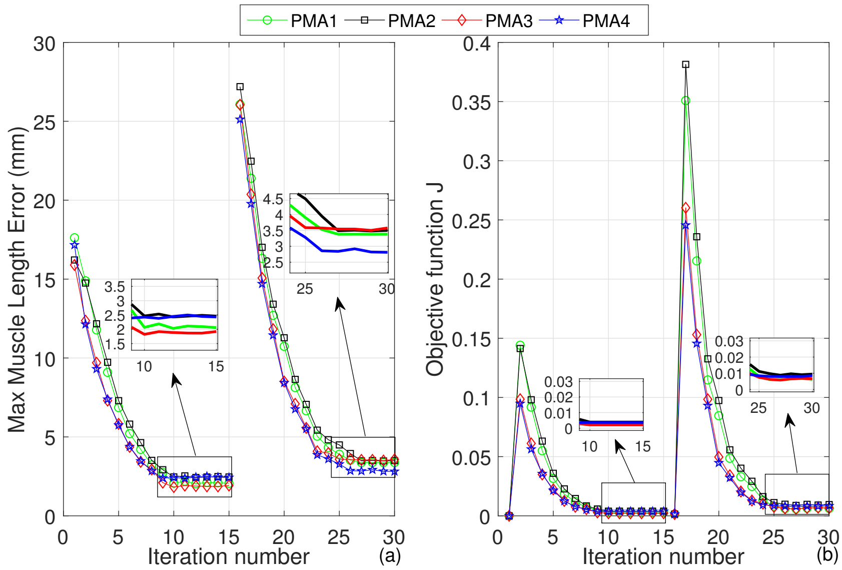

Figure 4.8: Single muscle length error and designed objective function variation of P1 under T2 movement. (a) Muscle length error convergence of all four PMs along two trials. (b) The $J(p_{i,k}(t))$ of all four PMs along two trials.

excellent tracking. After the initial setting at 1^{th} iteration and 16^{th} iteration in Figure 4.8(b), the objective function $J(p_{i,k}(t))$ for both trial is started by 0.15 and 0.38. The DDAILC is able to converge the value to 0.005 and 0.01, while only 5 iterations required for the follow-up trial.

To statistically analyse the tracking performance of applied methods while conducting different passive training with human participants. Apart from the maximum tracking error, another two criteria are analysed: 1) Root mean square error (RMSE) that indicating the tracking stability between each discrete sample for the entire trajectory; 2) Peak amplitude error which represents the capability of completing a desired peak

Table 4.2: The statistical results of three performance criteria for T1 and T2.

		Angle rms error (rad)			Peak amplitude error (rad)			Max error (rad)		
T1	Iteration number	5	10	15	5	10	15	5	10	15
P-ILC	X-axis	0.0607	0.0274	0.0215	0.0873	0.0327	0.0252	0.1027	0.059	0.05
	Y-axis	0.0594	0.0289	0.0217	0.0852	0.0402	0.0272	0.0968	0.0503	0.0374
DDAILC	X-axis	0.045	0.0155	0.0117	0.0663	0.0184	0.0063	0.0837	0.0375	0.0272
	Y-axis	0.0429	0.0121	0.0087	0.0649	0.0157	0.0085	0.0719	0.0293	0.0185
PID	X-axis	0.0403			0.0171			0.0898		
	Y-axis	0.0353			0.0169			0.0724		

T2	Amplitude	0.2 rad		0.3 rad		0.2 rad		0.3 rad		0.2 rad		0.3 rad	
	& Trail number	5	15	5	15	5	15	5	15	5	15	5	15
P-ILC	X-axis	0.061	0.0201	0.0918	0.0305	0.0767	0.0104	0.1253	0.0345	0.1004	0.0493	0.1509	0.065
DDAILC	X-axis	0.0463	0.0128	0.0157	0.0129	0.0627	0.005	0.0101	0.0046	0.0862	0.0299	0.052	0.0444
PID	X-axis	0.0471		0.0592		0.011		0.0216		0.0915		0.1122	

ROM. Three performance indicators for each participant are calculated by

$$\text{RMSE} = \sqrt{\frac{\sum_{t=1}^{N}\left(\theta^*(t) - \theta_{15}(t)\right)^2}{N}} \tag{4.26}$$

$$\text{Maximum error} = Max(|\theta^*(t) - \theta_{15}(t)|) \tag{4.27}$$

$$\text{Peak error} = \frac{\sum|\theta^*(t) - \theta_{15}(t)|}{2},\ t = 100, 300. \tag{4.28}$$

where two discrete points are selected for calculating an average peak error when the CARR moves to maximum ROM of plantarflexion and dorsiflexion. The detailed tracking performance with the mean value of ten participants are shown in Table 4.2. Under two therapist-resembled trajectories, two ILC methods significantly improve the RMSE and maximum error when compared to PID controller that indicates the control stability and accuracy is optimized via such learning approach. While with dynamic parameter $\Phi_{i,k}(t)$, both criteria have further improved by DDAILC. For the peak amplitude error, the P-ILC performs closely or even worse than PID. It intuitively demonstrates the major drawback of conventional P-ILC, that is, tracking error can not be effectively converge during later period of learning. On the contrary, by introducing the PPD, this problem can be solved while DDAILC can provide effective error compensation with a peak error under 0.01 rad.

Detailed statistical analysis results are shown in Figure 4.9, with mean value of all participants and their standard deviations (SD) for three indicators. The improvements on RMSE has been further verified, while the SD of employing P-ILC and DDAILC are smaller than using PID. For the maximum error, the peak error of P-ILC reveals its drawback and DDAILC successfully avoid such performance degradation. Besides, the standard deviation of PID for maximum error is large, indicating that the control performance is affected by different participant. For the learning based methods, especially DDAILC, the standard deviations is small which able to provide a more reliable control performance.

4.5 Conclusion

In this chapter, a data-driven adaptive iterative learning controller is proposed for the CARR to achieve repetitive ROM training. Due to the modelling difficulty of PMs, the dynamic linearization approach is introduced and the rigorous mathematical proof is given to guarantee the convergence and the boundedness of the algorithm. Experimental studies consist of passive training with and without human participants under two therapist-resembled movements. Compared to P-ILC and PID controllers, with or without participants involved, proposed DDAILC has significant improvement on the tracking performance which maintains the tracking error under 9% of the desired trajectory.

4.6 Chapter Summary

To meet the second objective, this chapter proposes a data-driven adaptive ILC for ankle ROMs training. The CFDL takes a simple form and can represent the I/O relationship of PM, which also shows great potential in other PM-driven devices. Moreover, asymptotic convergence may be acceptable for most piratical scenarios but is not suitable for conducting rehabilitation training. Since large learning transients are likely to cause ankle injuries, monotonic convergence is derived in the controller design. Experimental studies demonstrate the superior performance in conducting ankle ROMs training, i.e., better task completion, stability and small tracking error are achieved.

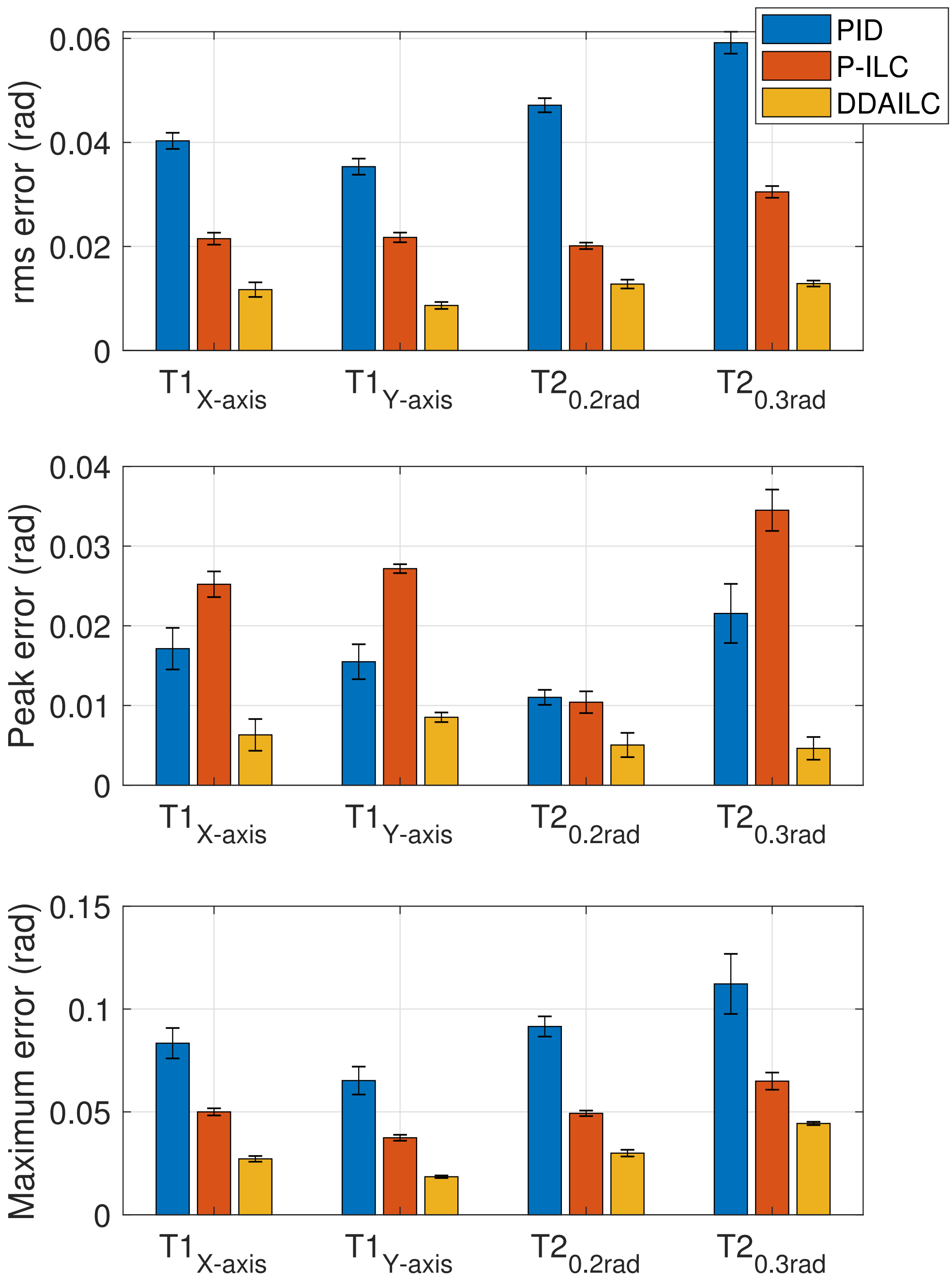

Figure 4.9: The statistical analysis results of ten participants while conducting T1 and T2, performance indicators from top to bottom: RMSE, peak error and maximum error. The coloured bars represent the mean value under different controller and error bars denote the standard error.

Chapter 5

A Phenomenological Pneumatic Muscle Model

To address the modelling difficulty caused by the nonlinearity of PMs, Chapter 4 proposes an adaptive ILC scheme based on the data-driven model that significantly improves the tracking performance of the CARR. However, the control of PM is also confronted with problems such as parametric uncertainty, limited contraction range and unmodelled uncertainties. To solve these problems, a suitable model that describes the dynamic characteristics of PM is essential for designing advanced controllers to further improve the tracking performance. In this chapter, a phenomenological PM model is introduced, identified and validated. Besides, several practical PM control problems are summarized.

5.1 Introduction

PMs are made of nonlinear braided rubber and actuated by pressurized air. Recently, it attracts lots of attention on rehabilitation devices due to its compliance, lightweight and high power/weight output [6, 12, 44, 67, 100]. However, its strong nonlinearity, unknown parameters and unmodelled uncertainties make tracking control difficult. An effective PM model is essential to realize the dynamic characteristics of PMs and also significant for subsequent controller design and stability analysis.

PM modelling has been extensively studied over the last decades and can be normally divided into two categories, i.e., theoretical modelling and phenomenological modelling. The theoretical models describe how the steady force of PM is generated by geometric parameters, internal pressure and friction force [118–120]. The modelling accuracy mainly depends on a large number of experimental fitting results with a certain amount of load. In contrast, phenomenological models establish the relationship between PM output force and the displacement caused by internal pressure change which is employed by many PM controller designs [95, 96, 121]. The phenomenological model of PM can be divided into Colbrunn type [122] and Reynolds type [123]. In particular, the Reynolds type is the most commonly used phenomenological model [95–97, 124], which is an adaption of the Voigt viscoelastic model with parallel arrangement of three elements, i.e., a spring element, a damping element and a contractile force element. The main advantages of the Reynolds model are, 1) it can be easily transformed into a state-space form that is suitable for the implementation of modern control methods; 2) the parameters are all pressure-dependent that simply the identification procedure.

In existing studies, the three-element form has been adopted for modelling both self-developed PMs [97, 123] and commercially available PMs [95, 96, 125]. However, model parameters greatly differ from various construction, initial length and inner diameter of PMs. Therefore, parameter identification for a particular PM is significant to characterize its dynamics. Although the same type of PM is employed in [96], the inflation/deflation interval is set as 1 bar which limits its application in practical systems. The pressure interval of the parameter identification process in this chapter will be set as the whole contraction range (0-6 bar).

To obtain the dynamics of applied PM in the CARR design, this chapter details the establishment of a phenomenological PM model with a three-element form. Specifically, Section 5.2 introduces the modelling procedures and parameter identification results are presented in Section 5.3. In Section 5.4, experimental validations and discussions regarding practical PM control problems are given.

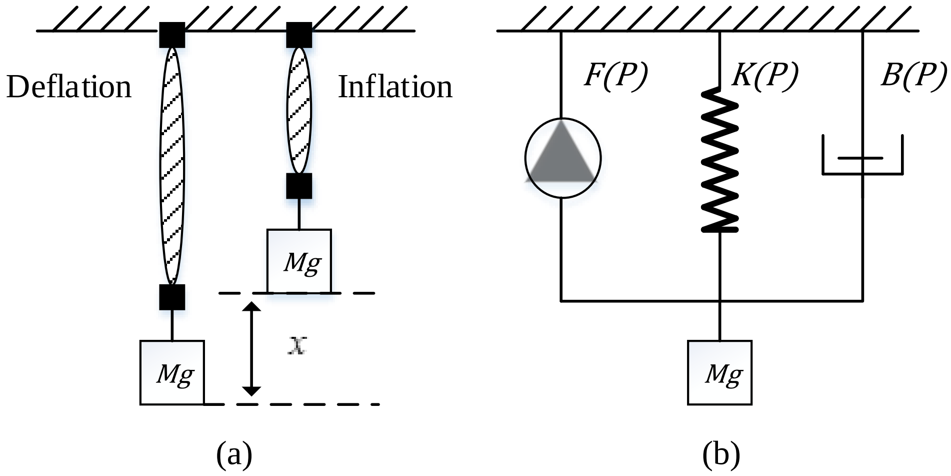

Figure 5.1: (a) Operational principle of PM. (b) The three-element model.

5.2 The Three-element Phenomenological Model

Considering the PM vertically drives a load as shown in Figure 5.1(a). The phenomenological model with three elements [123] is presented in Figure 5.1(b). Each element can be written as pressure-dependent polynomials so that a proportional valve can handle the control task. Letting x_s be the PM position, the dynamic under three-element form is described as

$$M\ddot{x}_s + B(P)\dot{x}_s + K(P)x_s = F(P) - Mg \tag{5.1}$$

where $\dot{x}$ and $\ddot{x}$ is the PM contraction velocity and acceleration. The contractile element $F(P)$ is the effective force that drives the inertial load $M\ddot{x}_s$ and the external load Mg with mass M and gravitational acceleration g. $B(P)$ and $K(P)$ are the pressure dependent damping and spring parameters follow

$$\begin{aligned} B_i(P) &= \sum_{k=0}^{N} B_{ik}P^k, \quad i = 1, 2, 3, \ldots, m \\ K_i(P) &= \sum_{k=0}^{N} B_{ik}P^k, \quad i = 1, 2, 3, \ldots, n \end{aligned} \tag{5.2}$$

where $B_i(P)$ and $K_i(P)$ are i th-order damping and spring elements, respectively; m and n are the orders of polynomials with corresponded coefficients B_{ik} and K_{ik}; N is the order of approximated polynomials. In general, large values of m, n and N result in higher modeling accuracy and increase the computational burden for implementing the model-based controller. In practical application, a simplified model is usually adopted and its capability has been verified by experimental validations [123, 125]. Besides, for different types of PM, e.g., different initial length, diameter and inflating volume, the parameters vary greatly. Therefore, it is necessary to identify specific parameters for the selected PM. The following simplified model is used to represent the dynamic of used PM on the CARR.

$$\begin{aligned} &M\ddot{x}_s + B(P)\dot{x}_s + K(P)x_s = F(P) - Mg \\ &B(P) = B_1P + B_0 = \begin{cases} B_{i1}P + B_{i0} \text{ inflation} \\ B_{d1}P + B_{d0} \text{ deflation} \end{cases} \\ &K(P) = K_1P + K_0 \\ &F(P) = F_1P + F_0 \end{aligned} \tag{5.3}$$

which set $m = n = N = 1$ in (5.2) with damping coefficients B_1 and B_0; spring coefficients K_1 and K_0; contractile coefficients F_1 and F_0. Note that, the damping element is constructed as a piecewise function due to different PM dynamics (inflation/deflation).

5.3 Parameter Identification

To identify the parameters in (5.3), a PM platform is built as shown in Figure 7.1. The PM vertically drive the load and has a maximum contraction of 0.1 m. The input pressure is controlled by the proportional regulator and the displacement is measured by a displacement encoder (Festo MLO-POT-300). The NI roboRIO is used for data acquisition and sends voltage signal to control the valve. System software is designed on host computer by LabVIEW and sensor calibration is conducted before experiments. The identification procedures consist of the following two steps:

*S*tep 1: Estimation of contractile element $F(P)$ and spring element $K(P)$.

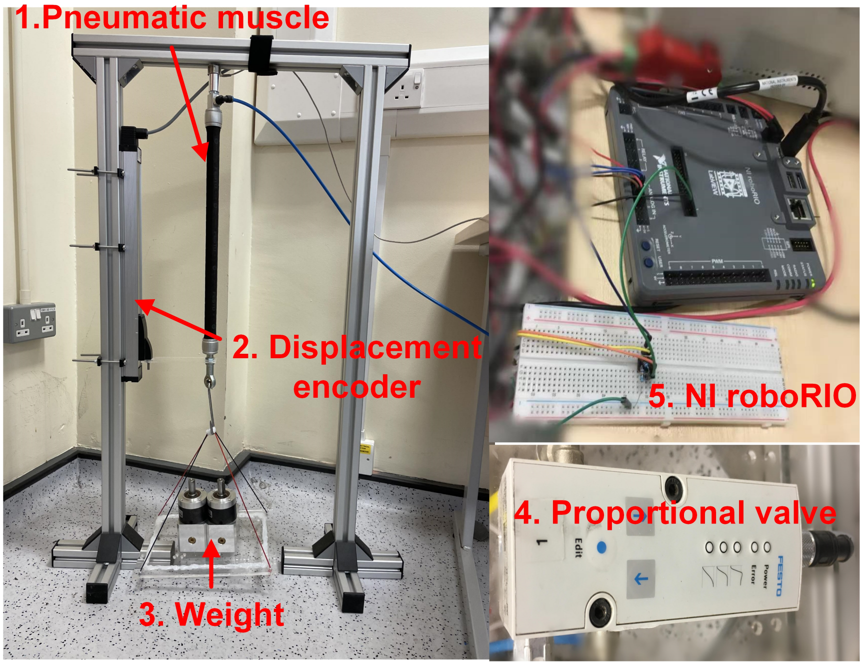

Figure 5.2: The PM platform contains: 1. PM actuator; 2. Displacement encoder; 3. Weight (load); 4. Proportional pressure valve; 5. NI roboRIO.

From (5.3), under the static state ($\dot{x}_s = \ddot{x}_s = 0$), one has

$$K(P)x_s = F(P) - Mg \tag{5.4}$$

Firstly, a group of pressures are set from 0.8 bar to 5.6 bar in steps of 0.8 bar. Under different pressure, a group of displacements x_s are recorded while the load is changing from 3.44 N to 90 N. According to (5.4), the relationships between $F(P)$, $K(P)$ and P can be obtained via least squares fitting algorithm. The fitting processes are repeated with respect to different pressures and results are shown in Figure 5.3. It can be seen that the relationship between $F(P)$ and P is approximately linear in Figure 5.3(a). In Figure 5.3(b), the relationship between $K(P)$ and P is piecewise linear.

*S*tep 2: Estimation of damping element $B(P)$.

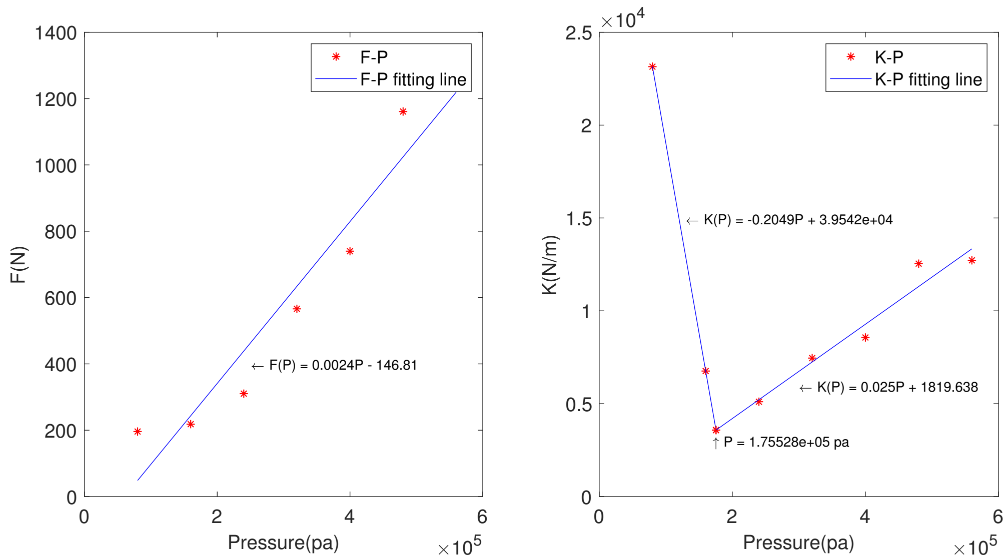

Figure 5.3: $F(P)$ and $K(P)$ fitting result.

From (5.3), the model of PM can be rewritten as

$$\begin{bmatrix} B(P) & K(P) \end{bmatrix} \begin{bmatrix} \dot{x}_s \\ x_s \end{bmatrix} = F(P) - Mg - M\ddot{x}_s \tag{5.5}$$

The identification of $B(P)$ requires a dynamic process and is separated into two cases, inflation (contraction) and deflation (release). For the inflation case, a step response is generated by suddenly removing half of the load. For the deflation case, a step response is generated by suddenly reducing half of the pressure. The displacements of PM are recorded and a low-pass filter is adopted to calculate the contraction velocity and acceleration. The aforementioned procedures are implemented for different pressures from 1 bar to 6 bar in steps of 1 bar, under a load of 49 N. According to (5.5), with the fitting results of $F(P)$ and $K(P)$ in the last step, the relationship between $B(P)$ and P can then be obtained. The fitting results of $B(P)$ is presented in Figure 5.4, where the variation for each single phase is rather large and it is difficult to be fitted with a single function. Therefore, a centre line is estimated via a least squares fitting algorithm to represent the nominal relationship between $B(P)$ and P, where two dash lines represent the data variation ranges [95, 97].

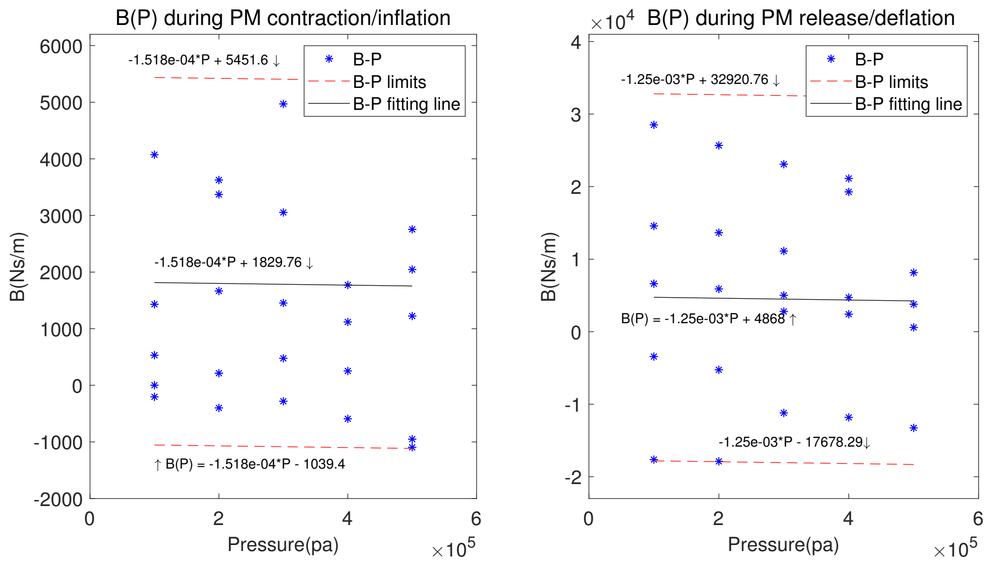

Figure 5.4: $B(P)$ fitting result.

Through above steps, the identified PM model is given by

$$
\begin{aligned}
&F(P) = F_1 P + F_0 = 0.0024P - 146.8 \\
&B(P) = \begin{cases} B_{i1}P + B_{i0} = -1.52 \times 10^{-4}P + 1829.76 \\ B_{d1}P + B_{d0} = -1.25 \times 10^{-3}P + 4868.4 \end{cases} \\
&K(P) = \begin{cases} K_{l1}P + K_{l0} = -0.205P + 39542 \\ \quad 0 < P \leq 1.75528 \times 10^5 Pa \\ K_{h1}P + K_{h0} = 0.025P + 1819.6 \\ 1.75528 \times 10^5 Pa < P \leq 6 \times 10^5 Pa \end{cases}
\end{aligned} \tag{5.6}
$$

where two sets of parameters B_{i1} and B_{i0}; B_{d1} and B_{d0} are used for inflation and deflation, respectively. With the intersection pressure 175 528 pa, two sets of parameters K_{l1} and K_{l0}; K_{h1} and K_{h0} are adopted. It can be found that there is a big difference between two sets of $K(P)$ which can cause switched problem during operation. To avoid it, an initial pressure is usually applied in advance while the loss of PM tension can also be solved.

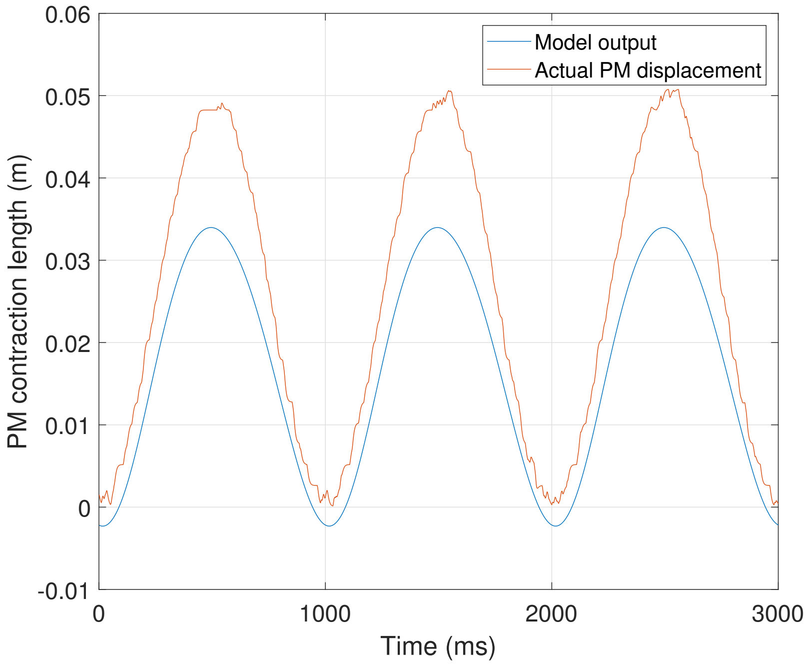

Figure 5.5: Comparison between model output and actual displacement.

5.4 Validation and Discussion

To demonstrate that the identified model (5.6) can represent the actual PM dynamics, the following pressure sequence is entered into the PPR and the identified model

$$P(\text{pa}) = 125000\sin(2\pi ft - \pi/2) + 125000 + 180000 \tag{5.7}$$

where $f = 0.1$ Hz and time interval $t = 0.001$ s. There exists an initial pressure 180 000 pa which leads the PM stay at 0.032 m. The initial pressure is set great than 175 528 pa so that only identified parameters K_{h1} and K_{h0} are used. Considering the static position of PM under $P = 180\,000$ pa as the neutral position, the model output and actual PM displacement are shown in Figure 5.5. The root mean square error between model output and actual PM displacement over a circle is 0.0087 m or about 17.4% of the average total displacement. The model accuracy is close to existing results in [125] which indicates that the identified three-element model can effectively represent the actual PM dynamics.

Various PM controller designs are based on a three-element form and aim to enhance the tracking performance [95, 96, 100, 123]. For its implementation on the CARR, some piratical issues are summarized as follow

- Parametric uncertainty: It has been found that the parameters of $B(P)$ and $K(P)$ take different values when P lie in different ranges [96]. Therefore, to handle parametric uncertainties, robust control methods have been considered in PM controller design [95, 97, 98, 124]. However, under the rehabilitation scenario, there is a lack of studies on designing a robust ILC scheme for gradually enhancing the PM tracking performance.

- Unmodelled uncertainties: The contraction of braid materials will cause friction that is unmodelled in the three-element form [97]. However, existing PM controllers that utilize ILC-based scheme [105, 117, 126] rarely consider the unmodelled uncertainties, an improved performance can be expected by taking it into consideration.

- Training safety: The input saturation of PM has been addressed in [124] for avoiding overlarge internal pressure. In addition, to ensure operational safety from the actuator point of view, the movements of the CARR delivered by PMs should also have guaranteed safety. It can be achieved by restricting the contraction of PM with some predefined bounds during training, which is essential for practical application but rarely considered in PM controller design.

5.5 Chapter Summary

A phenomenological model with a three-element form is introduced to describe PM dynamics. The model parameters are identified and validated via experiments. The model accuracy is similar to the existing results which is over 83% of the average PM displacement. Instead of using data-driven model in Chapter 4, the phenomenological model provides a foundation for improving the tracking performance. Unsolved problems for ILC-based PM control, e.g., robustness, unmodelled uncertainties, and operational safety have been summarized.

Chapter 6

Robust Iterative Learning Control for Pneumatic Muscle with Uncertainties and State Constraints

In Chapter 4, the data-driven method is adopted to represent the PM dynamics. However, as summarized in Chapter 5, several practical issues of PM control also have a significant impact on its tracking performance. To address these issues, this chapter proposes a novel ILC scheme for state tracking of PM with uncertainties and state constraints in this chapter. The three-element PM model in Chapter 5 is adopted with both parametric and nonparametric uncertainties, while full state constraints are considered for enhancing operational safety. To prevent constraint violation, the barrier Lyapunov function (BLF) is employed, which grows to infinity when its arguments approach some limits. By incorporating the BLF with the composite energy function (CEF) approach and ensuring the boundedness of CEF in the closed-loop, it can be assured that those limits are not transgressed. Through rigorous analysis, uniform convergence of PM state tracking errors is guaranteed under the proposed ILC scheme. Simulation study and experimental validation with a PM platform are conducted to illustrate the efficacy of the proposed scheme. Compared to conventional ILC, the proposed scheme can avoid violation of predefined state constraints while the tracking error after convergence is 2.5% of the desired trajectory. Furthermore, the implementation on the CARR indicates that the proposed scheme can restrict the rotation within the predefined ROM bound and tracking accuracy is improved by 18%.

6.1 Introduction

The three-element model [123] is commonly used to describe PM dynamics. However, continuous changes in air pressure bring uncertainties to the model parameters. Besides, PMs suffer from unmodelled uncertainty such as friction which also degrades the control performance. Existing methods to handle these uncertainties include model approximation [96, 127], nonlinear disturbance observers (NDO) [97, 98] and robust control [56, 95]. To deal with parametric uncertainties, an offline model compensator is established in [127]. Alternatively, for state-dependent nonparametric uncertainties, a state estimator is developed in [96] for feedforward controller design. In [97] and [98], NDOs are incorporated with dynamic surface control and proxy-based sliding mode control. Although explicit system parameters are not required, the nonparametric uncertainties are assumed to be bounded by some known value which are hard to justify. Robust control schemes are proposed in [95] and [56]. With backstepping technique [95] and parameter estimation algorithm [56], parametric uncertainties are effectively tackled.

Repetition is a vital feature in actuator applications. Since the pioneering work [128] by Arimoto, iterative learning control (ILC) is known to be effective in handling repetitive control processes [101, 129, 130]. However, its practical implementations on PM systems are rare. The norm-optimal ILC (NOILC) is introduced for PM tracking by minimizing an iteration-dependent quadratic function [126]. Since the computation of matrix gain requires explicit system knowledge, parametric uncertainty can not be handled. Recent study [117] establishes a data-driven model for PM and achieves position tracking by model-free adaptive iterative control (MFAILC). Although the perturbation of uncertain parameters are captured by the data-driven model, the global Lipschitz continuous (GLC) condition is required and nonparametric uncertainty is not considered. To address these problems, the composite energy function (CEF) framework [131] is introduced which is originated from Lyapunov function (LF) and subsequently extended to consecutive learning cycles. The LF approach is applicable to local Lipschitz functions and guarantees the finiteness of system states within a finite interval. To evaluate the parametric learning effect along iteration horizon, an L^2 norm of learning errors is also incorporated into CEF. Based on such construction, the convergence of CEF along the iteration horizon guarantees the boundedness and pointwise convergence of the tracking error.

Due to the extensive applications in compliant robotic devices, the states of PM, i.e., position and velocity are required to be constrained for an enhanced safety. Velocity constraints are considered for two PM-driven rehabilitation devices, where duty cycle modification are adopted [132] and saturation function are designed in [82]. For aforementioned two works, due to the lack of rigorous stability analysis, the performance of the closed-loop system is not theoretically guaranteed. Furthermore, there is no literature reported that considers full state constraints of PMs while maintaining the system stability.

In this chapter, the state tracking problem is considered for PMs. Taking both parametric and nonparametric uncertainties into consideration, a PM model is constructed under three-element form. To tackle uncertainties, a new ILC scheme is proposed that combines conventional ILC law with additional robust part. Unlike previous results, commonly used identical initial condition (i.i.c.) is replaced with more practical alignment condition, the nonparametric uncertainties are assumed to be LLC and only lower bound of the input gain is required for controller design. To enhance the operational safety, full state constraints are considered. A barrier Lyapunov function (BLF) is employed that solves sate constraints by restricting the corresponded tracking errors. With designed CEF incorporated with BLF, uniform convergence of PM state tracking errors are guaranteed, whereas full state constraints will not be violated through the entire learning cycle. Simulation and experimental study are conducted to illustrate the efficacy of the proposed scheme.

The rest of this chapter is organized as follows. Section 6.2 formulates the state tracking problem. The proposed ILC scheme and designed CEF are developed in Section 6.3, with rigorous convergence analysis presented by Section 6.4. Section 6.5 gives the simulation and experimental validation that compares with conventional ILC scheme.

6.2 PM Modelling and Problem formulation

6.2.1 PM Modelling

As discussed in Chapter 5, the PM can be described as the following three-element model:

$$\begin{aligned} & M\ddot{x}_s + B(P)\dot{x}_s + K(P)x_s = F(P) - Mg \\ & B(P) = B_1 P + B_0 = \begin{cases} B_{i1}P + B_{i0} \text{ inflation} \\ B_{d1}P + B_{d0} \text{ deflation} \end{cases} \\ & K(P) = K_1 P + K_0 \\ & F(P) = F_1 P + F_0 \end{aligned} \tag{6.1}$$

where M, P and g are the mass of load, pressure and gravitational acceleration, respectively. The PM position, velocity and acceleration are denoted as $x_s, \dot{x}_s$ and $\ddot{x}_s$. $B(\cdot), K(\cdot)$ and $F(\cdot)$ are pressure-dependent damping, spring and force elements, where $B(\cdot)$ is piecewise due to inflation and deflation. It has been found that B_0, B_1, K_0 and K_1 take different values when P lies in different range [95].

Define an equilibrium point, where the PM stay at position x_0 with pressure P_0. Under the static state, one has

$$K(P_0)x_0 = F(P_0) - Mg. \tag{6.2}$$

Let $u = P - P_0$, $x = x_s - x_0$ and substitute (6.2) into (6.1), it can be derived that

$$M\ddot{x} + (B_1 P_0 + B_1 u + B_0)\dot{x} + (K_1 P_0 + K_1 u + K_0)(x + x_0) = F_1 u + K(P_0)x_0 \tag{6.3}$$

It then follows

$$M\ddot{x} + B(P_0)\dot{x} + K(P_0)x = (-B_1\dot{x} - K_1 x + F_1 - K_1 x_0)u \tag{6.4}$$

To simplify the notation, (6.4) is written as

$$\ddot{x} + \bar{B}\dot{x} + \bar{K}x = (a\dot{x} + bx + c)u \tag{6.5}$$

where $\bar{B} = (B_1P_0 + B_0)/M$, $\bar{K} = (K_1P_0 + K_0)/M$, $a = -B_1/M$, $b = -K_1/M$ and $c = (F_1 - K_1x_0)/M$. For PM dynamics, continuous changes of internal pressure bring uncertainty to the parameters in (6.1), implies that the value of $\bar{B}, \bar{K}, a, b$ and c in (6.5) are unknown. Besides, the unmodelled uncertainty and state constraints are also crucial for a precise and safe PM tracking.

6.2.2 Problem Formulation

Considering the PM system works in an iterative manner with index $i \in \mathbb{N}^+$, rewriting (6.5) as

$$\begin{aligned} \dot{x}_{i,1}(t) &= x_{i,2}(t) \\ \dot{x}_{i,2}(t) &= \theta^T x_i(t) + g(x_i(t))u_i + d(x_i(t)),\ t \in [0, T] \end{aligned} \tag{6.6}$$

where $T > 0$ is the time interval. $\theta = [-\bar{K}, -\bar{B}]^T$ is the parametric uncertainty and $x_i = [x_{i,1}, x_{i,2}]^T$ is a state vector. The control input is defined as u_i with unknown gain $g(x_i) = ax_{i,2} + bx_{i,1} + c$, and $d(x_i)$ represents the unmodelled uncertainty. The following assumptions and properties are given.

Assumption 4 [133] *The twice differentiable desired trajectory $x_{r,1}$ and its first derivative $x_{r,2}$ satisfy*

$$|x_{r,1}| \leq k_{c,1},\ |x_{r,2}| \leq k_{c,2}, \forall t \in [0, T] \tag{6.7}$$

where $k_{c,1}$ and $k_{c,2}$ are two positive numbers. Under the desired control input u_r, the following formulation similar to (6.6) is satisfied

$$\dot{x}_{r,2} = \theta^T x_r + g_r u_r + d_r \tag{6.8}$$

where $x_r = [x_{r,1}, x_{r,2}]^T$ is a desired state vector, $g_r \triangleq g(x_r)$ and $d_r \triangleq d(x_r)$.

Assumption 5 *Functions $g(\cdot)$ and $d(\cdot)$ in (6.6) satisfy LLC, that is*

$$|g(x_i) - g(x_r)| < \alpha_i \|x_i - x_r\| \tag{6.9}$$

$$|d(x_i) - d(x_r)| < \beta_i \|x_i - x_r\| \tag{6.10}$$

where $\alpha_i = \alpha(x_i, x_r, t)$ and $\beta_i = \beta(x_i, x_r, t)$ are known bounding functions and $\|\cdot\|$ is the Euclidean norm for vectors.

Property 1 [95, 123] *For a general PM, $F_1 > 0$ always hold. Since PM's contraction range and frequency of motion are usually small, i.e., $x_{i,1}$ and $x_{i,2}$ are typically small. Thus, the function $g(\cdot)$ satisfies that $g(\cdot) \geq g_{\min} > 0$.*

Property 2 *Reference trajectories are spatially closed, i.e., $x_{r,1}(0) = x_{r,1}(T)$, $x_{r,2}(0) = x_{r,2}(T)$. Actual trajectories are aligned, i.e., $x_{i,1}(0) = x_{i-1,1}(T)$, $x_{i,2}(0) = x_{i-1,2}(T)$.*

For safety concern, system states are required to satisfy

$$|x_{i,1}| < k_{s,1},\ \ |x_{i,2}| < k_{s,2},\ \ \forall t \in [0, T] \tag{6.11}$$

where $k_{s,1}$ and $k_{s,2}$ are positive state constraints. To achieve a complete tracking, it is obvious that $k_{c,1} < k_{s,1}$ and $k_{c,2} < k_{s,2}$. The control objective is to design a robust constrained ILC (RCILC) controller u_i for (6.6) such that $x_{i,1} \to x_{r,1}$ and $x_{i,2} \to x_{r,2}$ as $i \to \infty$. Meanwhile, all signals in the closed-loop system are global uniformly bounded and state constraints (6.11) are satisfied. To prevent states from violating predefined constraints, the BLF is employed and incorporated with the CEF framework. The following lemma formalises a result on the use of CEF in the control design and analysis for repetitive system.

Lemma 2 [134] *For $k_{b,1}$, $k_{b,2} \in \mathbb{R}^+$, let $\mathscr{L} := \{(\ell_1, \ell_2) \in \mathbb{R}^2 : |\ell_1| < k_{b,1}, |\ell_2| < k_{b,2}\}$ be open sets.*

Consider the dynamic system works in an iterative manner

$$\dot{z}_i = f(z_i, t),\ \ i \in \mathbb{N}^+,\ \ \forall t \in [0, T] \tag{6.12}$$

where $z_i := (z_{i,1}, z_{i,2}) \in \mathscr{L}$ and $f : \mathscr{L} \times \mathbb{R} \to \mathbb{R}^2$. Suppose that there exists continuously differentiable function $E : \mathscr{L} \to \mathbb{R}^+$, such that

$$E(z_i) \to \infty \text{ as } |z_{i,1}| \to k_{b,1},\ |z_{i,2}| \to k_{b,2}. \tag{6.13}$$

System (6.12) is under alignment condition, i.e., $z_i(0) = z_{i-1}(T)$ and $z_1(0) \in \mathscr{L}$. If the following inequalities hold:

$$\dot{E}(z_i) < \infty \text{ and } \Delta E(z_i(T)) \leq 0,\ \forall t \in [0, T] \tag{6.14}$$

where $\Delta E(z_i(T)) = E(z_i(T)) - E(z_{i-1}(T))$ is the difference between two consecutive iterations, then one has

$$z_i \in \mathscr{L},\ \forall t \in [0, T] \text{ and } \lim_{i\to\infty} \Delta E(z_i(T)) = 0. \tag{6.15}$$

Proof:
The boundedness of $E(z_1(0))$ and $\dot{E}(z_i) < \infty$ infer that $E(z_1(t))$ is bounded. With the alignment condition, $E(z_i(t))$ can be inferred to be bounded for all $t \in [0, T]$ and $i \in \mathbb{N}^+$. From (6.13), the boundedness of $E(z_i(t))$ indicates that $z_i(t)$ remains in the set $\mathscr{L}$, i.e., $|z_{i,1}(t)| < k_{b,1}$, $|z_{i,2}(t)| < k_{b,2}$, $\forall t \in [0, T]$.
Since $\Delta E(z_i(T)) \leq 0$, $E(z_i(T))$ is non increasing along the iteration horizon, it implies that $\lim_{i\to\infty} E(z_i(T))$ exists. With bounded $E(z_1(T))$, at k-th iteration, one has

$$\lim_{k\to\infty} E(z_k(T)) = E(z_1(T)) + \lim_{k\to\infty} \sum_{i=2}^{k} \Delta E(z_i(T)) \leq E(z_1(T)). \tag{6.16}$$

From the convergence theorem [135], as the sum of series converges to zero, it can be deduced that $\Delta E(z_i(T))$ converges to zero asymptotically, as $i \to \infty$. Thus, it can be seen that (6.15) holds. ■

Define the state tracking error $z_{i,1} = x_{i,1} - x_{r,1}$, $z_{i,2} = x_{i,2} - \sigma_i$ and $\sigma_i = x_{r,2} - \kappa_1 z_{i,1} \cos^2(\frac{\pi z_{i,1}^2}{2k_{b,1}^2})$, where $\kappa_1 > 0$ is a constant and σ_i is commonly used as stabilization term in the conventional adaptive controller design [133]. Note that $z_{i,2}$ is a fictitious error consists of the second order state error $\dot{z}_{i,1} = x_{i,2} - x_{r,2}$ and an additional term

σ_i. If $z_{i,1} \to 0$ as $i \to \infty$, $z_{i,2}$ will approach the real state error $\dot{z}_{i,1}$. In our subsequent design, the transformation from state constraints to corresponded error constraints are used, that is

$$|z_{i,1}| < k_{b,1}, \ |z_{i,2}| < k_{b,2}, \ \forall t \in [0, T] \tag{6.17}$$

where $k_{b,1}$ and $k_{b,2}$ are defined as constraints on $z_{i,1}$ and $z_{i,2}$ which are chosen by

$$\begin{aligned} k_{b,1} &\leq k_{s,1} - k_{c,1} \\ k_{b,2} &\leq k_{s,2} - k_{c,2} - \kappa_1 k_{b,1}. \end{aligned} \tag{6.18}$$

Remark 6 *Instead of GLC condition in PM controller designs* [117, 136, 137]*, LLC condition is considered in this study. The* i.i.c. *is a general assumption in ILC theory* [101]*, i.e., $z_{i,1}(0) = z_{i,2}(0) = 0$. From a practical point of view,* i.i.c. *can hardly be met in various circumstances. Therefore, the more realistic alignment condition is adopted in this study.*

Remark 7 *In optimization-based ILC, the system input, output and state constraints are transformed into matrix inequality and control law is designed by solving the constrained optimization problem* [138–140]*. In virtue of energy-based nature, the CEF incorporated with BLF is adopted to handle state constraints as shown in* Section 5.3.

6.3 Controller Design and CEF

6.3.1 Controller Design

The state error vector is defined as $\bar{z}_i = [z_{i,1}, \dot{z}_{i,1}]^T$ and the following control law is designed

$$\begin{aligned} u_i &= u_i^{ilc} + u_i^r \\ u_i^r &= -\frac{1}{g_{\min}}(\alpha_i |u_i^{ilc}| \mathrm{sgn}(z_{i,2}) \|\bar{z}_i\| + \beta_i \mathrm{sgn}(z_{i,2}) \|\bar{z}_i\| \end{aligned} \tag{6.19}$$

$$+ |\hat{\theta}_i^T|\bar{z}_i \mathrm{sgn}(z_{i,2}) + |\dot{x}_{r,2} - \dot{\sigma}_i|\mathrm{sgn}(z_{i,2}) + \kappa_2 z_{i,2}$$
$$+ z_{i,1}\mathrm{sgn}(z_{i,1}z_{i,2})\cos^2(\frac{\pi z_{i,2}^2}{2k_{b,2}^2})\cos^{-2}(\frac{\pi z_{i,1}^2}{2k_{b,1}^2})) \qquad (6.19\text{a})$$

$$u_i^{ilc} = \mathrm{proj}(u_{i-1}^{ilc}) - p z_{i,2}\cos^{-2}(\frac{\pi z_{i,2}^2}{2k_{b,2}^2}),\ u_0^{ilc} = 0 \qquad (6.19\text{b})$$

$$\hat{\theta}_i = \mathrm{proj}(\hat{\theta}_{i-1}) + q z_{i,2}\bar{z}_i \cos^{-2}(\frac{\pi z_{i,2}^2}{2k_{b,2}^2}),\ \hat{\theta}_0 = 0 \qquad (6.19\text{c})$$

where the control law (6.19) consists of a robust part (6.19a) and two ILC parts (6.19b) and (6.19c) with positive learning gains p and q. The sgn is the signum function [97]. The $\kappa_2 > 0$ is constant and $\dot{\sigma}_i$ is given by

$$\dot{\sigma}_i = \dot{x}_{r,2} - \kappa_1 \dot{z}_{i,1}\cos^2(\frac{\pi z_{i,1}^2}{2k_{b,1}^2}) + \kappa_1 \frac{\pi z_{i,1}^2}{k_{b,1}^2}\sin\left(\frac{\pi z_{i,1}^2}{k_{b,1}^2}\right)\dot{z}_{i,1}. \qquad (6.20)$$

The definition of $\mathrm{proj}(\cdot)$ follows

$$\mathrm{proj}(u^{ilc}) = \begin{cases} u^{ilc} & \text{if } |u^{ilc}| \leq \bar{u}^{ilc} \\ \mathrm{sgn}(u^{ilc})\bar{u}^{ilc} & \text{if } |u^{ilc}| > \bar{u}^{ilc} \end{cases} \qquad (6.21)$$

and

$$\mathrm{proj}(\hat{\theta}) = [\mathrm{proj}(\hat{\theta}_1), \mathrm{proj}(\hat{\theta}_2), ..., \mathrm{proj}(\hat{\theta}_\ell)]^T$$
$$\mathrm{proj}(\hat{\theta}_j) = \begin{cases} \hat{\theta}_j & \text{if } |\hat{\theta}_j| \leq \bar{\theta}_j \\ \mathrm{sgn}(\hat{\theta}_j)\bar{\theta}_j & \text{if } |\hat{\theta}_j| > \bar{\theta}_j \end{cases} \quad j = 1, 2, ..., \ell \qquad (6.22)$$

where $\bar{u}^{ilc} \geq |u_r|_{\sup}$ and $\bar{\theta}_j \geq |\theta_j|_{\sup}$, $\forall j = 1, 2, ..., \ell$ with two known bounds $|u_r|_{\sup}$ and $|\theta_j|_{\sup}$.

Remark 8 *In ILC theory, projector is commonly used for providing uniform convergence instead of pointwise convergence* [131]. *In practice, the bounding information, i.e.,* $|u_r|_{\sup}$ *and* $|\theta_j|_{\sup}$ *can be selected from hardware limits and arbitrarily choosing large bound may lead to divergent learning transient behaviour* [101, 141].

Remark 9 *The control parameters should be set to guarantee both the performance and the stability of the closed-loop system. In particular, fast convergence can be achieved* *by tuning p and q up, but it should not be set too large due to the control saturation and measurement noise in practice. Parameter κ_1 can be determined by error constraint (6.18) based on practical constraint conditions and κ_2 should be tuned accordingly for stabilizing the robust term.*

6.3.2 Composite Energy Function

In this chapter, the following BLFs are introduced [134]:

$$V(z_{i,1}) = \frac{k_{b,1}^2}{\pi}\tan\left(\frac{\pi z_{i,1}^2}{2k_{b,1}^2}\right), \ |z_{1,1}(0)| < k_{b,1} \tag{6.23}$$

$$V(z_{i,2}) = \frac{k_{b,2}^2}{\pi}\tan\left(\frac{\pi z_{i,2}^2}{2k_{b,2}^2}\right), \ |z_{1,2}(0)| < k_{b,2} \tag{6.24}$$

which are positive definite, continuously differentiable in the set $|z_{i,1}| < k_{b,1}$, $|z_{i,2}| < k_{b,2}$ and will approach infinite as $|z_{i,1}| \to k_{b,1}$, $|z_{i,2}| \to k_{b,2}$. Incorporated with the BLF, the CEF is designed as:

$$E_i(t) = V_i^1(t) + V_i^2(t) + V_i^3(t) \tag{6.25}$$

$$V_i^1(t) = \frac{k_{b,1}^2}{\pi}\tan\left(\frac{\pi z_{i,1}^2}{2k_{b,1}^2}\right) + \frac{k_{b,2}^2}{\pi}\tan\left(\frac{\pi z_{i,2}^2}{2k_{b,2}^2}\right) \tag{6.26}$$

$$V_i^2(t) = \frac{1}{2p}\int_0^t g_r(u_i^{ilc} - u_r)^2 d\tau \tag{6.27}$$

$$V_i^3(t) = \frac{1}{2q}\int_0^t (\theta - \hat{\theta}_i)^T(\theta - \hat{\theta}_i) d\tau. \tag{6.28}$$

6.4 Analysis of Convergence Property

Theorem 2 *Suppose Assumption 1–2 and Property 1–2 hold for (6.6). The initial conditions satisfy $|z_{1,1}(0)| < k_{b,1}$, $|z_{1,2}(0)| < k_{b,2}$ and $k_{b,1}$, $k_{b,2}$ are selected according to (6.18). If the controller (6.19) is applied, the following results hold.*

(1) State constraints $|x_{i,1}| < k_{s,1}$ and $|x_{i,2}| < k_{s,2}$ will not be violated.

(2) State tracking errors $z_{i,1}$ and $\dot{z}_{i,1}$ uniformly converge to zero as $i \to \infty$.

(3) All closed-loop signals are bounded.

Proof. The proof consists of three parts. First, the finiteness of the CEF is given which implies the state constraints will not be violated. Then, the decreasing property of the designed CEF is investigated, after which a conclusion of the asymptotical convergence of state tracking errors are drawn in the sense of L^2-norm. Last, the boundedness of involved quantities are given and the uniform convergence of state tracking errors are guaranteed.

Part (1): Finiteness of $E_i(t)$.

Firstly, the boundedness of the time derivative of E_i is presented. Three components of E_i will be studied one by one, start from V_i^1. From (6.26), one has

$$\dot{V}_i^1 = z_{i,1}\dot{z}_{i,1}\cos^{-2}(\frac{\pi z_{i,1}^2}{2k_{b,1}^2}) + z_{i,2}\dot{z}_{i,2}\cos^{-2}(\frac{\pi z_{i,2}^2}{2k_{b,2}^2}). \tag{6.29}$$

In light of $\dot{z}_{i,1} = z_{i,2} - \kappa_1 z_{i,1}\cos^2(\frac{\pi z_{i,1}^2}{2k_{b,1}^2})$ and $\dot{z}_{i,2} = \ddot{z}_{i,1} + \dot{x}_{r,2} - \dot{\sigma}_i$, one can obtain that

$$\dot{V}_i^1 = z_{i,1}z_{i,2}\cos^{-2}(\frac{\pi z_{i,1}^2}{2k_{b,1}^2}) - \kappa_1 z_{i,1}^2 + \cos^{-2}(\frac{\pi z_{i,2}^2}{2k_{b,2}^2})\big(z_{i,2}\ddot{z}_{i,1} + z_{i,2}(\dot{x}_{r,2} - \dot{\sigma}_i)\big). \tag{6.30}$$

From (6.8) and Assumption 2, the first component $z_{i,2}\ddot{z}_{i,1}$ in parentheses are given as follow and some inequalities are satisfied

$$\begin{aligned}
&z_{i,2}\ddot{z}_{i,1} = z_{i,2}(\theta^T\bar{z}_i + (g_i u_i - g_r u_r) + (d_i - dr))\\
&z_{i,2}u_i^{ilc}(g_i - g_r) \leq \alpha_i |z_{i,2}||u_i^{ilc}|\ \|\bar{z}_i\|\\
&z_{i,2}(d_i - dr) \leq \beta_i |z_{i,2}|\ \|\bar{z}_i\|.
\end{aligned} \tag{6.31}$$

Note that $g_i u_i^{ilc} - g_r u_r = u_i^{ilc}(g_i - g_r) + g_r(u_i^{ilc} - u_r)$, according to control law (6.19) and Property 1, it can be inferred that

$$\begin{aligned}
z_{i,2}\ddot{z}_{i,1} =& z_{i,2}\theta^T\bar{z}_i + z_{i,2}u_i^{ilc}(g_i - g_r) + g_r z_{i,2}(u_i^{ilc} - u_r)\\
&- \frac{g_r}{g_{\min}} z_{i,2}(\alpha_i |u_i^{ilc}|\mathrm{sgn}(z_{i,2})\|\bar{z}_i\| + \beta_i \mathrm{sgn}(z_{i,2})\|\bar{z}_i\|\\
&+ |\hat{\theta}_i^T|\bar{z}_i \mathrm{sgn}(z_{i,2}) + |\dot{x}_{r,2} - \dot{\sigma}_i|\mathrm{sgn}(z_{i,2}) + \kappa_2 z_{i,2}\\
&+ z_{i,1}\mathrm{sgn}(z_{i,1}z_{i,2})\cos^2(\frac{\pi z_{i,2}^2}{2k_{b,2}^2})\cos^{-2}(\frac{\pi z_{i,1}^2}{2k_{b,1}^2})) + z_{i,2}(d_i - dr)
\end{aligned}$$

$$
\begin{aligned}
&\leq z_{i,2}\theta^T\bar{z}_i + z_{i,2}(d_i - dr) + z_{i,2}u_i^{ilc}(g_i - g_r)\\
&\quad + g_r z_{i,2}(u_i^{ilc} - u_r) - \alpha_i|z_{i,2}||u_i^{ilc}|\|\bar{z}_i\| - \kappa_2 z_{i,2}^2\\
&\quad - \beta_i|z_{i,2}|\|\bar{z}_i\| - |z_{i,2}||\hat{\theta}_i^T\bar{z}_i| - |z_{i,2}||\dot{x}_{r,2} - \dot{\sigma}_i|\\
&\quad - |z_{i,1}z_{i,2}|\cos^2(\frac{\pi z_{i,2}^2}{2k_{b,2}^2})\cos^{-2}(\frac{\pi z_{i,1}^2}{2k_{b,1}^2})\\
&\leq z_{i,2}\theta^T\bar{z}_i + g_r z_{i,2}(u_i^{ilc} - u_r) - \kappa_2 z_{i,2}^2 - |z_{i,2}||\hat{\theta}_i^T\bar{z}_i|\\
&\quad - |z_{i,2}||\dot{x}_{r,2} - \dot{\sigma}_i| - |z_{i,1}z_{i,2}|\cos^2(\frac{\pi z_{i,2}^2}{2k_{b,2}^2})\cos^{-2}(\frac{\pi z_{i,1}^2}{2k_{b,1}^2}).
\end{aligned}
\tag{6.32}
$$

Substituting (6.32) into (6.30), the second component in parentheses is eliminated which leads to

$$
\dot{V}_i^1 \leq \cos^{-2}(\frac{\pi z_{i,2}^2}{2k_{b,2}^2})(z_{i,2}\theta^T\bar{z}_i + g_r z_{i,2}(u_i^{ilc} - u_r) - |z_{i,2}||\hat{\theta}_i^T\bar{z}_i|) - \kappa_1 z_{i,1}^2 - \kappa_2 z_{i,2}^2. \tag{6.33}
$$

From (6.27) and ILC law (6.19b), it can be derived that

$$
\begin{aligned}
\dot{V}_i^2(t) =&\frac{1}{2p}g_r(u_r^2 + (u_i^{ilc})^2 - 2u_r u_i^{ilc})\\
=&\frac{1}{2p}g_r u_r^2 + \frac{1}{2p}g_r\mathrm{proj}(u_{i-1}^{ilc})^2 - \frac{1}{p}g_r u_r\mathrm{proj}(u_{i-1}^{ilc})\\
&+ \cos^{-2}(\frac{\pi z_{i,2}^2}{2k_{b,2}^2})(g_r z_{i,2}u_r + \frac{1}{2}pg_r z_{i,2}^2\cos^{-2}(\frac{\pi z_{i,2}^2}{2k_{b,2}^2}) - g_r z_{i,2}\mathrm{proj}(u_{i-1}^{ilc}))\\
=&C_1 + \cos^{-2}(\frac{\pi z_{i,2}^2}{2k_{b,2}^2})(g_r z_{i,2}(u_r - \mathrm{proj}(u_{i-1}^{ilc})) + \frac{1}{2}pg_r z_{i,2}^2\cos^{-2}(\frac{\pi z_{i,2}^2}{2k_{b,2}^2}))
\end{aligned}
\tag{6.34}
$$

where $C_1 = \frac{1}{2p}g_r u_r^2 + \frac{1}{2p}g_r\mathrm{proj}(u_{i-1}^{ilc})^2 - \frac{1}{p}g_r u_r\mathrm{proj}(u_{i-1}^{ilc})$ is a finite term.

From (6.28) and ILC law (6.19c), the derivative of V_i^3 follows

$$
\begin{aligned}
\dot{V}_i^3 =&\frac{1}{2q}(\theta^T\theta + \hat{\theta}_i^T\hat{\theta}_i - 2\theta^T\hat{\theta}_i)\\
=&\frac{1}{2q}\theta^T\theta + \frac{1}{2q}\mathrm{proj}(\hat{\theta}_{i-1})^T\mathrm{proj}(\hat{\theta}_{i-1}) - \frac{1}{q}\theta^T\mathrm{proj}(\hat{\theta}_{i-1})\\
&- \cos^{-2}(\frac{\pi z_{i,2}^2}{2k_{b,2}^2})(z_{i,2}\theta^T\bar{z}_i - z_{i,2}\mathrm{proj}(\hat{\theta}_{i-1})^T\bar{z}_i\\
&- \frac{1}{2}qz_{i,2}^2\bar{z}_i^T\bar{z}_i\cos^{-2}(\frac{\pi z_{i,2}^2}{2k_{b,2}^2}))
\end{aligned}
$$

$$
\begin{aligned}
=&C_2 - \cos^{-2}(\frac{\pi z_{i,2}^2}{2k_{b,2}^2})(z_{i,2}(\theta - \text{proj}(\hat{\theta}_{i-1}))^T \bar{z}_i \\
&- \frac{1}{2} q z_{i,2}^2 \bar{z}_i^T \bar{z}_i \cos^{-2}(\frac{\pi z_{i,2}^2}{2k_{b,2}^2}))
\end{aligned} \tag{6.35}
$$

where $C_2 = \frac{1}{2q}\text{proj}(\hat{\theta}_{i-1})^T \text{proj}(\hat{\theta}_{i-1}) - \frac{1}{q}\theta^T \text{proj}(\hat{\theta}_{i-1}) + \frac{1}{2q}\theta^T\theta$ is a finite term. Substituting (6.33)–(6.35) into (6.25) yields

$$
\begin{aligned}
\dot{E}_i =& \dot{V}_i^1 + \dot{V}_i^2 + \dot{V}_i^3 \\
\leq& C_1 + C_2 + \cos^{-2}(\frac{\pi z_{i,2}^2}{2k_{b,2}^2})(z_{i,2}(\text{proj}(\hat{\theta}_{i-1}) - \hat{\theta}_i)^T \bar{z}_i) \\
&+ g_r z_{i,2}(u_i^{ilc} - \text{proj}(u_{i-1}^{ilc})) \\
&+ \frac{1}{2}\cos^{-4}(\frac{\pi z_{i,2}^2}{2k_{b,2}^2})(p g_r z_{i,2}^2 + q z_{i,2}^2 \bar{z}_i^T \bar{z}_i) - \kappa_1 z_{i,1}^2 - \kappa_2 z_{i,2}^2 \\
=& C_1 + C_2 - \frac{1}{2}\cos^{-4}(\frac{\pi z_{i,2}^2}{2k_{b,2}^2})(p g_r z_{i,2}^2 + q z_{i,2}^2 \bar{z}_i^T \bar{z}_i) \\
&- \kappa_1 z_{i,1}^2 - \kappa_2 z_{i,2}^2.
\end{aligned} \tag{6.36}
$$

The definition of $\text{proj}(\cdot)$ ensure that C_1 and C_2 are finite which indicates that $\dot{E}_i < \infty$. According to Lemma 2, E_i is bounded, which guarantees that state error constraints (6.17) hold in the i-th iteration, as the BLF incorporated will be bounded. With $k_{b,1}$ and $k_{b,2}$ selected by (6.18), it is straightforward to show that

$$
\begin{aligned}
&|x_{i,1}| = |z_{i,1}| + |x_{r,1}| < k_{b,1} + k_{c,1} < k_{s,1} \\
&|x_{i,2}| = |z_{i,2}| + |\sigma_i| < k_{b,2} + k_{c,2} + \kappa_1 k_{b,1} < k_{s,2}
\end{aligned} \tag{6.37}
$$

which indicates that state constraints will never be violated over the entire learning cycle.

Part (2): Difference of $E_i(T)$.

Next, the CEF (6.25) is proved to be non-increasing at $t = T$. The difference of $E_i(T)$ between two consecutive iterations is defined as

$$
\Delta E_i(T) = \Delta V_i^1(T) + \Delta V_i^2(T) + \Delta V_i^3(T). \tag{6.38}
$$

From (6.26), $\Delta V_i^1(T)$ is given by

$$\begin{aligned}\Delta V_i^1(T) =& \frac{k_{b,1}^2}{\pi}\tan\left(\frac{\pi z_{i,1}(0)^2}{2k_{b,1}^2}\right) - \frac{k_{b,1}^2}{\pi}\tan\left(\frac{\pi z_{i-1,1}(T)^2}{2k_{b,1}^2}\right) \\ &+ \int_0^T \cos^{-2}(\frac{\pi z_{i,1}^2}{2k_{b,1}^2}) z_{i,1}(\tau)\dot{z}_{i,1}(\tau)d\tau \\ &+ \frac{k_{b,2}^2}{\pi}\tan\left(\frac{\pi z_{i,2}(0)^2}{2k_{b,2}^2}\right) - \frac{k_{b,2}^2}{\pi}\tan\left(\frac{\pi z_{i-1,2}(T)^2}{2k_{b,2}^2}\right) \\ &+ \int_0^T \cos^{-2}(\frac{\pi z_{i,2}^2}{2k_{b,2}^2}) z_{i,2}(\tau)\dot{z}_{i,2}(\tau)d\tau. \end{aligned} \tag{6.39}$$

For convenience, τ will be omitted in the subsequent analysis. With Property 2, one has

$$\Delta V_i^1(T) = \int_0^T \cos^{-2}(\frac{\pi z_{i,1}^2}{2k_{b,1}^2}) z_{i,1}\dot{z}_{i,1} + \cos^{-2}(\frac{\pi z_{i,2}^2}{2k_{b,2}^2}) z_{i,2}\dot{z}_{i,2}d\tau. \tag{6.40}$$

Employing same manner (6.31)–(6.33), it can be obtained that

$$\begin{aligned}\Delta V_i^1(T) \leq \int_0^T & \cos^{-2}(\frac{\pi z_{i,2}^2}{2k_{b,2}^2})(z_{i,2}\theta^T\bar{z}_i + z_{i,2}g_r(u_i^{ilc} - u_r) \\ & - |\hat{\theta}_i^T\bar{z}_i||z_{i,2}|) - \kappa_1 z_{i,1}^2 - \kappa_2 z_{i,2}^2 d\tau. \end{aligned} \tag{6.41}$$

For $\Delta V_i^2(T)$, note that $u_i^{ilc} + proj(u_{i-1}^{ilc}) - 2u_r \leq 2(u_i^{ilc} - u_r)$, it can be inferred that

$$\begin{aligned}\Delta V_i^2(T) \leq& \frac{1}{2p}\int_0^T g_r(u_i^{ilc} - proj(u_{i-1}^{ilc}))(u_i^{ilc} + proj(u_{i-1}^{ilc}) - 2u_r)d\tau \\ \leq& \int_0^T \cos^{-2}(\frac{\pi z_{i,2}^2}{2k_{b,2}^2}) z_{i,2}g_r(u_r - u_i^{ilc})d\tau. \end{aligned} \tag{6.42}$$

For $\Delta V_i^3(T)$, applying the property

$$(a-b)^T(a-b) - (a-c)^T(a-c) = (b-c)^T(b+c-2a)$$

for vector a, b and $c \in \mathbb{R}^{\ell\times 1}$, one can derive that

$$\begin{aligned}\Delta V_i^3(T) \leq& \frac{1}{2q}\int_0^T (\hat{\theta}_i - proj(\hat{\theta}_{i-1}))^T(\hat{\theta}_i + proj(\hat{\theta}_{i-1}) - 2\theta)d\tau \\ \leq& \int_0^T \cos^{-2}(\frac{\pi z_{i,2}^2}{2k_{b,2}^2}) z_{i,2}(\hat{\theta}_i - \theta)^T\bar{z}_i d\tau. \end{aligned} \tag{6.43}$$

Substituting (6.41)–(6.43) into (6.38) yields

$$\Delta E_i(T) \leq \int_0^T -\kappa_1 z_{i,1}^2 - \kappa_2 z_{i,2}^2 d\tau \leq 0. \tag{6.44}$$

According to Lemma 2, it can be inferred that $\Delta E_i(T)$ asymptotically converge to zero. Therefore, from (6.44), one can deduce that $z_{i,1}$ and $z_{i,2}$ asymptotically converge to zero in the sense of L^2-norm, namely

$$\lim_{i\to\infty} \int_0^T z_{i,1}^2 d\tau = 0,\ \lim_{i\to\infty} \int_0^T z_{i,2}^2 d\tau = 0,\ t \in [0,T]. \tag{6.45}$$

Part (3): Boundedness of involved quantities and uniform error convergence.

Part (1) shows that state constraints are equivalently solved by (6.18). With bounded states, the boundedness of $\dot{z}_{i,1}$ and $\dot{\sigma}_i$ are clear. Since functions $g(\cdot)$ and $d(\cdot)$ are state-dependent, their boundedness ensure that the robust term u_i^r is also bounded. With bounded u_i, $\dot{x}_{i,2}$ is bounded which implies that $\dot{z}_{i,1} = z_{i,2} + \sigma_i - \dot{x}_{r,1}$ and $\dot{z}_{i,2} = \dot{x}_{i,2} - \dot{\sigma}_i$ are finite. Since $[0,T]$ is a closed set, $z_{i,1}, z_{i,2}$ are uniformly continuous, according to (6.45), $z_{i,1}$ and $z_{i,2}$ uniformly converge to zero, that is

$$\lim_{i\to\infty} z_{i,1}(t) = 0,\ \lim_{i\to\infty} z_{i,2}(t) = 0,\ t \in [0,T]. \tag{6.46}$$

Notice that $\sigma_i \to x_{r,2}$ as $z_{i,1} \to 0$, one has, $z_{i,2} = x_{i,2} - \sigma_i \to x_{i,2} - x_{r,2} = \dot{z}_{i,1}$. Therefore, the second-order state error also uniformly converge to zero, that is

$$\lim_{i\to\infty} \dot{z}_{i,1}(t) = 0,\ t \in [0,T] \tag{6.47}$$

which completes the proof. ■

6.5 Simulation and Experimental Results

6.5.1 Setup and Parameter Identification

The experimental setup of the PM platform is shown in Figure 6.1. The PM (Festo DMSP-20-400N) vertically drive the load and has a maximum contraction of 0.1 m. The input pressure is controlled by a proportional regulator Festo VPPM-6L-V1 and

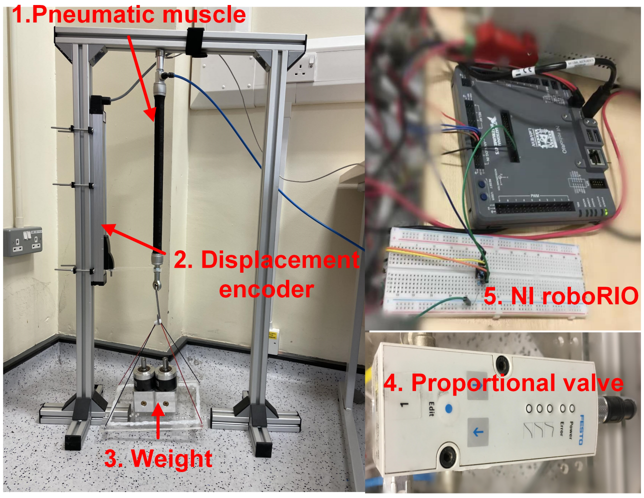

Figure 6.1: The PM platform contains the following components: 1. PM actuator; 2. Displacement encoder; 3. Weight (load); 4. Proportional pressure valve; 5. NI roboRIO.

the displacement of the PM is measured by Festo MLO-POT-300 encoder. The NI roboRIO is used for data acquisition and sends voltage signal to control the valve. The control program is designed on host computer by Labview.

The identification of the system parameters in (5.6) is conducted for simulation. A 49 N load is used and a nominal pressure $P_0 = 1.8 \times 10^5 Pa$ is applied which lead PM to an initial position $x_0 = 0.032\,\text{m}$. Since $1.8 \times 10^5 > 1.75528 \times 10^5$, only parameters k_{h0} and k_{h1} are used. The parameters are

$$
\begin{aligned}
F(P) &= F_1 P + F_0 = 0.0031P - 146.8 \\
B(P) &= \begin{cases} B_{i1}P + B_{i0} = -1.52 \times 10^{-4}P + 1829.4 \\ B_{d1}P + B_{d0} = -1.25 \times 10^{-3}P + 4868.4 \end{cases} \\
K(P) &= K_{h1}P + K_{h0} = 0.025P + 1819.6
\end{aligned} \tag{6.48}
$$

Then, the uncertain parameters in (6.5) can be calculated as, $\bar{B} \in [568.68, 1760.41]$, $\bar{K} \in [1863.92, 6528.4]$, $a \in [3.04, 25] \times 10^{-5}$, $b \in [-6.4, -3.7] \times 10^{-4}$, $c \in [6.13, 6.22] \times 10^{-4}$.

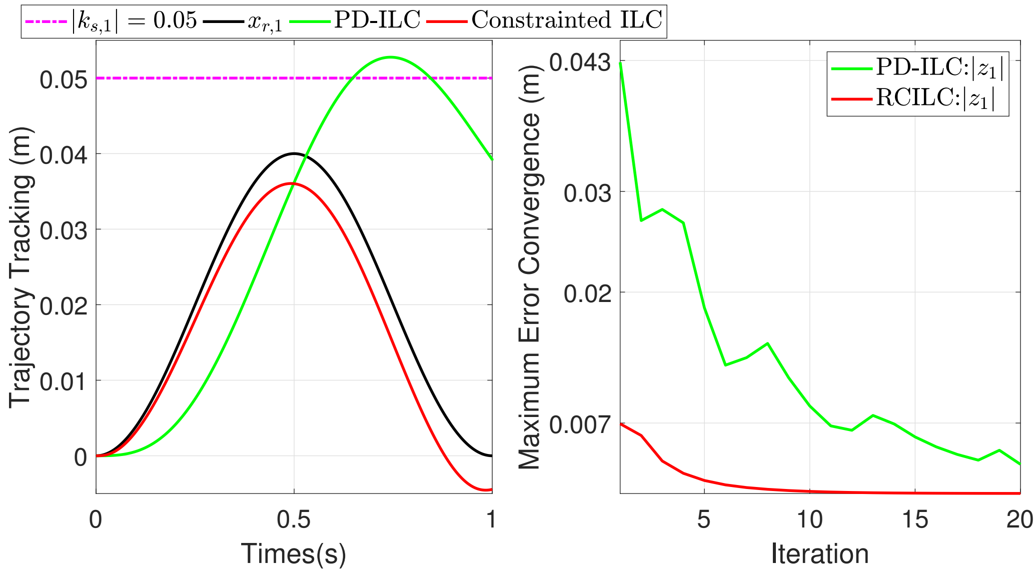

Figure 6.2: Tracking performance of x_1 at first iteration and maximum error convergence.

6.5.2 Simulation Study

This section validates the feasibility of proposed control algorithm before implementing to the practical plant. The time interval in each iteration is 0.001 s and the reference trajectory is an unidirectional sine wave

$$x_{r,1} = 0.02sin(2\pi ft - \frac{\pi}{2}) + 0.02 \tag{6.49}$$

where $f = 1\,\text{Hz}$ and system states are constrained by $|x_1| < 0.05$, $|x_2| < 0.18$. Tracking results are compared with the PD-type iterative learning controller (PD-ILC) [101] under i.i.c.:

$$u_i = u_{i-1} + \Gamma z_{i-1,1} + \Upsilon \dot{z}_{i-1,1} \tag{6.50}$$

where Γ and Υ are two ILC gains. Uncertainty $d(\cdot)$ in (6.6) is modelled as $d(x_i) = m\text{sgn}(x_{i,2}) + nx_{i,2}$, which contains Coulomb and Viscous friction with $m = 0.02$ and $n = 2$. The value of g_{min} and LLC bounding functions α_i and β_i are calculated by fitting results, where $g_{min} = 5.87 \times 10^{-4}$, $\alpha_i = 0.00039$ and $\beta_i = 2.02$. The gains of

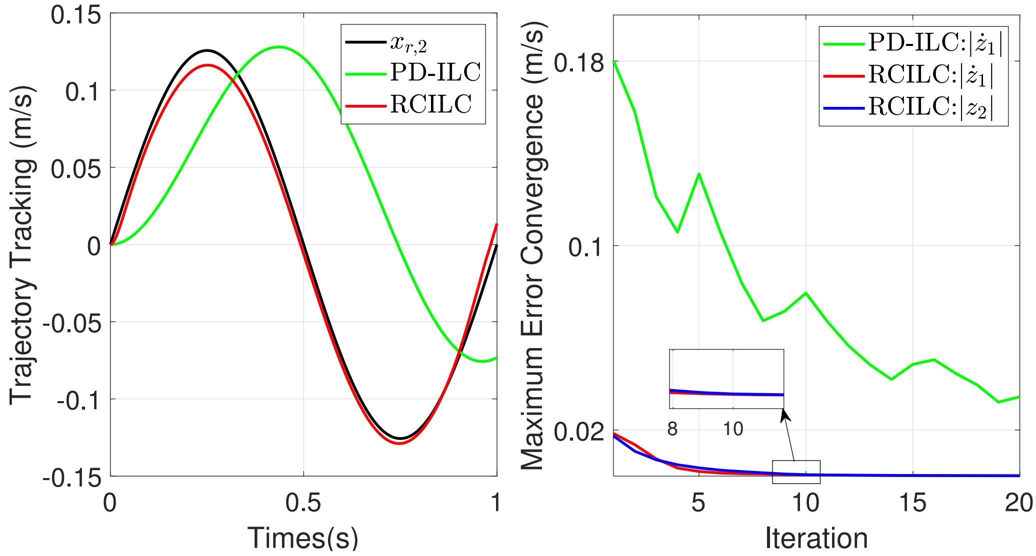

Figure 6.3: Tracking performance of x_2 at first iteration and maximum error convergence.

the proposed ILC have been tuned using trial and error method that follows Remark 4. Following the error bound transformations (6.18), $k_{b,1}$ is first chosen as $k_{b,1} = k_{s,1} - k_{c,1} = 0.01$. To satisfy (6.18), control parameters are set as $k_{b,2} = 0.024$ with $\kappa_1 = 3$. The rest of the parameters are set as $p = 1 \times 10^6$, $q = 5 \times 10^4$ and $\kappa_2 = 10$. For PD-ILC, learning gains are set as $\Gamma = 6 \times 10^6$ and $\Upsilon = 2 \times 10^6$.

In Figure 6.2, tracking performances of x_1 are given. It can be observed that PD-ILC violates the constraint in first iteration while RCILC can restrict the state as expected. From the convergence curve, RCILC reduces the tracking error to $0.007 < k_{b,1}$ and nonuniform convergence can be found for PD-ILC. Figure 6.3 simulates the tracking performance of x_2. PD-ILC has a maximum error of 0.18 in first iteration, and RCILC can reduce it to 0.02 according to the error constraint $k_{b,2}$. Moreover, RCILC uniformly converges $\dot{z}_{i,1}$ and the fictitious state error $z_{i,2}$ will approach to the real state as iteration increases.

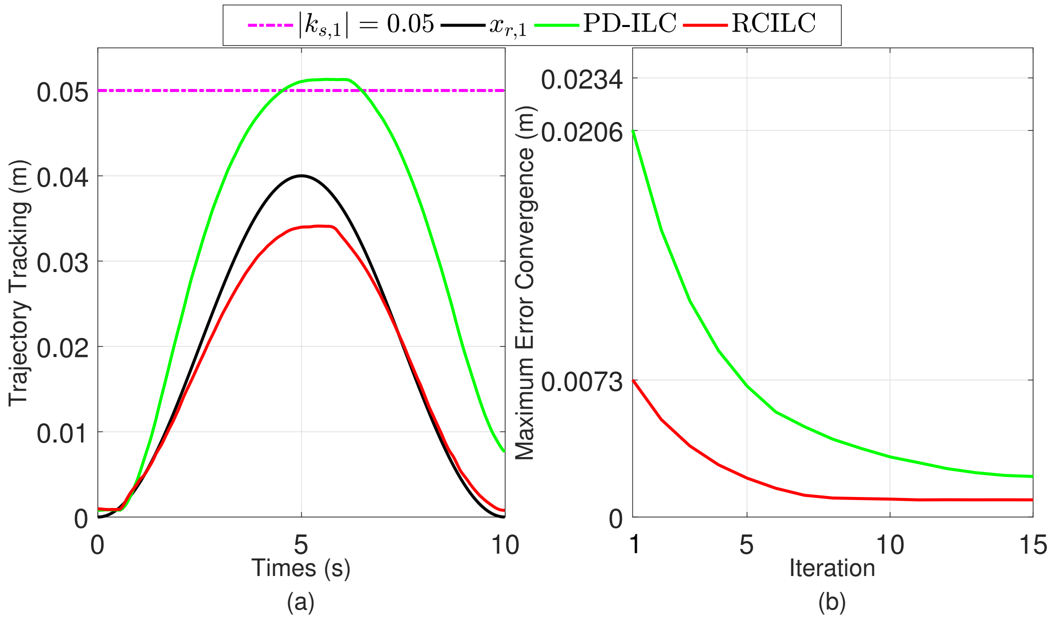

Figure 6.4: (a) Trajectory tracking of x_1 in first iteration; (b) Maximum error convergence within 15 iterations.

6.5.3 Experimental Validation

In the experimental study, PD-ILC and RCILC are both implemented. To meet practical scenario for PMs, $x_{r,1}$ is selected with the same amplitude in (6.49) and $f = 0.1\,\mathrm{Hz}$. For different frequency, experiments will be conducted to validate the performance of the proposed scheme.

The state constraints are defined as $|x_1| < 0.05$, $|x_2| < 0.1$, while error bounds are chosen as $k_{b,1} = 0.01$, $k_{b,2} = 0.035$ with $\kappa_1 = 5$. The ILC gains in (6.19b) and (6.19c) are set as $p = 15$ and $q = 10$, and $\kappa_2 = 8$ in (6.19a). For the PD-ILC, the learning gains are set as $\Gamma = 75$ and $\Upsilon = 15$. Note that the maximum contraction range of the selected PM is $0.1\,\mathrm{m}$, with natural position $x_0 = 0.032\,\mathrm{m}$, the trajectory applied is closed to the maximum control range. Therefore, such constraint is essential for ensuring the system safety.

The trajectory tracking of x_1 in the first iteration of two schemes are shown in Fig. 6.4(a). It can be seen that the state x_1 evidently exceed the constraint $0.05\,\mathrm{m}$ under

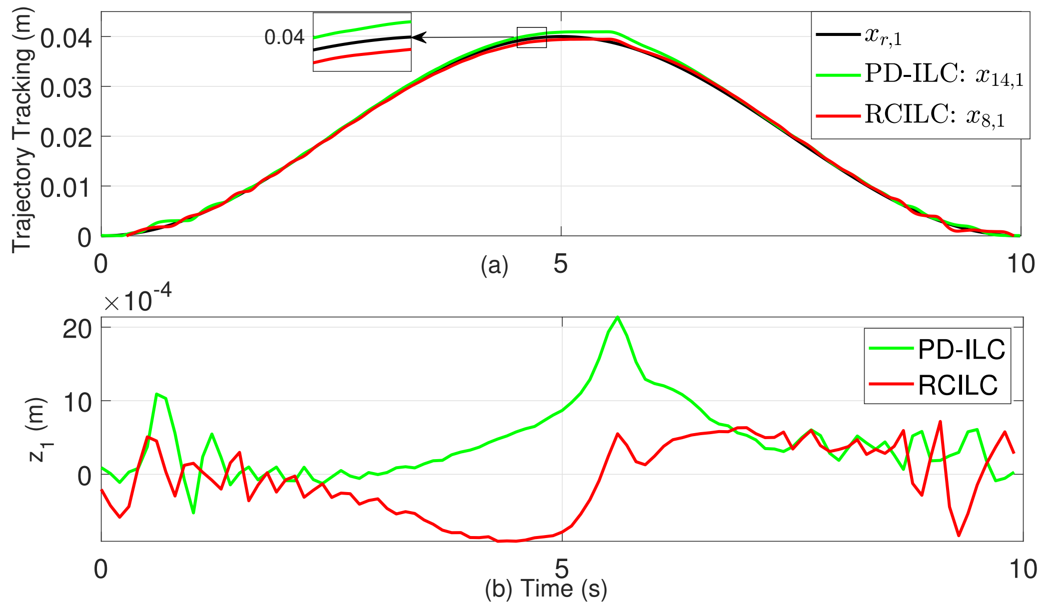

Figure 6.5: Tracking performance of x_1 after different iterations. (a) Trajectory of x_1; (b) z_1.

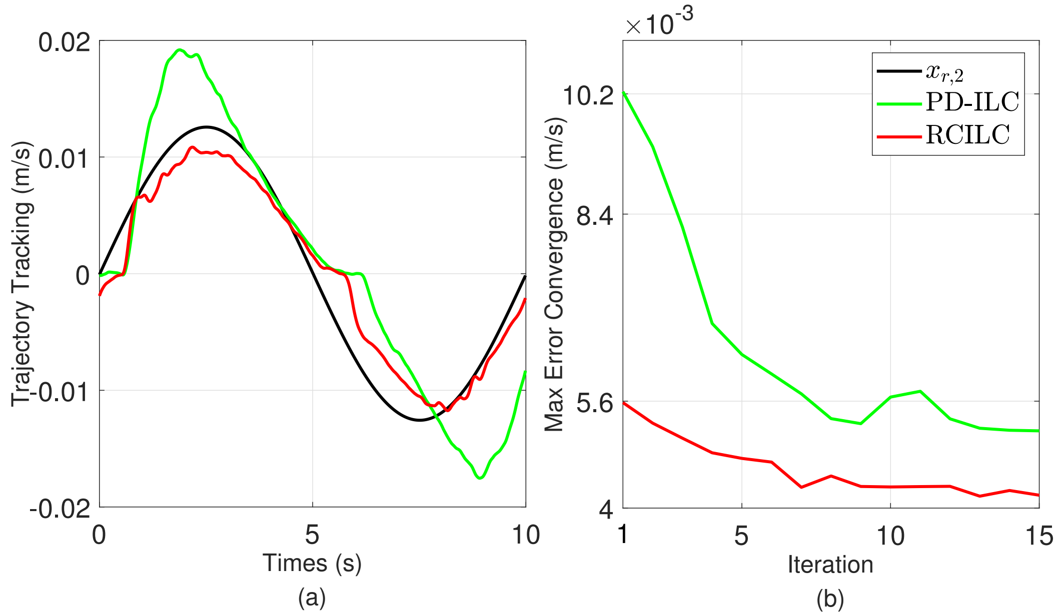

Figure 6.6: (a) Trajectory tracking of x_2 in first iteration; (b) Maximum error convergence within 15 iterations.

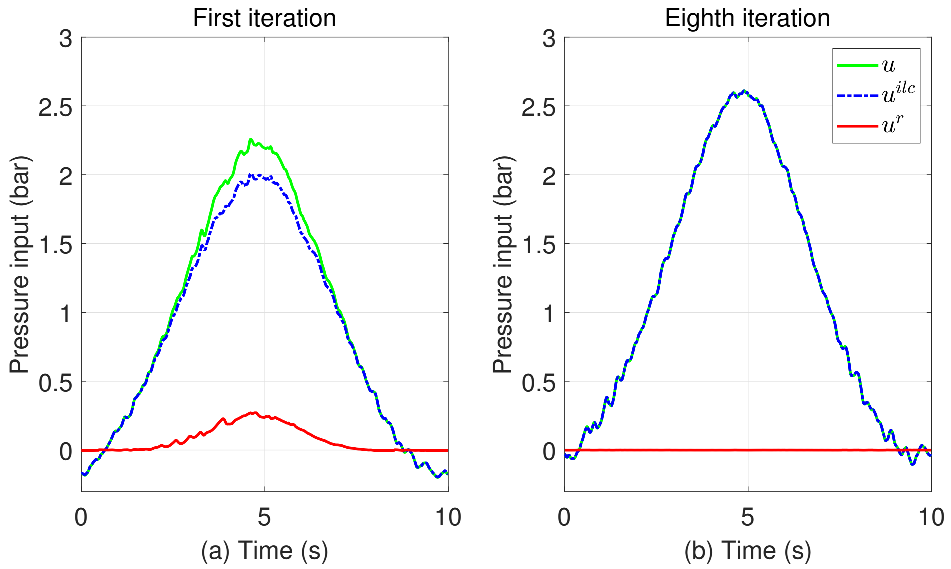

Figure 6.7: Control signal profiles. (a) First iteration; (b) Eighth iteration.

PD-ILC scheme. However, the RCILC can avoid violation of the predefined state constraint by employing the barrier scheme. Figure 6.4(b) shows the maximum error convergence curves, with predefined bound $k_{b,1} = 0.01$, RCILC can quickly reduce the error accordingly implies that the designed BLF for state error is working as excepted. The tracking performance after several iterations is shown in Figure 6.5, both methods can gradually track the reference trajectory. Specifically, the RCILC can reduce the tracking error to 1×10^{-3} m within 8 iterations, while for the PD-ILC, the tracking error is 2×10^{-3} m after 14 iterations. The tracking results of $x_{i,2}$ in the first iteration and maximum error convergence curves are given in Figure 6.6. State x_2 is well in bound for both methods under low frequency, however, the RCILC is able to properly reduce the tracking error in the first iteration and maintain quick convergence speed. Control input signals at the first and eighth iterations are shown in Figure 6.7. With large tracking error, the control effort of the robust part u_1^r is obvious in Figure 6.7(a). When the tracking error converge to a significant small level, the discrepancy between u_i and u_8^{ilc} in Figure 6.7(b) is invisible. It indicates that, as iteration increases, the iterative learning part u_i^{ilc} will dominate the control effort.

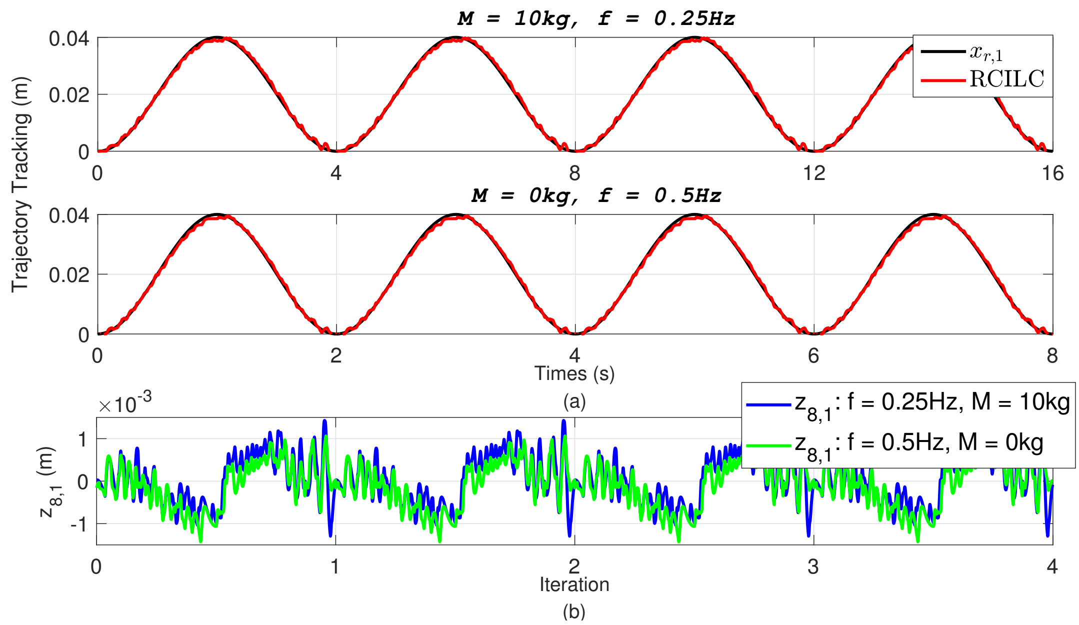

Figure 6.8: The tracking performance of x_1 after 8 iterations. (a) Two scenarios: 1. $M = 10\,\text{kg}$, $f = 0.25\,\text{Hz}$, 2. $M = 0\,\text{kg}$, $f = 0.5\,\text{Hz}$; (b) State tracking error z_1 under both scenarios.

To further verify the performance of the proposed scheme, experimental results while PM drives different load under different frequency are shown in Figure 6.8. The RCILC is able to maintain outstanding tracking performance while the state tracking error converge to approximate $1 \times 10^{-3}\ m$ after 8 iterations for both scenarios. It indicates that the proposed scheme is practicable for various applications.

6.5.4 Implementation on the CARR

In this section, RCILC is implemented on the CARR to further illustrate its performance. Note that the subscript "robot" is used to avoid confusions. Since the CARR contains four PMs, the current task is to control the individual length variation of each PM to achieve a desired end-effector posture. The inverse kinematics (3.1)-(3.4) are adopted to calculate the individual trajectories and determine constraint requirements of each PM. The reference trajectory (rad) of the CARR is defined as

$$x_{r,robot} = 0.2sin(2\pi ft) \tag{6.51}$$

where $f = 0.05$ and $k_{s,robot} = 0.2$. To avoid potential injury when human participant is involved, state constraint $x_{robot} < k_{c,robot} = 0.3$ is required to be satisfied. The transformation from the CARR trajectory to individual PM length variation is given in Figure 6.9. With an amplitude of 0.2 rad, the peak and valley of the PM length are about 600 mm and 570 mm. For the amplitude of 0.3 rad, the peak and valley become 605 mm and 558 mm. To ensure that the length variation will not violate the predefined bound, the state constraint is chosen in terms of the smaller contraction range (peak of the PM length variation). Therefore, for each individual PM constraint, it is chosen that $k_{c,1} = 0.13$ and $k_{s,1} = 0.18$. The length error constraint is then selected as $k_{b,1} = 0.18 - 0.13 = 0.05$. The rest of parameters of RCILC are given by, $p = 18$, $q = 2$, $\kappa_1 = \kappa_2 = 2$ and $k_{b,2} = 0.2$. For comparison, the PD-ILC given in (6.50) is implemented with $\Gamma = 40$, $\Upsilon = 3$. By L'Hôpital's rule, one has

$$\lim_{k_{b,1}\to\infty} \frac{k_{b,1}^2}{\pi} \tan\left(\frac{\pi z_{i,1}^2}{2k_{b,1}^2}\right) = \frac{1}{2} z_{i,1}^2 \tag{6.52}$$

$$\lim_{k_{b,2}\to\infty} \frac{k_{b,2}^2}{\pi} \tan\left(\frac{\pi z_{i,2}^2}{2k_{b,2}^2}\right) = \frac{1}{2} z_{i,2}^2 \tag{6.53}$$

which implies that the employed BLF can be simplified to a quadratic Lyapunov candidate for system without constraint. Subsequently, following control law is constructed with control parameters unchanged and is named as robust iterative learning controller (RILC).

$$\begin{aligned}
u_i &= u_i^{ilc} + u_i^r \\
u_i^r &= -\frac{1}{g_{\min}}(\alpha_i|u_i^{ilc}|\mathrm{sgn}(z_{i,2})\|\bar{z}_i\| + \beta_i \mathrm{sgn}(z_{i,2})\|\bar{z}_i\| + \kappa_2 z_{i,2} \\
&\qquad + |\hat{\theta}_i^T|\bar{z}_i \mathrm{sgn}(z_{i,2}) + \kappa_1 \dot{z}_{i,1}\mathrm{sgn}(z_{i,2}) + z_{i,1}\mathrm{sgn}(z_{i,1}z_{i,2})) \\
u_i^{ilc} &= \mathrm{proj}(u_{i-1}^{ilc}) - pz_{i,2} \\
\hat{\theta}_i &= \mathrm{proj}(\hat{\theta}_{i-1}) + qz_{i,2}\bar{z}_i
\end{aligned} \tag{6.54}$$

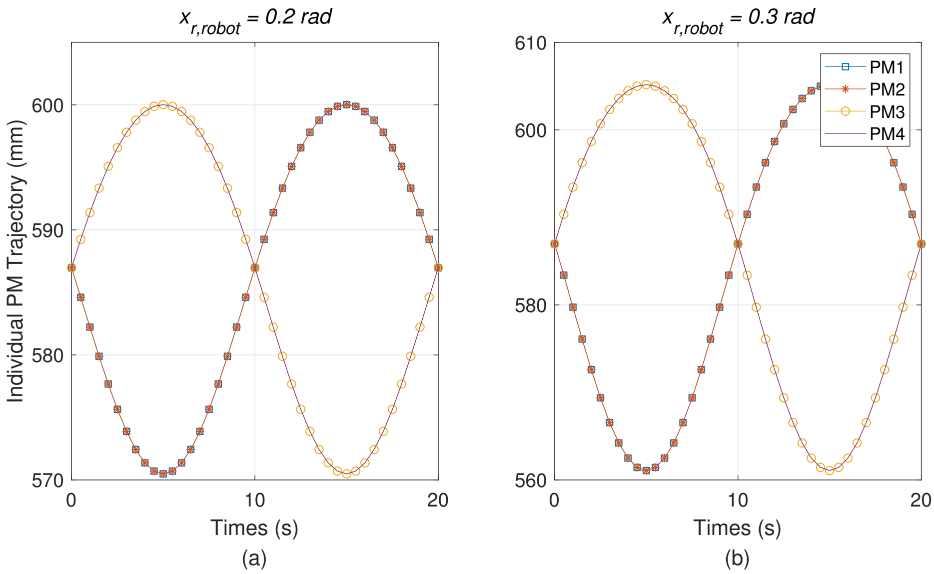

Figure 6.9: PM length under different CARR trajectory. (a) 0.2 rad; (b) 0.3 rad.

In the following experiments, RILC is also implemented such that the effects of incorporating the BLF can be validated.

The CARR repeats the desired trajectory 15 times (total 300 s), the first 10 trajectory tracking results for three controllers are given in Figure 6.10. It can be observed that all three controllers can gradually follow the reference trajectory and the discrepancy between actual and reference trajectory is iteratively decreased. Furthermore, at the beginning of learning, it can be seen that the conventional PD-ILC violates the predefined constraint. The detailed tracking performance in the first iteration and maximum error convergence within 15 iterations are given in Figure 6.11. In Figure 6.11(a), the violation of state constraint for PD-ILC is clear. In Figure 6.11(b), the maximum tracking error of RILC in first iteration is 0.1319 rad $> k_{b,1}$. For RCILC, the maximum tracking error is 0.0948 rad $< k_{b,1}$, which indicates that the BLF incorporated works as expected. Furthermore, the converged error of RCILC after 15 iterations is 0.004 rad while the error of PD-ILC after 15 iterations is 0.04 rad, which has a significant improvement of about 18% of the reference trajectory. Experiments on the CARR demonstrate that the proposed RCILC can effectively avoid the violation

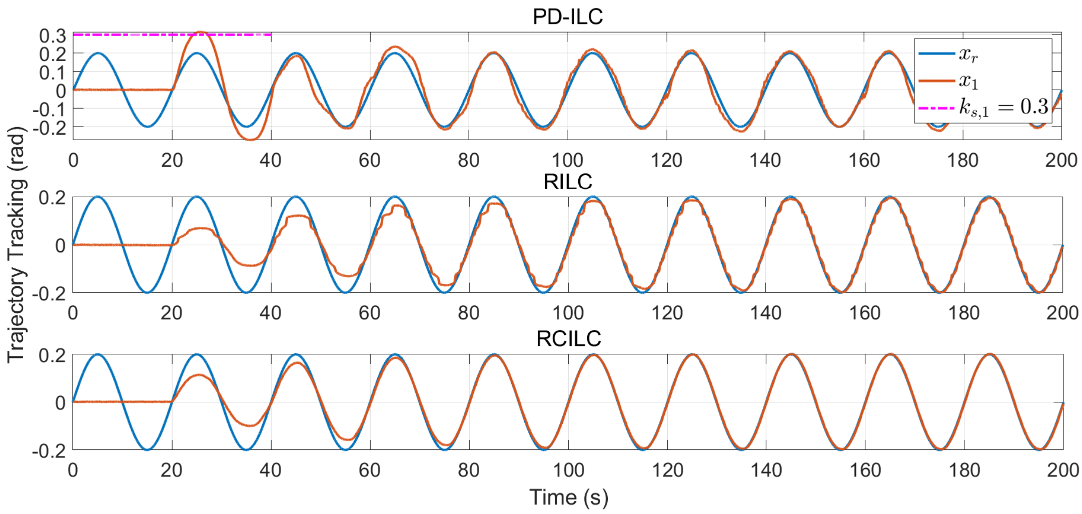

Figure 6.10: Trajectory tracking results of the CARR under PD-ILC, RILC and RCILC during first ten iterations.

of the predefined ROM constraint which is crucial for guaranteeing the training safety of the ankle. Moreover, considering uncertainties in PM controller design also results in more accurate state tracking performance.

6.6 Conclusion

This chapter proposes a new ILC scheme for state tracking of PM actuators. Both parametric and nonparametric uncertainties are tackled and state constraints are considered for enhancing system safety. Differ from conventional ILC schemes, i.i.c. is replaced with alignment condition and nonparametric uncertainties are assumed to be LLC. By constructing the robust feedback, the controller is designed under CEF framework and only the lower bound of the unknown control gain is required. Employing the BLF approaches, the state constraint problems are solved by restricting corresponded state errors. With proper error bounds selection, it is proven that state tracking errors are uniformly converged and state constraints will not be violated over the entire learning cycle. Experimental studies indicate that proposed scheme can effectively avoid viola-

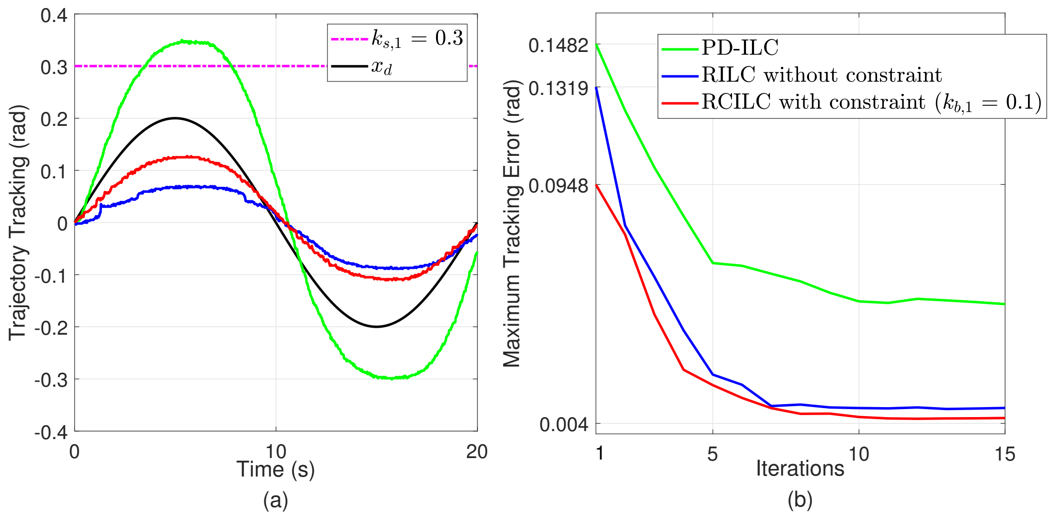

Figure 6.11: Detailed tracking performance. (a) The actual CARR trajectory by implementing PD-ILC, RILC and RCILC with $k_{s,1} = 0.03$ and $k_{b,1} = 0.1$; (b) The maximum tracking error convergence curve within 15 iterations.

tion of state constraint and the maximum error after convergence is 2.5% for single PM. The implementation on the CARR also evidence that RCILC can effectively constrain the rotation within predefined ROM bound and the tracking accuracy is significantly improved when compares to conventional PD-ILC.

6.7 Chapter Summary

To achieve the third objective, this chapter tackles unknown parameters and unmodelled uncertainties of PMs. Together with state constraints related to the safety issue of the CARR, a robust constrained ILC scheme is proposed. As a typical soft actuator, PM has the same properties as many other advanced actuators which are also suitable for the implementation of RCILC. Although most rehabilitation robotics have physical restrictions on joint ROM, this chapter considers state constraints of the robot actuator in controller stability analysis, avoiding excessive design complexity while providing a "double insurance" to fit the rehabilitation scenarios.

Chapter 7

Iterative Impedance Learning Control for Ankle Rehabilitation

In Chapters 4 and 6, nonlinearities, uncertainties and state constraints are considered for improving the tracking accuracy, robustness and training safety of the CARR. After partial recovery of ankle ROMs, active training is required for further promoting patients' rehabilitation outcomes. To obtain better HRI during training, impedance learning control is investigated in this chapter. Under repetitive interaction tasks, the ankle dynamics are described as a time-varying iterative system with unknown mechanical impedance parameters. Subsequently, the gradient following approach and iterative learning algorithm are employed to obtain the desired impedance model. With learned parameters, an inner torque controller with robot dynamic compensation is implemented for tracking the modified trajectory. To ensure that PMs are continuously in tension during training, the force distribution technique is also implemented. Human-involved experiments on the CARR validate the efficacy of the proposed method. In repetitive training with passive ankle stiffness, the proposed controller can learn an optimal set of impedance parameters that provide compliant robot assistance with enhanced task completion.

7.1 Introduction

The ankle joint plays a decisive role in standing, ambulation and balancing, but it is highly susceptible to neurological and musculoskeletal injury [27]. Physiotherapy is essential for the rehabilitation of ankle motion function and it necessitates labour and intensive leading efforts by the physiotherapists. Robot-aided therapy is a promising field that provides a long-term repetitive environment, accurate sensing and reliable records [40, 80, 142]. Differ from the industrial scenario, the rehabilitation robot must be configured for stable, safe and compliant motion in contact with the human. However, unknown and dynamical changes of the human ankle bring along difficulties to interaction controller design [143].

The impedance control proposed by Hogan [86] has been considered as one of the most powerful interaction control methods. The objective of this control concept is to accomplish a desired mechanical impedance at the robot end-effector. However, employing a predefined impedance model tends to be conservative, and a better interaction performance can be expected with other choices [144, 145]. Moreover, numerous industrial applications are mainly aimed at rigid interaction objects which can be characterized by stationary impedance parameters [146–148]. The human ankle dynamics, however, is continuously changing and highly individual-dependent [89]. The learning process is common in motion-based tasks, for instance, when a person pushes the footboard forward, he/she may fail in the beginning due to lack of interaction knowledge, e.g. mass, inertia and friction of the footboard. After several repetitions, the person learns a better set of impedance parameters of his/her ankle while the desired target is achieved as long as the control effort will be minimized.

To reproduce such a human-inspired learning process in interaction controller design, many variable impedance control (VIC) schemes have been proposed. Position-based VICs have been proposed in [91, 149, 150] with force senseless approach, and the impedance model is modified by end-effector velocity at each portion of the task. With force sensor feedback, control schemes in [151, 152] adjust model parameters by constructing an auxiliary interaction force dynamic. However, these methods have an inherent trade-off for position error and iterative force that have limited performance. To mimic the intelligent decision-making process and the physical behaviour pattern of human operators, neural network and fuzzy algorithms are utilized to determine and change the robot impedance during the task [153–155]. Nevertheless, the considerable computation costs of the multi-layer networks bring difficulties to real-time implementation. In addition, existing VICs are rarely validated on rehabilitation robotics and how to fully utilize the repetitive characteristic of tasks is still open.

This chapter proposes a learning impedance controller for enhancing interaction performance when conducting robot-aided ankle rehabilitation. By virtue of the repetitive rehabilitation tasks, the interaction process is described as a linear time-varying (LTV) repetitive system. The gradient following method that decrease a multiple interaction index is introduced, and impedance parameters are iteratively adjusted such that the desired impedance model is learned despite unknown ankle dynamics. A PD-based torque controller with robot dynamic compensation is employed to conduct interaction tasks, and participant involved experiments on the CARR verify the efficacy of the proposed controller.

The rest of this chapter is organized as follows. Section 7.2 formulates the impedance learning problem and a two-loop control conceive. In Section 7.3, the outer learning loop and inner torque loop are designed. Simulations and experiments are then presented in Section 7.4 with the conclusion given in Section 7.5.

7.2 Problem Formulation

Considering the human ankle is interacting with the CARR and the three-dimensional interactive torque is measured by the six-axis load cell. According to Section 3.3 and 3.4, the human-robot dynamics can be modelled as

$$M(q)\ddot{q} + C(q,\dot{q})\dot{q} + G(q) = \tau_r + \tau_h \tag{7.1}$$

where $q \in \mathbb{R}^3$ and $q = [\theta_x, \theta_y, \theta_z]^T$ is the angle vector; $M(q) \in \mathbb{R}^{3\times3}$, $C(q, \dot{q}) \in \mathbb{R}^{3\times3}$ and $G(q) \in \mathbb{R}^3$ denote the inertia matrix, centripetal and Coriolis matrix and gravity vector, respectively; $\tau_r \in \mathbb{R}^3$ is the robot control torque and $\tau_h \in \mathbb{R}^3$ is the interactive torque that applied to the end-effector by the human ankle and adapted from the sensor measurement by Section 3.4.

Assume that the individual is controlling the mechanical impedance of his/her ankle joint that producing the similar trajectory of the robot. The ankle's dynamics can be described by the following mass-damping-spring model

$$M_h\ddot{q} + B_h\dot{q} + K_h q = \tau_h \tag{7.2}$$

where $M_h \in \mathbb{R}^{3\times3}$, $B_h \in \mathbb{R}^{3\times3}$ and $K_h \in \mathbb{R}^{3\times3}$ are inertia, damping and spring matrices, which are all diagonal and positive definite. Unlike stationary interaction, different individuals have divergent configuration for the ankle joint that implies that M_h, B_h and K_h are unknown with respect to the joint position q. Moreover, movement adaption is also common in human joint motion that brings time-varying property to the impedance parameters. Therefore, using fixed impedance parameters for controller design is unconscionable under rehabilitation scenario.

The objective of this work is to achieve better interaction control when conducting robot-aided ankle rehabilitation. In particular, a standard impedance control procedure is adopted with the following target impedance model

$$M_d(\ddot{q}_d - \ddot{q}) + B_d(\dot{q}_d - \dot{q}) + K_d(q_d - q) = \tau_h \tag{7.3}$$

where $M_d \in \mathbb{R}^{3\times3}$, $B_d \in \mathbb{R}^{3\times3}$ and $K_d \in \mathbb{R}^{3\times3}$ are target impedance parameter matrices and $q_d \in \mathbb{R}^3$ is the desired trajectory. For an enhanced interaction, the proper value of M_d, B_d and K_d have to be found that match the human joint model in (7.2). By virtue of the task repetition during rehabilitation, an iterative adaption law is proposed for seeking impedance parameter with previous selection and current feedback. The updating criteria is to minimize a cost function J^k (reinforcement) at $k \in \mathbb{N}^+$ iteration which will be specified later. The parameter learning laws take the following forms

$$\Delta M_d^k = \eta_M(J^k),\ \Delta B_d^k = \eta_B(J^k),\ \Delta K_d^k = \eta_K(J^k) \tag{7.4}$$

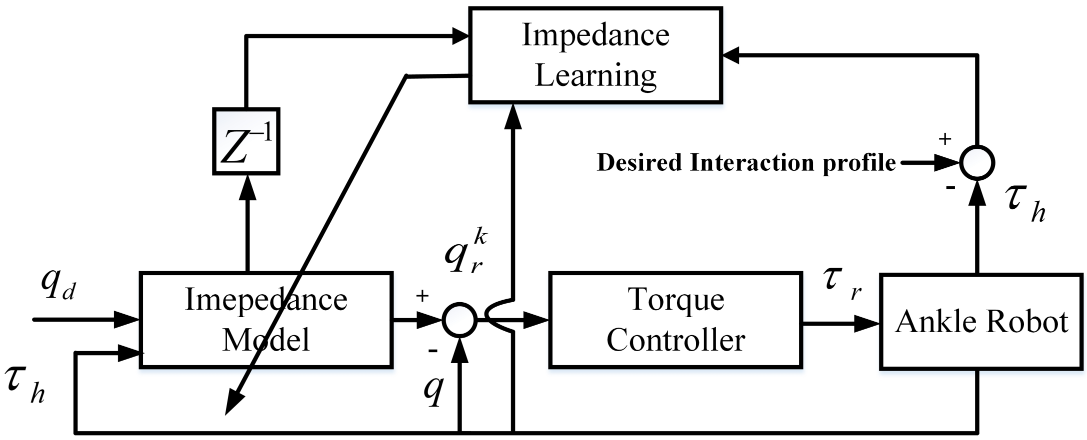

Figure 7.1: Block diagram of the iterative impedance learning controller.

where $\eta_M(J^k)$, $\eta_B(J^k)$ and $\eta_K(J^k)$ are feedback learning terms that contains different components of J^k. ΔM_d^k, ΔB_d^k and ΔK_d^k are the difference of parameter between two consecutive iterations. The initial value M_d^0, B_d^0 and K_d^0 can be selected according to ankle dynamic baseline. With learned impedance parameters, a modified trajectory q_r^k at k-th iteration is derived by

$$M_d^k(\ddot{q}_d - \ddot{q}_r^k) + B_d^k(\dot{q}_d - \dot{q}_r^k) + K_d^k(q_d - q_r^k) = \tau_h. \tag{7.5}$$

Then, the torque control method is developed to make $q \to q_r^k$ in time interval $t \in [0, T], \forall k$. Note that only the modified trajectory will be redefined in (7.3), while the feedback information within current iteration is used to evaluate J^k. The proposed control architecture with outer impedance parameter learning and inner torque control is given in Figure 7.1.

7.3 Controller Design

7.3.1 Iterative Impedance Learning

Since arbitrary selection of M_d may cause instability, M_d is fixed with apparent ankle inertia and only B_d and K_d are learned during rehabilitation. The gradient following method [156] is employed for iteratively decreasing J^k which update B_d^k and K_d^k by

$$\Delta B_d^k = -\alpha_B(\frac{\partial J^k}{\partial B_d^k})^T = -\alpha_B(\frac{\partial \tau_h^k}{\partial B_d^k})^T(\frac{\partial J^k}{\partial \tau_h^k})^T \tag{7.6}$$

$$\Delta K_d^k = -\alpha_K(\frac{\partial J^k}{\partial K_d^k})^T = -\alpha_K(\frac{\partial \tau_h^k}{\partial K_d^k})^T(\frac{\partial J^k}{\partial \tau_h^k})^T \tag{7.7}$$

where α_B and α_K are learning rates. From (7.3), one has $(\frac{\partial \tau_h^k}{\partial B_d^k})^T = \dot{q}_d^T - \dot{q}^{k^T} = \dot{e}^{k^T}$ and $(\frac{\partial \tau_h^k}{\partial K_d^k})^T = q_d^T - q^{k^T} = e^{k^T}$. Due to the unknown ankle dynamics, the derivative $(\frac{\partial J^k}{\partial \tau_h^k})^T$ in (7.6) and (7.7) is not available. To overcome this problem, various reinforcement algorithms for estimating the derivative have been proposed [153, 155, 156]. Take advantage of the repetitive nature of rehabilitation, an alternative way is investigated via iterative learning concept that do not require explicit knowledge of ankle dynamics and aforementioned estimation processes.

To introduce iterative learning concept, (7.2) is rewritten into state-space form [157]

$$\begin{bmatrix} \dot{x}_1 \\ \dot{x}_2 \\ \dot{x}_3 \end{bmatrix} = \begin{bmatrix} 0 & I & 0 \\ -M_h^{-1}K_h & -M_h^{-1}B_h & 0 \\ 0 & 0 & 0 \end{bmatrix} \begin{bmatrix} x_1 \\ x_2 \\ x_3 \end{bmatrix} + \begin{bmatrix} 0 \\ M_h^{-1} \\ I \end{bmatrix} \tau_h \tag{7.8}$$

where $x_1 = q$, $x_2 = \dot{q}$, $x_3 = \int_0^T \tau_h(s)ds$ and I is the unit matrix with proper dimension. Denoting

$$X = \begin{bmatrix} x_1 \\ x_2 \\ x_3 \end{bmatrix} \tag{7.9}$$

$$A = \begin{bmatrix} 0 & I_n & 0 \\ -M_h^{-1}K_h & -M_h^{-1}B_h & 0 \\ 0 & 0 & 0 \end{bmatrix} \tag{7.10}$$

$$B = \begin{bmatrix} 0 \\ M_h^{-1} \\ I_n \end{bmatrix} \tag{7.11}$$

And considering the time-varying property discussed in Section 6.2, the ankle dynamic model (7.2) can be transferred into the following LTV system

$$\begin{aligned} \dot{X} &= A(t)X + B(t)\tau_h \\ Y &= C(t)X \end{aligned} \tag{7.12}$$

where $C(t)$ denotes the relationship between the states (i.e. position, velocity and integration of interactive torque) and the output Y. The following Lemma formalises a result for implementing a D-type ILC on system (7.12).

Lemma 3 [158] *Consider the following LTV system works in an iterative manner*

$$\begin{aligned} \dot{X}^k &= A(t)X^k + B(t)u^k \\ Y^k &= C(t)X^k. \end{aligned} \tag{7.13}$$

Suppose that control input u^k is iteratively updated as

$$u^k = u^{k-1} + \Gamma(\dot{Y}_d - \dot{Y}^k) \tag{7.14}$$

where Y_d is a realizable desired output and learning gain Γ satisfies

$$||I - \Gamma C(t)B(t)|| < 1. \tag{7.15}$$

If $C(t)B(t)$ is full-column rank and identical initial condition $Y^k(0) = Y_d(0)$ is satisfied, uniform convergence of output tracking is guaranteed. That is, $Y^k \to Y_d$ uniformly in $t \in [0, T]$ as $k \to \infty$.

According to Lemma 3, the following updating law is constructed by taking τ_h in (7.12) as control input

$$\tau_h^k = \tau_h^{k-1} - \Gamma(\dot{Y}^k - \dot{Y}_d) \tag{7.16}$$

which indicates that τ_h is updated for iteratively decreasing the error between Y^k and Y_d. Approximately, this error can be defined as the cost function J^k, and measure by $J^k = ||Y^k - Y_d||_2$, where $||\cdot||_2$ denotes two-norm. Notice that all components of Y^k

are available from feedback measure. Similar to the gradient following approach, one obtains

$$\tau_h^k = \tau_h^{k-1} - \alpha_\tau (\frac{\partial J^k}{\partial \tau_h^k})^T. \tag{7.17}$$

Comparing (7.16) and (7.17), the derivative can be approximated by

$$\frac{\partial J^k}{\partial \tau_h^k} = \frac{\Gamma}{\alpha_\tau}(\dot{Y}^k - \dot{Y}_d)^T. \tag{7.18}$$

Substituting (7.18) to (7.6) and (7.7), the learning law is designed as

$$\begin{aligned}\Delta B_d^k &= B_d^k - B_d^{k-1} = -\frac{\alpha_B}{\alpha_\tau}\Gamma \dot{e}^k (\dot{Y}^k - \dot{Y}_d)^T \\ \Delta K_d^k &= K_d^k - K_d^{k-1} = -\frac{\alpha_K}{\alpha_\tau}\Gamma e^k (\dot{Y}^k - \dot{Y}_d)^T.\end{aligned} \tag{7.19}$$

Remark 10 *Parameter learning law (7.19) takes simple form, which is developed based on feedback measures from the interaction task instead of modelling the human ankle. The output gain $C(t)$ plays a vital role in constructing the error based cost function J^k which represents the weight between position, velocity and interactive torque.*

Remark 11 *The condition (7.15) is commonly used in ILC design [101]. For our specified ankle system (7.12), suppose that movement only happens along one DoF, i.e., $-M_h^{-1}$ is now a constant. With proper selected $C(t)$ and learning gain Γ, condition (7.15) is easy to be satisfied. Moreover, the non-zero property of $C(t)B(t)$ also implies that for a higher dimension, non-zero element is exist in each column of $C(t)B(t)$ (full-column rank).*

7.3.2 Torque Control via Force Distribution

The learned parameters B_d^k and K_d^k have been obtained through the outer-loop impedance learning, the modified trajectory q_r^k is obtained according to (7.5). Thus, an inner torque controller is developed in this section to make $q \to q_r^k$. The following control law is constructed that combines the error feedback with the compensation of robot dynamics

$$\tau_r = -K_r s + M(q)a + C(q,\dot{q})v + G(q) - \tau_h \tag{7.20}$$

where

$$\begin{aligned} q_e &= q - q_r^k \\ v &= \dot{q}_r^k - \Lambda q_e \\ a &= \dot{v} = \ddot{q}_r^k - \dot{q}_e \\ s &= \dot{q} - v = \dot{q}_e + \Lambda q_e \end{aligned} \tag{7.21}$$

and K_r is a positive-definite gain matrix, the weight between position error relative to the velocity error is defined with a matrix Λ. The system dynamic under control law (7.20) can then be written as

$$\begin{aligned} M(q)\ddot{q} + C(q,\dot{q})\dot{q} &= -K_r s + M(q)a + C(q,\dot{q})v \\ M(q)\dot{s} + C(q,\dot{q})s + K_r s &= 0 \end{aligned} \tag{7.22}$$

Define the Lyapunov candidate $V = \frac{1}{2}s^T M(q)s$, its derivative can be obtained by

$$\begin{aligned} \dot{V} &= s^T M(q)\dot{s} + \frac{1}{2}s^T \dot{M}(q)s \\ &= s^T(-C(q,\dot{q})s - K_r s) + \frac{1}{2}s^T \dot{M}(q)s \\ &= -s^T K_r s + s^T(\frac{1}{2}\dot{M}(q) - C(q,\dot{q}))s \end{aligned} \tag{7.23}$$

With the property that $\frac{1}{2}(\dot{M}(q) - 2C(q,\dot{q}))$ is skew-symmetric, one has, $\dot{V} \leq 0$. So far, the control torque (7.20) is designed to make $s \to 0$ that implies $q_e \to 0$ and $\dot{q}_e \to 0$ as $t \in [0,T]$. Note that using the sliding error s also eliminate the steady-state error.

Unlike conventional motor-driven rehabilitation robot, CARR utilizes PM as actuator for an enhanced compliance. If PM is not fully in tension, instability may occur which requires conducting force distribution from designed control torque (7.20) to individual actuation force. To fulfil this potential problem, an analytic-iterative force distribution technique [159] is implemented by solving following optimization problem

$$\min_{y} f(y) = (F_0 + Ay)^T (F_0 + Ay)$$
$$\text{s.t. } F_{\min} - (F_0 + Ay) \leq 0 \tag{7.24}$$

where y is the optimal solution; $F_0 = (J^T)^{\dagger} F_m$ with Jacobian matrix J^T and measured actuator force F_m; $A = \text{orthonormal}\{I - (J^T)^{\dagger} J^T\}$ and F_{min} is a non-negative constant.

Remark 12 *The CARR is a self-developed prototype with explicit knowledge of model parameters, thus, (7.20) is constructed by involving direct model compensations. Notice that adaptive control schemes can also be applied in the inner loop if robot dynamics contain uncertainties.*

7.4 Simulation and Experiment

7.4.1 Simulation Study

Simulation studies are first given to demonstrate the necessity of employing force distribution algorithm in the CARR torque controller. A desired trajectory is defined as

$$q_d = \begin{bmatrix} 0.3\sin(2\pi f t) \\ 0 \\ 0 \end{bmatrix} \tag{7.25}$$

where $f = 0.1\,\text{Hz}$. The desired trajectory, its first and second derivative are used to calculate the desired control torque τ_r based on (7.1) without considering the interaction with patient. The desired actuation forces of PMs are then calculated by $F = (J^T)^{\dagger}\tau_r$ where J is calculated via inverse kinematics (3.2)-(3.5). The desired force of four PMs are shown in Figure 7.2, where positive value means pulling and negative value refers to pushing. It can be clearly seen that to achieve the desired trajectory (7.25), pushing forces are required for two PMs which are unpractical. As a consequence, it is essential to calculate feasible force distributions in real-time for the CARR.

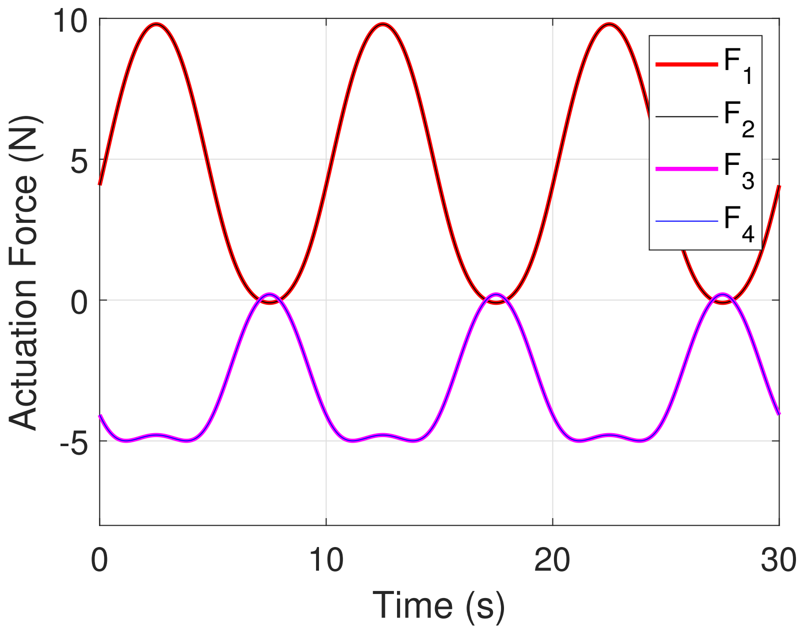

Figure 7.2: Desired force of each PM under trajectory (7.25).

To validate the feasibility of applied analytic-iterative force distribution algorithm, equation (7.26) presents another commonly used closed-form scheme [160] for comparison.

$$y = F_{mean} - (J^T)^{\dagger}(F_m + J^T F_{mean}) \tag{7.26}$$

where F_{mean} is a predefined mean feasible force distribution which can be specified for different applications. Three cases are then considered for both methods with different robot trajectories and interaction torques.

Case 1: $q_x = 0.3\sin(2\pi f t)$, $q_y = q_z = 0$, $\tau_x = 10$ and $\tau_y = \tau_z = 0$.

Case 2: $q_x = 0.3\sin(2\pi f t)$, $q_y = 0.2\sin(2\pi f t)$, $q_z = 0$, $\tau_x = 10$ and $\tau_y = \tau_z = 0$.

Case 2: $q_x = 0.3\sin(2\pi f t)$, $q_y = 0.2\sin(2\pi f t)$, $q_z = 0$, $\tau_x = t$ and $\tau_y = \tau_z = 0$.

The solutions of distributed forces are shown in Figure 7.3. It can be found that both methods can achieve satisfied distributions of each PM with a given interaction torque

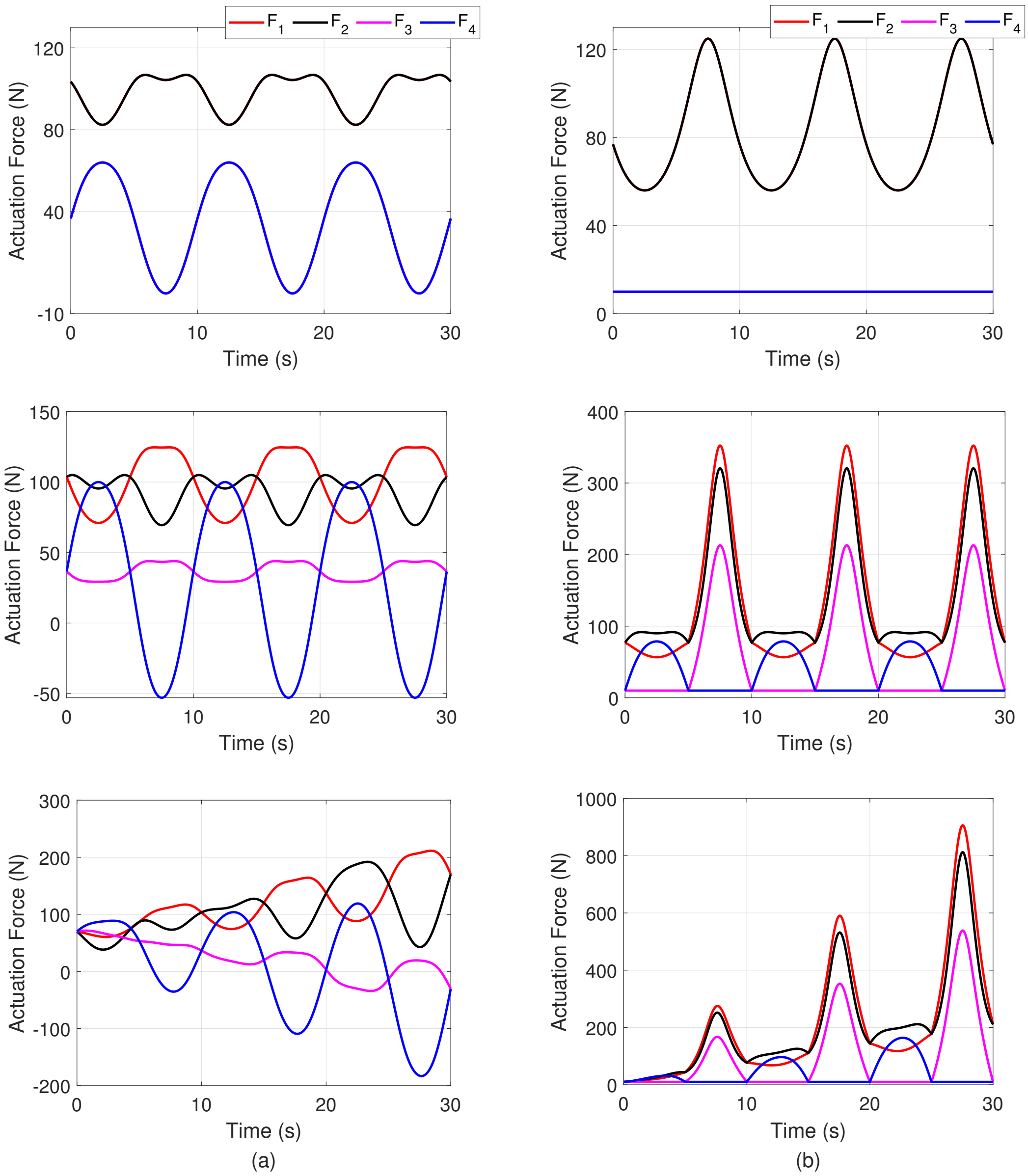

Figure 7.3: Force distribution results of (a) closed-form scheme and (b) analytic-iterative algorithm. Case 1, 2 and 3 are respectively presented from top to bottom in each figure.

along a predefined robot trajectory. However, the two methods present significantly different calculation results due to their inherent characteristics. For the closed-form scheme in Figure 7.3(a), the force distribution is highly related to the selection of F_{mean} (set as 70 N in the simulation). Under constant interaction torque in Case 1 and 2, only PM4 exhibits a small negative force. However, with the increase of the required torque to overcome large interaction torque, the force distributed to each PM increased significantly and even result in a largely negative force for PM3 and PM4 (Case 3), which is undesirable for the PM. For the analytic-iterative algorithm presented in Figure 7.3(b), since the distributed forces are generated based on the predefined F_{min} (set as 10 N in the simulation), all the forces are positive and PMs are in tension. Moreover, as the analytic-iterative approach is developed with an optimisation search algorithm, PMs are only required to maintain a small amount of force during the off working state which prolongs its usage. On the other hand, the closed-form scheme has less computation burden compared to the analytic-iterative algorithm. With the time interval $t = 0.01$, a total of 1000 sampling points are generated during one trajectory. The computational time of the closed-form scheme for three cases are 0.179 s, 0.214 s and 0.234 s. In contrast, the analytic-iterative algorithm requires 0.521 s, 0.571 s and 0.636 s. Therefore, the closed-form scheme is more suitable for robotic systems with strictly defined time bound. Since the embedded controller of the CARR has a maximum sampling frequency of 1000 Hz, the computation speed of the analytic-iterative algorithm (around 0.0005 s) can meet the real-time requirement. Thus, the analytic-iterative algorithm will be adopted in the follow-up experiments for force distribution calculation.

7.4.2 Experimental Validation

To validate the effectiveness of the iterative impedance learning scheme, experiments are conducted with two healthy participants (S1 and S2) that have been approved by the University of Leeds Research Ethics Committee (reference MEEC 18-001). During experiments, desired interaction torque is set to zero indicating that the CARR is trying to minimize participants' effort, i.e., reinforcing compliance. Note that variable interaction profile can also be applied using proposed impedance learning approach. In this experiment, the existence of ankle passive stiffness are used for verification,

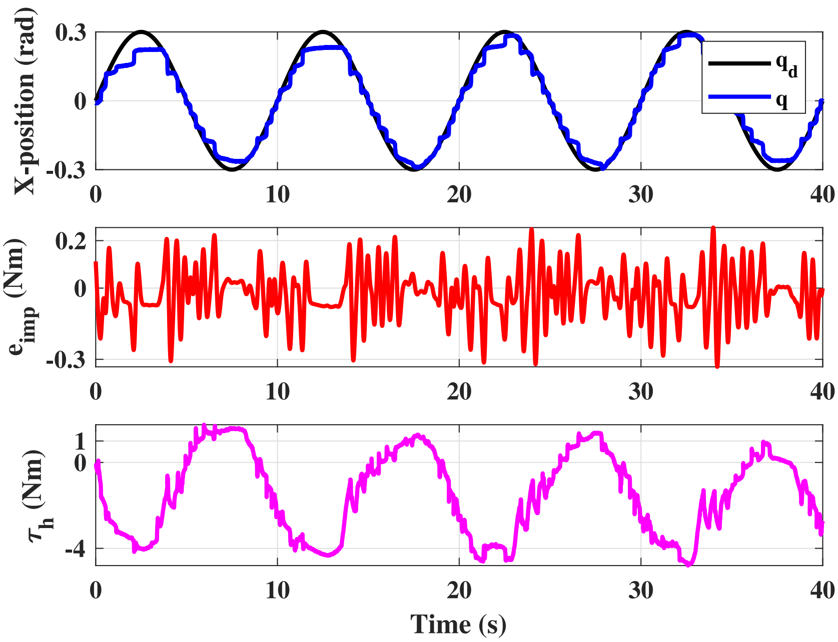

Figure 7.4: Trial of S1 with fixed impedance parameters.

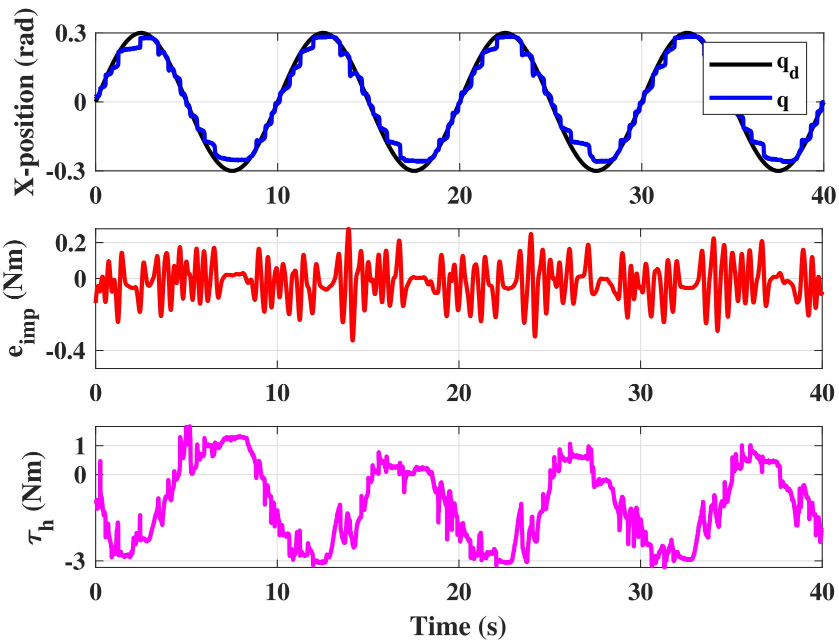

Figure 7.5: Trial of S2 with fixed impedance parameters.

and more active and resistive training scenarios will be conducted further. The same trajectory in (7.25) is applied and the initial impedance parameter in (7.5) are set as $M_d^0 = 0.01$, $B_d^0 = 2$ and $K_d^0 = 40$ according to [89]. To verify the validity of impedance learning scheme, the conventional impedance control scheme with fixed parameters (initial values) is implemented and the training results are shown in Figure 7.4 and 7.5. Each trial contains four repetitive trajectories, i,e, q_r^k, $k = 1, 2, 3, 4$, and feedback gains in (7.20) are set as $\Lambda_p = 30$ and $\Lambda_v = 5$. The impedance error between actual system dynamics and desired impedance dynamics is defined as

$$e_{\text{imp}} = M_d^0 \ddot{e}^k + B_d^0 \dot{e}^k + K_d^0 e^k - \tau_h. \tag{7.27}$$

From Figure 7.4 and 7.5, it can be observed that for both S1 and S2, the position tracking is satisfactory that can almost follow the desired trajectory. Due to the existing of the impedance error, such position error cannot be entirely eliminated. As discussed in Section 2, the predefined impedance parameters is part of the reason for limited interaction performance. Also, the measured interaction torque of both subjects have similar tendency with different magnitude that demonstrates the individual-dependent property.

Subsequently, the iterative impedance learning controller is then tested. The learning gain in (7.19) are set as $\frac{\alpha_B}{\alpha_\tau} = 2$, $\frac{\alpha_K}{\alpha_\tau} = 5$ and $\Gamma = 8$. The output gain in (7.12) is set as $C(t) = [10 \;\; 0 \;\; 1]$ and $Y_d = \begin{bmatrix} q_r^k \\ \dot{q}_r^k \\ 0 \end{bmatrix}$ that gives $J^k = ||10e^k - \int_0^T \tau_h(s)ds||_2$. To obtain the velocity and acceleration of the robot end-effector, tracking differentiators are employed which generates smooth $\dot{q}_r^k$ and $\ddot{q}_r^k$ from q_r^k [161]. For a fair comparison, feedback gains of the inner torque controller Λ_p and Λ_v remain unchanged. The initial value of impedance parameter is utilized in the first iteration as baseline, and also four repetitive trajectories are conducted after. The training results for S1 and S2 are shown in Figure 7.6 and 7.7, and the learned impedance parameters after 4 iterations are also given. It can be seen that both position tracking performance are gradually enhanced as learning process is ongoing. Besides, impedance parameters after learning

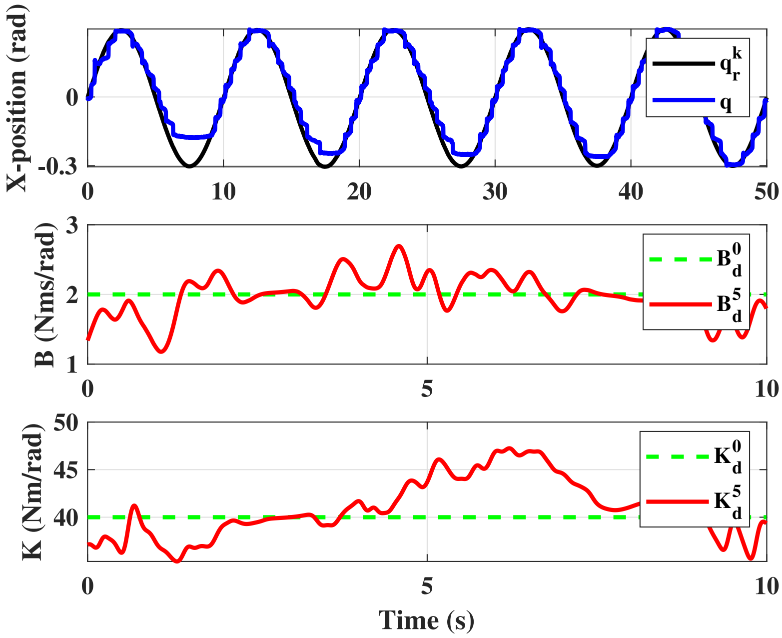

Figure 7.6: Trial of S1 with iterative impedance learning.

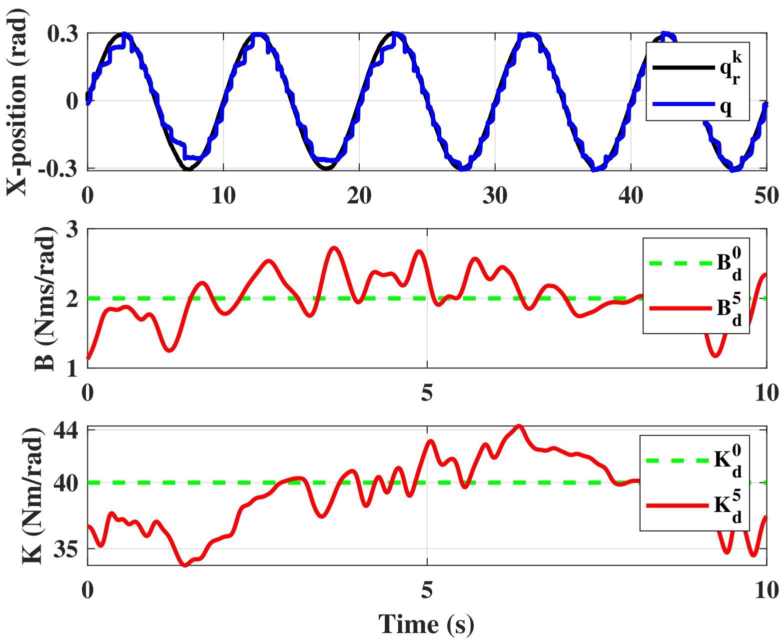

Figure 7.7: Trial of S2 with iterative impedance learning.

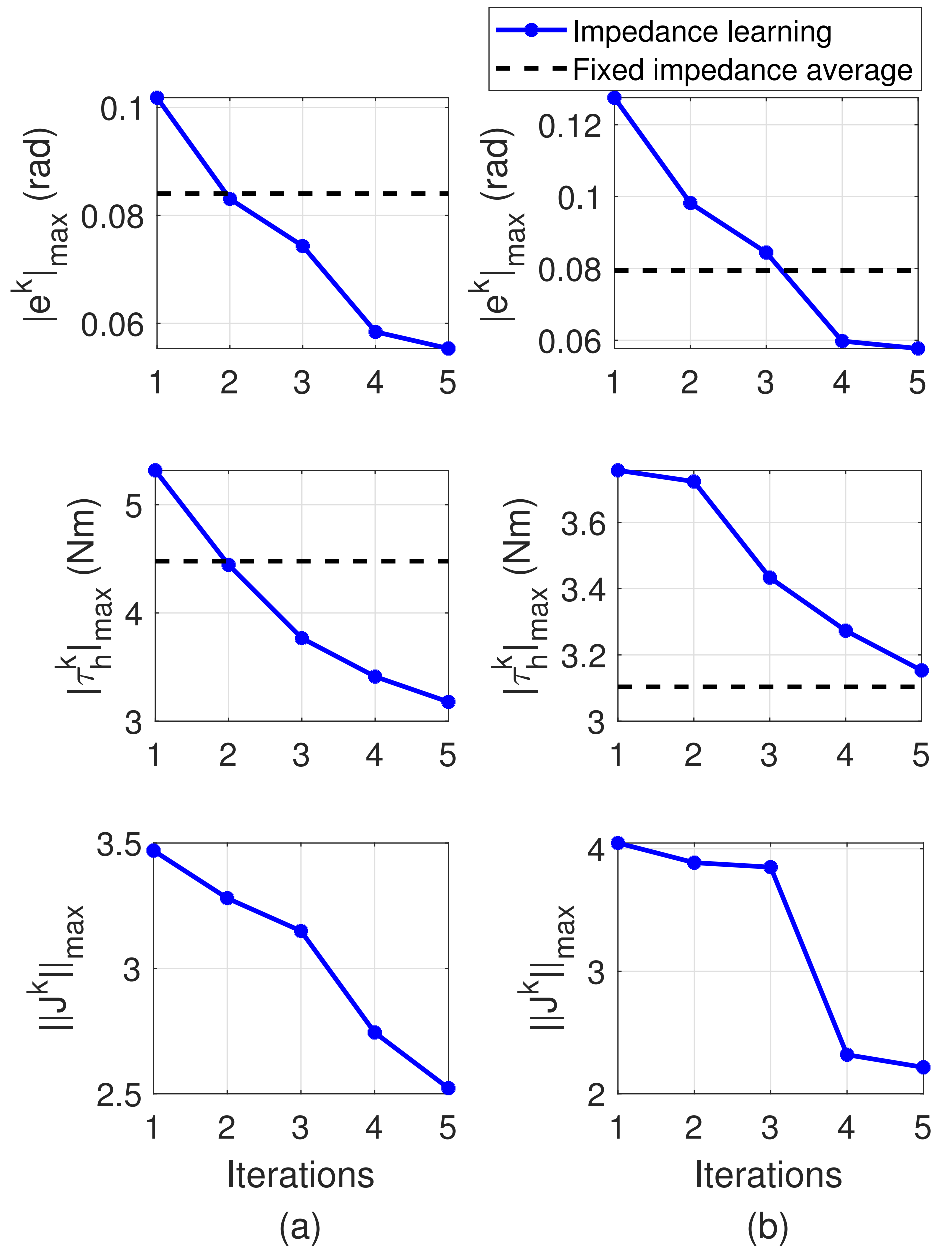

Figure 7.8: Convergence curves of position error, interaction force and cost function. (a) S1; (b) S2.

is different indicating that proposed learning law is able to capture the individual of subjects' ankle dynamic.

To further illustrate the learning process, convergence curves for position error, interaction force and cost function are given in Figure 7.8. The dotted lines demonstrate the average value in the first experiment with fixed impedance parameters. For both subjects, the position errors have been effectively reduced by 8% within four iterations. Since the defined output gain $C(t)$ lays emphasis on minimizing the position error, the expectation of error decreasing is validated. Since the weight of interaction torque is set as 1, the robot compliance remain. Furthermore, the convergence of cost function is different for S1 and S2, indicating that arbitrary selection of learning gain may degrade the control performance due to disparate interaction profiles.

7.5 Conclusion

This chapter focuses on the active training of ankle rehabilitation by designing an iterative impedance learning scheme. A dual-loop structure is constructed with outer impedance learning and inner torque control. The unknown ankle dynamics are described as a time-varying system and an iterative learning law with gradient following approach is introduced for obtaining an optimal set of impedance parameters. Subsequently, a torque controller with force distribution is implemented that ensure PMs are continuously in tension. Compared to conventional impedance control, experimental results on the CARR illustrate that, with a specific weight matrix, task completion can be improved by 8% within 5 iterations and compliant robot movements are retained.

7.6 Chapter Summary

To achieve the fourth objective, this chapter combines an impedance learning scheme with a force-distributed torque controller. The trajectory tracking error and interaction force are jointly considered to be minimized and the force distribution algorithm guarantees that PMs are continuously in tension. Experiments with the CARR illustrate the efficiency of the impedance leaning scheme with potential variability on specifying control objectives with different choices of the weight matrix.

Chapter 8

Progressive Learning Strategies for Ankle Rehabilitation with Quantitative Performance Evaluation

Impedance learning is investigated in Chapter 7 and its performance has been validated. However, the desired interaction profile is still required which is hard to be judged with different individuals. Moreover, clinical studies demonstrate that promoted participation is an important factor to speed up recovery [54, 162, 163]. To address these issues, a progressive learning control strategy with quantitative performance evaluation is proposed. With three indicators, a fuzzy logic system is first designed to determine the training performance during the previous trial. Subsequently, a cost function that contains both tracking error and robot stiffness matrix is constructed. The iterative learning law designed for the stiffness matrix is derived on the basis of fuzzy system output. The control stability and ultimate bound are analysed using Lyapunov theory. Experiments are conducted with ten healthy subjects, the results of performance evaluation, individual error convergence, stiffness matrix learning and changes of robot-assisted torque and interactive torque are discussed. The capability of the progressive learning strategy on promoting active participants is proved.

8.1 Introduction

Post-stroke patients are commonly suffered from ankle dysfunctions that require long-term help from therapists [14]. However, the gap between the numbers of patients and therapists has limited the available rehabilitation care. To solve this issue, robotics have been used to assist the repetitive ankle training [36, 44, 164, 165]. Different from other applications, there exists a large number of interactions during rehabilitation training. Therefore, safe and efficient interaction control becomes one key issue of the ARRs.

For guaranteeing the compliant physical interaction between robots and the environments, impedance control has been adopted for the interaction control by keeping the desired force relationship between the robot and the environment [86, 148, 166]. As a specific design of the impedance control, the admittance control calculates the desired reference trajectory from the desired interaction relationship and the measured interaction force, and the desired reference trajectory is then tracked by using the position tracking controller [36, 146, 155]. When the environment is unknown, some adaptive impedance/admittance controllers have been adopted by using the optimal control methods or the adaptive control methods [43, 153, 167]. However, when the environment is time-varying, designing an appropriate impedance controller still faces grand challenges.

Towards this challenge, ILC has been introduced and take advantage of the repetitive nature of the task. Along the task horizon, ILC can adjust the stiffness parameters trial after trial based on the previous control information. For tackling the situation that the interaction force may be different during each trial, a control law motivated by the human CNS was proposed [168, 169]. The iterative adaptive law was designed to minimize the tracking error and the robot stiffness term. Furthermore, a robot controller simultaneously adapting the stiffness and the reference trajectory and a bio-inspired controller imitating human motor learning properties were provided for the interaction with the time-varying environment [170, 171]. However, the aforementioned studies consider the HRI under a working/operating environment where ILC focuses on the convergence of the system's state as well as the interaction force. Under the rehabilitation scenario, it cannot stimulate the active participation of patients, which limits the rehabilitation outcome.

To overcome this limitation, an idea of ANN has been proposed in [172], which considers the fact that stimulating the patients' motion intention is helpful to their recovery. With the AAN controller, the robot only gives the needed force when the patient's functional capability is not strong enough to complete the training tasks. Reversely, when complete tasks can be achieved, the robot system keeps compliant and follows the motion of the patient. To achieve this idea, a minimal controller was designed for upper limb rehabilitation [54]. The designed controller consists of a sensor-less force observer and an impedance control law. The stiffness parameter of the impedance controller is iteratively updated by the designed updating law, and the stiffness parameter is adjusted concerning the rehabilitation task's motion error. When the patients try to move actively and the motion error is greater than the desired value, the stiffness parameter decreases and the ultimate bound of the allowable tracking error increases, vice versa. Similarly, a greedy ANN algorithm [163] and an iterative ANN strategy [173] are proposed that judges the robot assistance by interaction force measure. The robot assistance is designed to be continuously decreasing such that persistent contributions of the patients are required. From another view of achieving the AAN control, an adaptive human-robot interaction control based on the SEA was proposed in [165, 174]. The designed control method divided the control mode into the robot-in-charge mode and the human-in-charge mode. A smooth switching law was given to guarantee the stability of the whole system on the basis of tracking error feedback. However, the reliability of using a single feedback measure to represent the training state is questionable due to the fact that clinical evaluations normally use multiple variables and empirical ranges for performance evaluation [162, 175].

Krebs et al. [53] first implemented a performance-based progressive robotic therapy with MIT-Manus, where the patient's performance is depicted using the patient's active power and motion accuracy. The stiffness of the robot joints is determined by the patient's performance of the last reaching movement. Papaleo et al. [176] proposed a patient-tailored adaptive therapy for a seven-degrees-of-freedom (DoF) upper limb rehabilitation robot, where a module for the evaluation of patients' biomechanical performance and a module for the modulation of the robotic assistance were included. The quantity of patients' biomechanical performance was evaluated using five kinematic and dynamic indicators that were extracted from sensory signals. Then, the stiffness of the robot controller was adjusted according to the weighted sum of the performance indicators, using a threshold technology. However, there is a lack of studies that combine the progressive approach with the learning controller design. With online learned performance during the previous trial, the behaviour of the robot should be adapted to subject's effect.

In this chapter, a progressive learning framework is designed that the iterative learning algorithm is constructed based on the output of a fuzzy performance evaluation module. To obtain comprehensive and quantitative training performance, three indicators are used as fuzzy system input and primary experiments are conducted for constructing the membership functions. Except for the cost function designed for minimizing tracking error, an extra term that represents the minimization of the robot stiffness matrix is also included. As a result, better performance will lead to a large allowable tracking error and lower robot stiffness matrix which maximizes the promotion of active participants. To demonstrate the efficacy of proposed control strategies, experiments with ten healthy subjects are conducted.

The rest of this chapter is as follows. Section 7.2 formulates the control problem and explains the concept of error bound modification. The fuzzy performance evaluation is given in Section 7.3 with progressive learning controller design and stability analysis presented in Section 7.4. The experimental results are demonstrated in Section 7.5 as well as the conclusion of this chapter in Section 7.6.

8.2 Problem Formulation

Considering the same dynamic model as given in (7.1)

$$M(q)\ddot{q} + C(q,\dot{q})\dot{q} + G(q) = \tau_r + \tau_h. \tag{8.1}$$

In addition to improving trajectory completion in the case of compliance, another key point of active rehabilitation training is to quantitatively evaluate the participant's performance and adapt the result to an optimal robot assistance, so as to promote maximum participancy. In the clinical environment, participant's performance is usually determined by the scoring system, which includes joint kinematic, dynamic and sensory information [175]. With multiple sets of tests, results contain multiple measured variables are weighted into the scoring system to generate the overall performance. To reproduce above procedure, this chapter consists of two parts: 1) Constructing an online evaluation block that quantifies the training performance during each trial; 2) Designing the learning controller that progressively adjust the robot assistance based on the performance evaluation of previous trial. A baseline controller is first given to illustrate the basic concepts.

8.2.1 Baseline Controller

Based on the control law given in (7.20), the following baseline controller is first given

$$\tau_r = -K_r s + M(q)a + C(q,\dot{q})v + G(q) - P_c\tau_h \tag{8.2}$$

where

$$\begin{aligned}
q_e &= q - q_d \\
v &= \dot{q}_d - \Lambda q_e \\
a &= \dot{v} = \ddot{q}_d - \dot{q}_e \\
s &= \dot{q} - v = \dot{q}_e + \Lambda q_e
\end{aligned} \tag{8.3}$$

and K_r is a positive-definite gain matrix, the weight between position error relative to the velocity error is defined with a matrix Λ. P_c is a scaling coefficient to weight the robot's torque and interactive torque. It has been proved in Chapter 6, if robot dynamics are known as a priori and interactive torque is completely eliminated, the sliding error $s \to 0$ as $t \to \infty$. However, there always exist model uncertainties and measuring error that make s only converges to a close neighbour of 0. Denoting the model uncertainties and measuring error as d and following same procedures in (7.22) and (7.23), one has

$$M(q)\dot{s} + C(q, \dot{q})s = -K_r s + d \tag{8.4}$$

and

$$\dot{V}(s) = -s^T K_r s + s^T d \tag{8.5}$$

Using the equality $x^T y \leq \|x\|\|y\|$ and define $\lambda_{min}(K_r)$ as the minimal eigenvalue of K_r. It can be deduced that

$$\begin{aligned} \dot{V}(s) &= -s^T K_r s + s^T d \\ &\leq -\lambda_{min}(K_r)\|s\|^2 + s^T\|d\| \\ &\leq (\theta - 1)\lambda_{min}(K_r)\|s\|^2 - \theta\lambda_{min}(K_r)\|s\|^2 + s^T\|d\| \end{aligned} \tag{8.6}$$

where a constant $\theta \in (0, 1)$ is introduced. From (8.6), a sufficient condition for $\dot{V}(s) \leq (\theta - 1)\lambda_{min}(K_r)\|s\|^2 \leq 0$ is

$$\begin{aligned} &-\theta\lambda_{min}(K_r)\|s\|^2 + s^T\|d\| \leq 0 \\ \Rightarrow &\|s\| \geq \frac{\|d\|}{\theta\lambda_{min}(K_r)} \end{aligned} \tag{8.7}$$

which indicates that s is uniformly ultimately bounded. This ultimate bound can be calculated by the fact of existing following bounding functions

$$\alpha_1\|s\| \leq V(s) \leq \alpha_2\|s\| \tag{8.8}$$

which can be used to calculate the bound B_u as

$$B_u = \alpha_1^{-1}(\alpha_2(\|r\|)) \tag{8.9}$$

where r satisfies $\dot{V}(s) \leq 0 \; \forall \|s\| \geq r \geq 0$. It is natural to assume that the lumped term $\|d\|$ is bounded, and due to the fact that the inertia matrix itself is positive definite and bounded, the following inequality is derived

$$\frac{1}{2}\lambda_{min}(M(q))\|s\|^2 \leq V(s) \leq \frac{1}{2}\lambda_{max}(M(q))\|s\|^2 \tag{8.10}$$

where $\lambda_{min}(M(q))$ and $\lambda_{max}(M(q))$ are the minimum and maximum eigenvalue of the inertia matrix throughout the entire given task. Invoking (8.7) and (8.8), $\alpha_1\|s\|$, $\alpha_2\|s\|$ and r can be specified accordingly. Thus, the ultimate bound for $\|s\|$ is

$$\begin{aligned} B_u =& \alpha_1^{-1}\left(\frac{\lambda_{max}(M(q))\|d\|^2}{2\theta^2\lambda_{min}(K_r)^2}\right) \\ =& \sqrt{\frac{\lambda_{max}(M(q))\|d\|^2}{\lambda_{min}(M(q))\theta^2\lambda_{min}(K_r)^2}} \end{aligned} \tag{8.11}$$

From (8.11), there are two factors that determine the size of the ultimate bound. The first factor is the value of the gain matrix K_r, i.e., the ultimate bound of s will decrease if larger value of K_r is selected, vice versa. This is because K_r represents the virtual stiffness of the robot joint. Another factor is the lumped term d which can be considered as the external disturbances. Large d results in poor tracking performance that increases the ultimate bound. For rehabilitation tasks, it is difficult to choose a consistent K_r for different subjects. To solve this problem, this chapter introduce an online performance evaluation model with experimental data support and progressively adapt the value of K_r to motivate subjects' participants.

8.3 Performance Evaluation

8.3.1 Performance Indicator

To quantitatively evaluate the performance of a previous trial, three indicators are used that contain both kinematic and dynamic measures. The extraction of kinematic indicators are based on embedded encoders and they are conceived to assess the following movement features: i) accuracy, ii) direction and iii) smoothness. On the other hand, dynamic measures provided by load cell provide us with the torque generated by the subject's ankle during continuous interactions. In detail, these indicators are

- *Mean absolute tracking error* (e_{mabs}) [53]:

$$e_{mabs} = \frac{1}{N}\sum_{i=1}^{N} \text{abs}(q_i - q_{r,i}) \tag{8.12}$$

  where the mean value of absolute tracking error is calculated with each discrete trajectory point.

- *Mean absolute measured torque* ($\tau_{h,mabs}$) [176]:

$$\tau_{h,mabs} = \frac{1}{N}\sum_{i=1}^{N} \text{abs}(\tau_{h,i}) \tag{8.13}$$

  where the mean value of absolute torque is obtained from discrete load cell measures.

- *Participant Ratio* ($\text{PR}_{\%}$) [54]:

$$\text{PR}_{\%} = \frac{1}{N}\text{count}(\tau_{h,i}\dot{q}_{d,i}) \times 100\%, \quad \text{if } \tau_{h,i}\dot{q}_{d,i} > 0 \tag{8.14}$$

  where the function count$(\cdot)$ output the number of samples that meet the condition $\tau_{h,i}\dot{q}_{d,i} > 0$, indicating that the directions of $\tau_{h,i}$ and reference velocity $\dot{q}_{d,i}$ are the same for each discrete sample.

The e_{mabs} evaluates the completeness of a given reference trajectory, indeed, movement error is likely to be a driving signal of motor learning [177]. Active participant is proved to be an important factor for neural plasticity during rehabilitation [178]. Therefore, indicator $\tau_{h,mabs}$ is introduced to evaluate the overall iteration performance of a trial. Since the direction of the measured torque is not considered in the indicator $\tau_{h,mabs}$, the intentional movement of subjects whether they are actively following or resisting the given trajectory can not be judged. To this end, the indicator $\text{PR}_{\%}$ is introduced that counts the sample points which have the same signs for $\dot{q}_{d,i}$ and $\tau_{h,i}$. These indicators are independently used in the existing literatures [53, 54, 176] with similar forms. To avoid the reliability and stability issues caused by employing single indicator, a fuzzy logic system will be designed in the next section to realize performance fusion.

8.3.2 Fuzzy Fusion

The FLS is able to map the typical nonlinear relation between model input and output without a precise mathematical formula [179]. It is somehow similar to the clinical rehabilitation assessment that evaluates subject's performance by a combination of functional indicators [175]. The main motivations of adopting fuzzy techniques for performance evaluation include:

- Fuzzy technique is well-suited to expert system applications where the rules are created from human expert knowledge, such as medical diagnostics [180].
- With customized linguistic rules and mappings, data variations raised by subject-specific and task-specific can be both handled [181].
- Fuzzy logic is essentially a heuristic approach such that previous results of experiments can be used for further updates [182].

Specifically, a FLS consists of three basic elements: the *fuzzifier*, the *rulebase inference* and the *defuzzifier*. The role of fuzzifier is to converse inputs and outputs into membership functions (MFs). The inputs of the designed FLS are above-mentioned three indicators e_{mabs}, $\tau_{h,mabs}$, $\mathrm{PR}_{\%}$ and the output is a comprehensive performance measure, denoted as P_i. Three linguistic variables are defined for the FLS inputs with S (small), M (medium), L (large) and five linguistic variables for the output as VB (very bad), B (bad), N (normal), G (good) and VG (very good). The Gaussian MF is adopted due to the advantage of being smooth and nonzero at all points.

The function of rulebase inference is to obtain the linguistic output from the linguistic input and the established rulebase. The development of fuzzy rules are usually based on expertise or prior data analysis, and further tuned in practice. To establish an input-output mapping, the common fuzzy language is adopted which contains a collection of IF-THEN statements, e.g.,

$$\text{IF } e_{mabs} \text{ is M and } \tau_{h,mabs} \text{ is M and } \mathrm{PR}_{\%} \text{ is M, THEN } P_i \text{ is N.} \tag{8.15}$$

Table 7 lists the fuzzy output obtained by 27 combinations of the three fuzzy sets of inputs and the Mamdani inference method [180] is used, i.e.,

$$\mu_{\mathrm{P}_i} = \sum_{27} \max\{\min\ \mu_{e1}\ \mu_{\tau 1}\ \mu_{\mathrm{PR1}}, \min\ \mu_{e2}\ \mu_{\tau 2}\ \mu_{\mathrm{PR2}},\ \text{etc.}\} \tag{8.16}$$

where μ_{P} is the membership degrees of the output linguistic variable and μ_{e1}, $\mu_{\tau 1}$, μ_{PR1}, etc are corresponded input linguistic variables.

Table 8.1: The fuzzy rulebase.

No.	e_{mabs}	$\tau_{h,mabs}$	$\mathrm{PR}_{\%}$	P_i	No.	e_{mabs}	$\tau_{h,mabs}$	$\mathrm{PR}_{\%}$	P_i
1	S	S	S	VB	15	M	M	B	G
2	S	S	M	VB	16	M	B	S	G
3	S	S	B	B	17	M	B	M	G
4	S	M	S	B	18	M	B	B	VG
5	S	M	M	B	19	B	S	S	VB
6	S	M	B	N	20	B	S	M	N
7	S	B	S	B	21	B	S	B	G
8	S	B	M	G	22	B	M	S	B
9	S	B	B	VG	23	B	M	M	N
10	M	S	S	VB	24	B	M	B	G
11	M	S	M	B	25	B	B	S	G
12	M	S	B	N	26	B	B	M	VG
13	M	M	S	N	27	B	B	B	VG
14	M	M	M	N					

The defuzzifier converts the membership degrees of the output linguistic variable to the exact value, i.e., the comprehensive performance indicator P_i. The centroid of area method is employed in the defuzzification process which provides a smooth output, i.e.,

$$\mathrm{P}_i = df(\mathrm{P}_i) = \frac{\int_a^b \mathrm{P}_i \mu_{\mathrm{P}_i} d\mathrm{P}_i}{\int_a^b \mu_{\mathrm{P}_i} d\mathrm{P}_i} \tag{8.17}$$

where a and b are the lower and upper bounds of the area, respectively.

When designing the FLS, the protocol for selecting defuzzification method can refer to [183]. However, the selection of MFs and the formulation of fuzzy inference rules need to be specified according to system (task) differences. With the baseline controller given in the last Section, a series of prior experiments are conducted to determine the values of MFs. The reference trajectory of the CARR is defined as

$$q_d = \begin{bmatrix} 0.3\sin(2\pi f t) \\ 0 \\ 0 \end{bmatrix} \tag{8.18}$$

where $f = 0.05$ and the time interval is $t = 0.005$. Three sets of K_r are selected to practically acquire the value of three selected indicators, that is

$$\begin{aligned} &1) \text{ Baseline} : K_r = \text{diag}(10, 3) \\ &2) \text{ Robot assistance} : K_r = \text{diag}(20, 3) \\ &3) \text{ Encouraged participant} : K_r = \text{diag}(5, 3). \end{aligned}$$

Total ten repeated trials are conducted with one healthy subject for each set of K_r and $P_c = 1$ is selected. The horizontal view of training interface is presented in Figure 8.1. Subject is asked to track the solid yellow cycle (reference trajectory) with the cyan cycle (current trajectory), while the ultimate target is given by the red cycle. Also, for reminding the direction of movement, the red cycle will become solid and the blue arrow will reserve when the plantarflexion is activated.

Experimental results are presented in Figure 8.2, 8.3 and 8.4, which contains four consecutive trials and provides the information of tracking error, interactive torque and dynamic performance, i.e., reference and measured velocity. Since the trajectory is only defined for D/P movement, the performance along this direction is presented. The numerical variation of the chosen indicators can provide us with the basis of fuzzy inference. It is clear in Figure 8.2 and 8.3, subject's participation is increased under lower stiffness matrix, in return, the tracking error is also increased. Besides, from Figure 8.4, it can be observed that the tendency of the interactive torque becomes

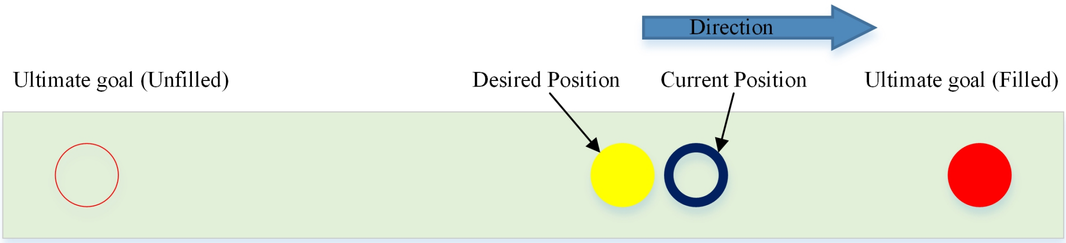

Figure 8.1: Horizontal view of the training interface. The direction towards to the right: dorsiflexion; left: plantarflexion. The ultimate goal will be filled when the movement towards it.

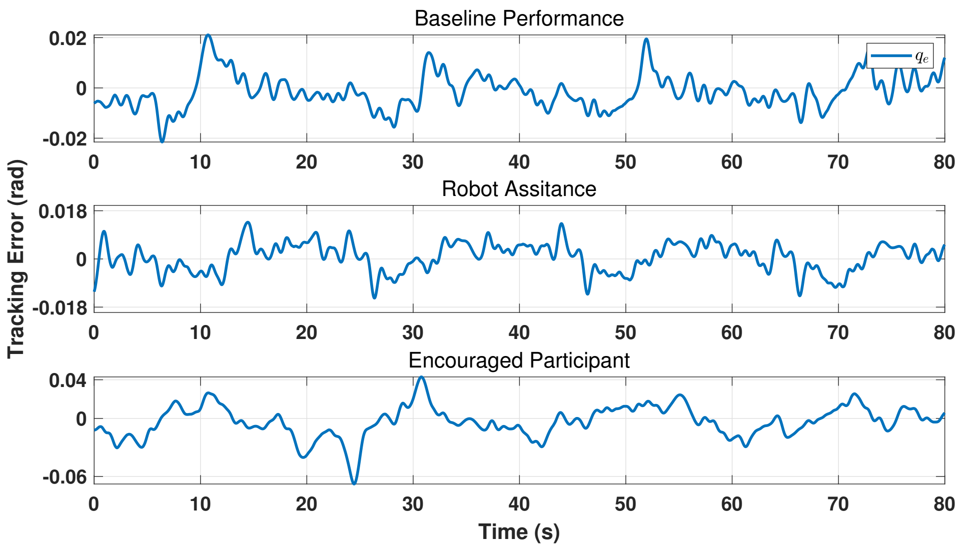

Figure 8.2: Tracking error under different stiffness matrices.

similar to the desired velocity, indicating that the value of $PR_{\%}$ will be increased when the subject is actively conducting the task. The ultimate goal for our rehabilitation strategy is to promote active participant with acceptable tracking error. Therefore, the fuzzy rules given in Table 8.1 is determined upon above discussions. Note that the involvement of $PR_{\%}$ not only reflects the ratio of active participant, but also avoids potential risky situation, e.g., when the passive stiffness of subject's ankle is impeding the reference trajectory.

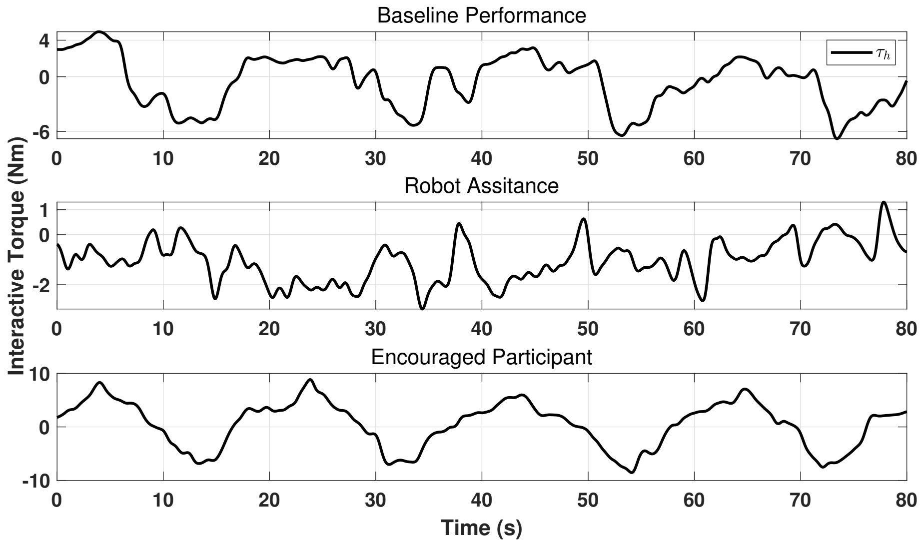

Figure 8.3: Interactive torque under different stiffness matrices.

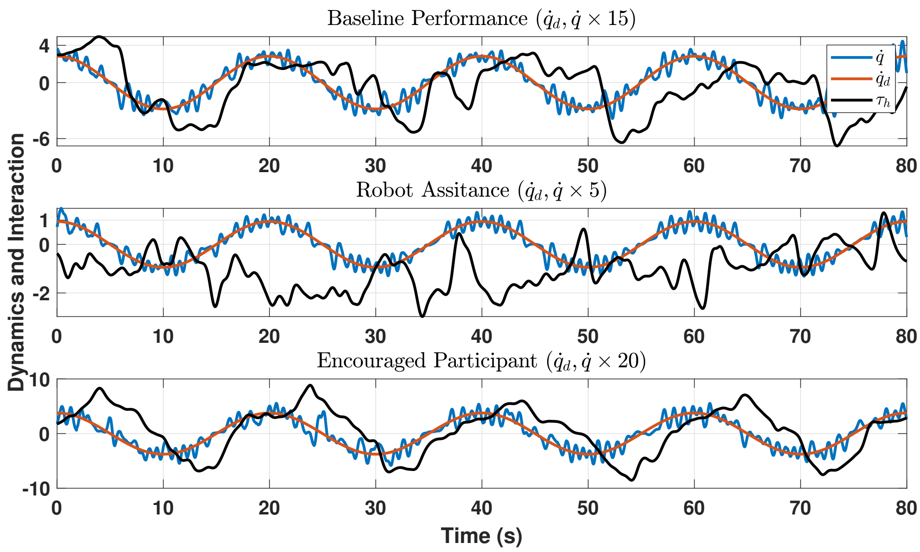

Figure 8.4: Detailed dynamics with different magnification of the CARR velocity.

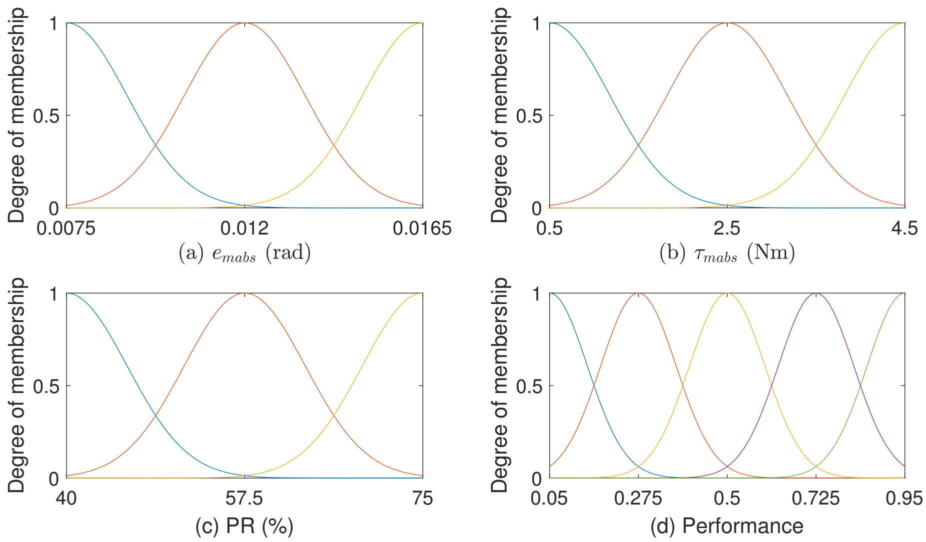

Figure 8.5: Membership functions of the input and output variables. (a) The fuzzy mean absolute error. (b) The fuzzy mean absolute interactive torque. (c) The fuzzy participant ratio. (d) The performance output.

The memberships function is also determined by prior experiments with statistical analysis results in Table 8.3.2. The average values of three indicators in ten trials are calculated that provide a basis of the selection of membership functions. The membership functions are then given by Figure 8.5, where the performance indicator are separated from 0.05 to 0.095 with an interval of 0.225.

Table 8.2: Mean values of three indicators in ten trials.

	e_{mabs} (rad)	$\tau_{h,mabs}$ (Nm)	$PR_{\%}$
Baseline	0.00968	2.6787	60
Robot assistance	0.00856	1.1716	46.95
Encouraged participant	0.0157	3.7468	69.09

8.4 Progressive Learning Controller

8.4.1 Controller design

The performance output of the fuzzy model given in last section provides a comprehensive evaluation of task completion during previous trial. Subsequently, a progressive learning control law is designed based on the objectives given in Section 7.2.1. The control input τ_r is given by

$$\tau_r = -K_r(t)s + M(q)a + C(q,\dot{q})v + G(q) - P_c\tau_h \tag{8.19}$$

where $K_r(t)$ can be time-varying and is adapted by the performance of last trial. $P_c \in (0,1)$ is a scale factor that represents the global assistance of the robot and will be discussed later. To provide more compliant robot motion and promote participant's evolvement, a cost function is first defined for minimizing $K_r(t)$ as

$$J_c(t) \equiv \frac{1}{2}\int_{t-T}^{t} P_i^2 \mathrm{vec}(K_r)^T \mathrm{vec}(K_r) d\sigma \tag{8.20}$$

where $t \in [0,T]$ is the time interval for a single trial which is periodic with T. P_i is the fuzzy performance output, and vec$(\cdot)$ stands for the column vectorization operation. The minimization can be achieved with following update law

$$P_i \Delta K_r(t) \equiv P_i(K_r(t) - K_r(t-T)) = \mathrm{vec}(ss^T) - \frac{\gamma}{1-P_i} P_i K_r(t) \tag{8.21}$$

where $\gamma > 0$ is a forgetting factor of learning. In addition, the trajectory tracking performance can be specified by the minimization of

$$J_e(t) \equiv \frac{1}{2} s(t)^T M(q) s(t) \tag{8.22}$$

Remark 13 *The cost function (8.22) is commonly used in robot controller design that gives the convergence of tracking error. However, under active rehabilitation scenario, a smaller $K_r(t)$ can lead to less robot interventions that promote participant's initiative. For this purpose, adaption law (8.20) is designed for minimizing an extra cost function (8.21).*

Therefore, the overall cost function to minimize is

$$J(t) \equiv J_e(t) + J_c(t) \tag{8.23}$$

In the next section, a Lyapunov-like analysis of the closed-loop learning control and the effect of employing the performance evaluation will be carried out.

8.4.2 Stability and Convergence Analysis

Assume that the time interval for a single trial is T, since the rehabilitation training normally contains several repetitions, the entire training process is periodic with T. By virtue of the repeatability, the participant's performance in last trial can be used to judge whether they are able to contributes more in the current tail. The difference between two consecutive periods of the overall cost (8.23) will be studied, i.e., $\Delta J(t) = J(t) - J(t-T) = \Delta J_e(t) + \Delta J_c(t)$. Let us first analyse $\Delta J_e(t)$. The time derivative of $J_e(t)$ is

$$\dot{J}_e = s^T M(q)\dot{s} + \frac{1}{2}s^T \dot{M}(q)s \tag{8.24}$$

Substituting control law (8.19) into (8.1), the closed-loop dynamic are described by

$$M(q)\dot{s} + C(q,\dot{q})s + K_r s = (1-P_c)\tau_h \tag{8.25}$$

Integrating $\dot{J}_e$ from $t-T$ to t, one can obtain

$$\Delta J_e = \int_{t-T}^{t} -s(\sigma)^T K_r(\sigma)s(\sigma) + (1-P_c)s(\sigma)^T \tau_h d\sigma \tag{8.26}$$

Next, consider the difference between J_c of two consecutive trials

$$\begin{aligned}
\Delta J_c =& J_c(t) - J_c(t-T) \\
=& \frac{1}{2}\int_{t-T}^{t} \Big(P_i^2 \mathrm{vec}(K_r(\sigma))^T \mathrm{vec}(K_r(\sigma)) - P_i^2 \mathrm{vec}(K_r(\sigma-T))^T \mathrm{vec}(K_r(\sigma-T))\Big) d\sigma \\
=& \frac{1}{2}P_i^2 \int_{t-T}^{t} \Delta \mathrm{vec}(K_r(\sigma))^T \Big(\mathrm{vec}(K_r(\sigma)) + \mathrm{vec}(K_r(\sigma-T))\Big) d\sigma \\
=& \frac{1}{2}P_i^2 \int_{t-T}^{t} \Delta \mathrm{vec}(K_r(\sigma))^T \Big(2\mathrm{vec}(K_r(\sigma)) - \mathrm{vec}(K_r(\sigma)) + \mathrm{vec}(K_r(\sigma-T))\Big) d\sigma
\end{aligned}$$

$$=-\frac{1}{2}P_i^2\int_{t-T}^{t}\Delta\text{vec}(K_r(\sigma))^T\Delta\text{vec}(K_r(\sigma))d\sigma+P_i^2\int_{t-T}^{t}\Delta\text{vec}(K_r(\sigma))^T\text{vec}(K_r(\sigma))d\sigma \tag{8.27}$$

Substituting learning law (8.21) into the second term of (8.27), one has

$$\begin{aligned}&P_i^2\int_{t-T}^{t}\Delta\text{vec}(K_r(\sigma))^T\text{vec}(K_r(\sigma))d\sigma\\ =&P_i\int_{t-T}^{t}\text{vec}(s(\sigma)s(\sigma)^T)^T\text{vec}(K_r(\sigma))d\sigma-P_i^2\int_{t-T}^{t}\frac{\gamma}{1-P_i}\text{vec}(K_r(\sigma))^T\text{vec}(K_r(\sigma))d\sigma\end{aligned} \tag{8.28}$$

Employing the property $\text{vec}(aa^T)^T\text{vec}(b)=a^Tba$ for vector $a\in\mathbb{R}^{\ell\times 1}$ and matrix $b\in\mathbb{R}^{\ell\times\ell}$, (8.28) becomes

$$P_i\int_{t-T}^{t}s(\sigma)^TK_r(\sigma)s(\sigma)d\sigma-P_i^2\int_{t-T}^{t}\frac{\gamma}{1-P_i}\text{vec}(K_r(\sigma))^T\text{vec}(K_r(\sigma))d\sigma \tag{8.29}$$

Substituting (8.26) and (8.27) into (8.23) and considering (8.29), it yields

$$\begin{aligned}\Delta J=&\Delta J_e+\Delta J_c\\ =&\int_{t-T}^{t}-s(\sigma)^TK_r(\sigma)s(\sigma)+P_is(\sigma)^TK_r(\sigma)s(\sigma)+(1-P_c)s(\sigma)^T\tau_h\\ &-\frac{P_i^2\gamma}{1-P_i}\text{vec}(K_r(\sigma))^T\text{vec}(K_r(\sigma))d\sigma-\frac{1}{2}P_i^2\int_{t-T}^{t}\Delta\text{vec}(K_r(\sigma))^T\Delta\text{vec}(K_r(\sigma))d\sigma\\ =&-\int_{t-T}^{t}(1-P_i)s(\sigma)^TK_r(\sigma)s(\sigma)+\frac{P_i^2\gamma}{1-P_i}\text{vec}(K_r(\sigma))^T\text{vec}(K_r(\sigma))\\ &-(1-P_c)s(\sigma)^T\tau_hd\sigma-\frac{1}{2}P_i^2\int_{t-T}^{t}\Delta\text{vec}(K_r(\sigma))^T\Delta\text{vec}(K_r(\sigma))d\sigma\end{aligned} \tag{8.30}$$

Note that the term $-\frac{1}{2}P_i^2\int_{t-T}^{t}\Delta\text{vec}(K_r(\sigma))^T\Delta\text{vec}(K_r(\sigma))d\sigma$ is left since it is negative definite. According to (8.30), a sufficient condition for $\Delta J\leq 0$ is

$$\begin{aligned}&(1-P_i)s^TK_rs+\frac{P_i^2\gamma}{1-P_i}\text{vec}(K_r)^T\text{vec}(K_r)-(1-P_c)s^T\tau_h\\ \geq&(1-P_i)\lambda_{min}(K_r)\|s\|^2+\frac{P_i^2\gamma}{1-P_i}\|\text{vec}(K_r)\|^2-(1-P_c)\|s\|\|\tau_h\|\geq 0\end{aligned} \tag{8.31}$$

where $\|\cdot\|$ denotes the Euclidean vector norm and induced matrix norm. $\lambda_{min}(K_r)$ stands for the minimal eigenvalue as in (8.6). The rehabilitation environment with intensive interaction implies that $\|\tau_h\|\neq 0$. Moreover, following the definition of fuzzy performance evaluation result and global assistance factor, i.e., $P_i \in (0.05, 0.95)$ and $P_c \in (0, 1)$, one has,

$$\begin{aligned} &4(1-P_i)^2\lambda_{min}^2(K_r)\|s\|^2 + 4\gamma\lambda_{min}(K_r)P_i^2\|\text{vec}(K_r)\|^2 \\ &-4(1-P_i)\lambda_{min}(K_r)(1-P_c)\|s\|\|\tau_h\| \geq 0 \end{aligned} \tag{8.32}$$

Adding $(1-P_c)^2\|\tau_h\|^2$ to the both sides of inequality (8.32) gives

$$\begin{aligned} &4(1-P_i)^2\lambda_{min}^2(K_r)\|s\|^2 + 4\gamma\lambda_{min}(K_r)P_i^2\|\text{vec}(K_r)\|^2 \\ &-4(1-P_i)\lambda_{min}(K_r)(1-P_c)\|s\|\|\tau_h\| + (1-P_c)^2\|\tau_h\|^2 \geq (1-P_c)^2\|\tau_h\|^2 \end{aligned} \tag{8.33}$$

Due to the fact that $4(1-P_i)^2\lambda_{min}^2(K_r)\|s\|^2 - 4(1-P_i)\lambda_{min}(K_r)(1-P_c)\|s\|\|\tau_h\| + (1-P_c)^2\|\tau_h\|^2 = 4(1-P_i)^2\lambda_{min}(K_r)^2\big(\|s\| - \frac{1-P_c}{2(1-P_i)\lambda_{min}(K_r)}\|\tau_h\|\big)^2$, inequality (8.33) can be written as

$$\begin{aligned} &4(1-P_i)^2\lambda_{min}(K_r)^2\big(\|s\| - \frac{1-P_c}{2(1-P_i)\lambda_{min}(K_r)}\|\tau_h\|\big)^2 + 4\gamma\lambda_{min}(K_r)P_i^2\|\text{vec}(K_r)\|^2 \\ &\geq (1-P_c)^2\|\tau_h\|^2 \end{aligned} \tag{8.34}$$

where the left hand side of (8.34) is positive semi-definite. Based on the uniformly ultimately bounded stability theory [55], it follows that $\|s\|$ and $\|\text{vec}(K_r)\|$ will converge to an invariant set $\Omega_s \subseteq \Omega$ on which $\Delta J = 0$, where the bounding set Ω is defined as

$$\begin{aligned} \Omega = \Bigg\{ &(\|s\|, \|\text{vec}(K_r)\|), \ \frac{4(1-P_i)^2\lambda_{min}(K_r)^2\big(\|s\| - \frac{1-P_c}{2(1-P_i)\lambda_{min}(K_r)}\|\tau_h\|\big)^2}{(1-P_c)^2\|\tau_h\|^2} \\ &+ \frac{4\gamma\lambda_{min}(K_r)P_i^2\|\text{vec}(K_r)\|^2}{(1-P_c)^2\|\tau_h\|^2} \leq 1 \Bigg\} \end{aligned} \tag{8.35}$$

It is clearly that follows (8.35), the bounding set Ω can be represented as an ellipse in the first quadrant

$$\frac{(x-p)^2}{a^2} + \frac{(y-q)^2}{b^2} = 1, \ x \geq 0, \ y \geq 0 \tag{8.36}$$

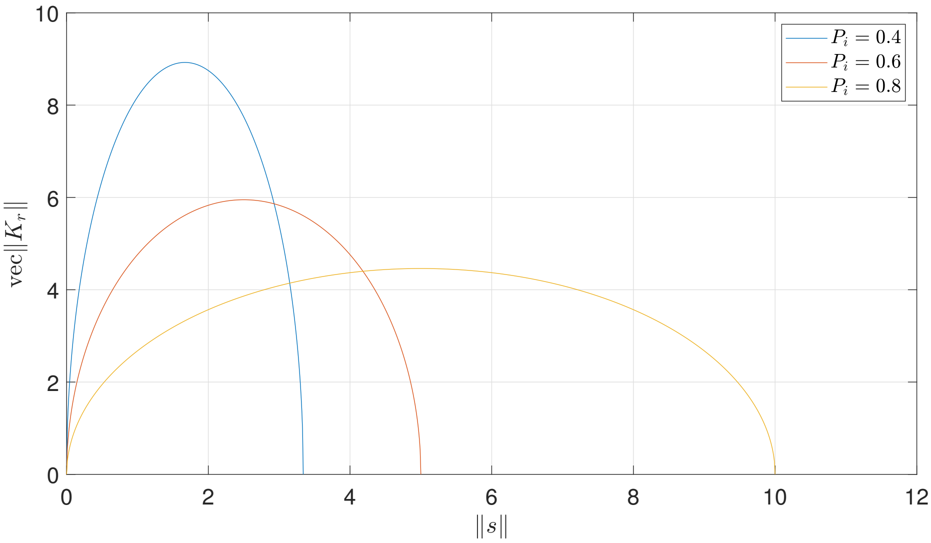

Figure 8.6: Curve of the bounding set under different P_i.

where

$$
\begin{aligned}
& x = \|s\|,\ y = \|\text{vec}(K_r)\| \\
& p = \frac{(1-P_c)\|\tau_h\|}{2(1-P_i)},\ q = 0 \\
& a = \frac{(1-P_c)\|\tau_h\|}{2(1-P_i)\lambda_{min}(K_r)},\ b = \frac{(1-P_c)\|\tau_h\|}{2\sqrt{\gamma}P_i}
\end{aligned} \tag{8.37}
$$

The upper bound for x and y are $a+p$ and $b+q$, respectively. From (8.37), a large P_i which indicates that participant has a good performance in last trial will lead to a large $a+p$. Meanwhile, the value of b will be decreased which represents that the stiffness of robot joint will be reduced. Therefore, under the proposed progressive learning law, the previous performance allows the modification of the tracking error and stiffness matrix bounds, i.e., good performance leads to a large error bound and lower stiffness matrix which stimulate subject's engagement, vice versa. Figure 8.6 presents the change of bounding set (8.35) caused by different P_i.

Note that the term $(1-P_c)\|\tau_h\|$ also affects the bounding set Ω. There are two main reasons to incorporate the assistance factor P_c:

- To reduce the conflicts between human and robot movements.

- Providing appropriate challenge for promoting subjects' active contribution.

From (8.37), increasing P_c will lead to a smaller $a + p$ and $b + q$ that is benefit to the rehabilitation training. Meanwhile, from (8.35) and (8.37), it can be seen that the forgetting factor γ is related to the ultimate bound of K_r. A large γ will lead to a "compliant" robot motion, in return, the learning transient behaviour of K_r could be degraded. In virtue of the performance evaluation, the value of γ is determined as follows:

- If subject had a poor performance ($P_i < 0.5$), a small γ should be selected that leads to a minor change of K_r in current trial.
- If subject had a good performance ($P_i \geq 0.5$), γ is increased for making the robot more "compliant".

Similar to [165, 172], the controller will treat the subjects' effect as "inappropriate" under poor performance evaluation result while more trials are reproduced with small difference of K_r such that subjects can further learn an appropriate ankle configuration. On the contrary, with good performance, subjects have a "reliable" movement which leads to a quick adaption of K_r.

Remark 14 *From a rehabilitation point of view, the progressive learning controller fits the fields of "active ROM training" and "strength training" scenarios. Under these modes, subjects' ankle has significant small resistance from spasticity while selective control of ankle movement can be obtained* [184]. *The value of open parameters can be specified by different training requirement, e.g., one can increase the initial value K_0 and γ if task completeness is the primary goal; a smaller P_c also leads to additional reduction of K_r that can be further defined when subject reaches a certain amount of participant.*

Remark 15 *From the construction of progressive learning law* (8.21) *which aims to minimize the cost function* (8.21). *The controller maintains a decreasing tendency of stiffness matrix such that subjects have to use their own effect to complete the reference* *trajectory. It has been validated in [163], such design is able to promote subjects' participant. However, authors in [163] use an increment algorithm for subject's capability estimation via real-time torque sensing data. In other words, a single indicator, i.e., interactive torque is used to adapt the robot assistance level. In the subsequent experimental validation, the effects of using single indicator and designed fuzzy logic system are specified.*

8.5 Experiments and Results

A series of experiments are conducted to validate the performance of the progressive learning strategies. The same trajectory (8.18) in baseline controller test is used and the training interface is shown in Figure 8.1. During experiments, subjects are informed with their qualitative performance for three indicators, i.e., whether the evaluations of three indicators surpass their medians ($P_i > 0.5$). The initial stiffness matrix is set as $K_0 = \text{diag}(15, 3)$ and the performance output of the fuzzy system are initialized by $P_1 = 0.12018$. The weight between position and velocity error is set as $\Lambda = 3$. During the first trial, subjects are asked to relax and familiarize themselves with the task characteristics. The weight between robot assistance and active participant is set as $P_c = 0.5$. Follow the discussion of forgetting factor γ in the last section, the following piecewise functions are designed

$$\gamma = \begin{cases} 0.01 & \text{if } P_i < 0.5 \\ 0.1 & \text{if } P_i \geq 0.5 \end{cases} \tag{8.38}$$

Total number of trials is set to about ten, depending on the performance of each subject. Since the progressive learning law maintains a tendency of decreasing robot assistance, the training will be stopped in advance if subject consistently perform well in the previous three tasks. Otherwise, few more trials are encouraged for subject to actively contribute to the movement. Ten healthy volunteers (two females and eight males) with no history of physical or neurological injury to the ankle are involved in the experiments. They are able to actively control their ankle and understand the contents of experiments. During experiments, subjects (hereinafter referred to as S1-S10) can only see the training interface and the researcher is monitoring the fuzzy performance evaluation results in backstage. All experiments have been approved by the University of Leeds Research Ethics Committee (reference MEEC 18-001). According to (8.18), the maximum amplitude of the selected movement is around 0.3 rad which is within the normal ROM of the ankle. The training period for one trial is 20 s and the overall angular velocity of CARR during operation is under 20 mrad/s that largely mimic clinical environment.

8.5.1 Performance Evaluation via Fuzzy Logic

The fuzzy logic designed for performance evaluation is validated first, where the statistical results are summarized in Figure 8.7. The maximum and minimum values of e_{mabs} is given in Figure 8.7(a) which range from $[0.00803, 0.0177]$ rad. It is similar to the predefined fuzzy membership function ($[0.0075, 0.0165]$). Identically, as shown in Figure 8.7(b) and (c), other two indicators for ten subjects over ten trials are range from $\tau_{h,mabs} \in [1.48, 4.6]$ Nm and $\mathrm{RP}_{\%} \in [43.73, 80.55]$ %. Compared to its corresponded membership functions, only one abnormal value has been found in Figure 8.7(b). It indicates that the designs of membership function which depend on primary experimental results can well define the range of selected performance indicators. The output of the fuzzy evaluation system is presented in Figure 8.7(d). Although the quantitative ranges of different indicators are well estimated by primary experiments. The shadow area infers the standard error (SE) between different subjects' mean performance over trials. It indicates that individual differences are commonly existed along the task horizon. Detailed performance output is given in Figure 8.8, the total trials have been done for different subjects are: 11 trials for S2 and S4; 10 trials for S3, S5 and S6; 9 trials for S1 and S7-S9; 7 trials for S10. It can be seen that the learning process of different subject is distinctive, especially in the middle of training. Since the reduction of K_r requires continuous contribution by subject's own effects, a slight lack of concentration are likely result in a degraded performance [163]. In terms of the usage of

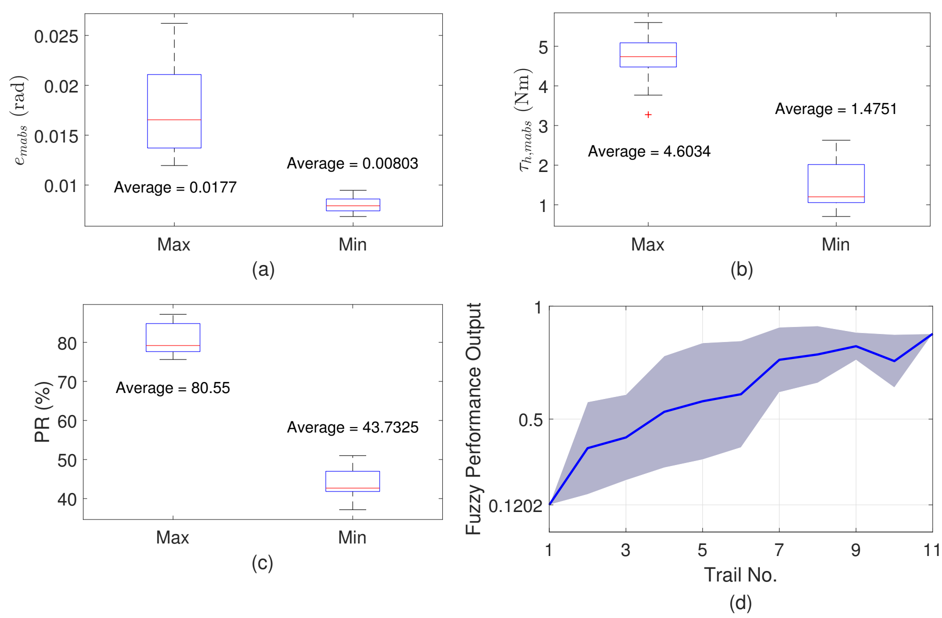

Figure 8.7: The statistical results of the fuzzy performance evaluation. (a) e_{mabs}; (b) $\tau_{h,mabs}$; (c) PR; (d) Performance output where blue line represents the mean of the fuzzy output and the gray shadow indicates the SE.

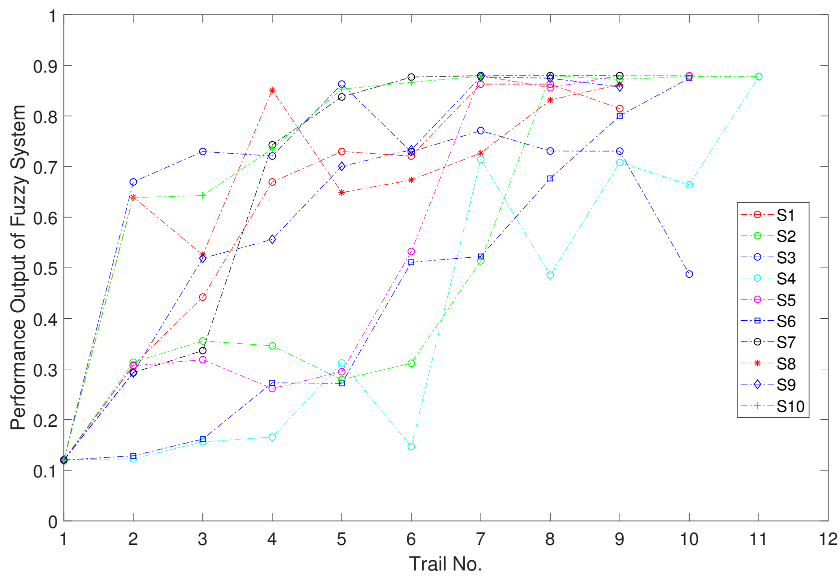

Figure 8.8: Fuzzy performance evaluation results over ten subjects.

Table 8.3: Mismatching of using single indicator for performance evaluation.

	S1	S2	S3	S4	S5	S6	S7	S8	S9	S10
e_{mabs}	0.009	0.013	0.013	0.014	0.011	0.013	0.013	0.013	0.0115	0.012
$\tau_{h,mabs}$	2.37	4.06	2.13	2.07	0.96	2.99	3.24	2.92	2.63	2.27

single indicator for performance evaluation, authors in [54] and [163] adopt tracking error and interactive torque, respectively. A set-point is used for determine the robot assistance which is selected as the median of the chosen indicators. In Table 8.5.1, the median value of membership functions are used for e_{mabs} and $\tau_{h,mabs}$ as the set-point. The experimental results of each indicator when the other one reaches the set-point are recorded. The mismatch between two indicators (one reaches the set-point but another not) is marked with a purple background. It can be observed that mismatches between different indicators are common, which can yield unsuitable judgement of the robot-assisted level.

8.5.2 Validation of Progressive Learning Algorithm

Next, the progressive learning controller is evaluated in terms of the modified error bounds and learned stiffness matrices K_r. In Figure 8.9 and 8.10, the effects of performance P_i on the error bound and K_r are validated. As analyses upon ultimate bound (8.35) and equation (8.37), the increment of P_i leads to a large error bound and a smaller stiffness matrix. The progressive increase of P_i can be validated in Figure 8.7 and 8.8, while in Figure 8.9 and 8.10, $\|s\|$ and $\|K_r\|$ have increasing and decreasing tendency, respectively. Since the initial sets of K_r are subject-invariant and relax movement is suggested in first trial. It can be seen that, under superior robot assistance, the trajectory of movement is stable with SE=0.0942. Subsequently, better performance leads to an increase of error bound that let subjects dominate the training with a highest SE=0.4017 (during the 8^{th} trial). On the contrary, in Figure 8.10, the $\|K_r\|$ maintains a decreasing tendency for providing a "compliant" robot motion. The same

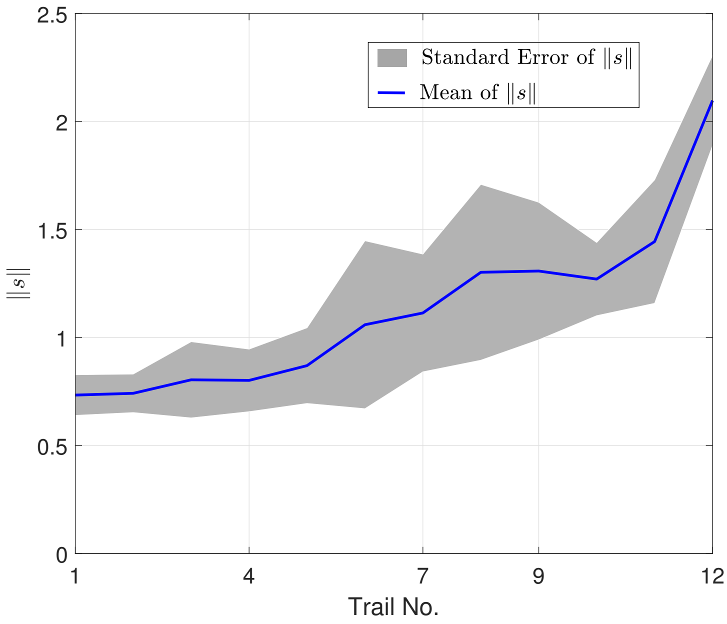

Figure 8.9: Mean of $\|s\|$ (blue line) and SE (gray shadow) of ten subjects over trials.

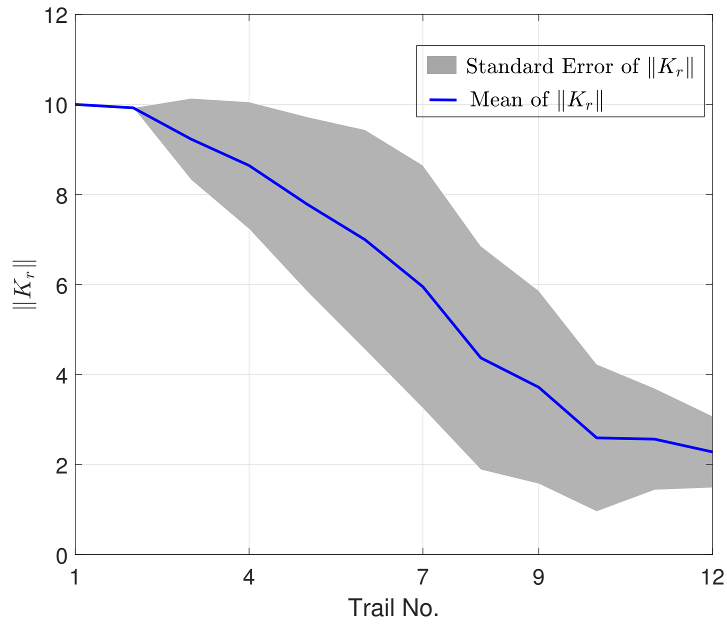

Figure 8.10: Mean of $\|K_r\|$ (blue line) and SE (gray shadow) of ten subjects over trials.

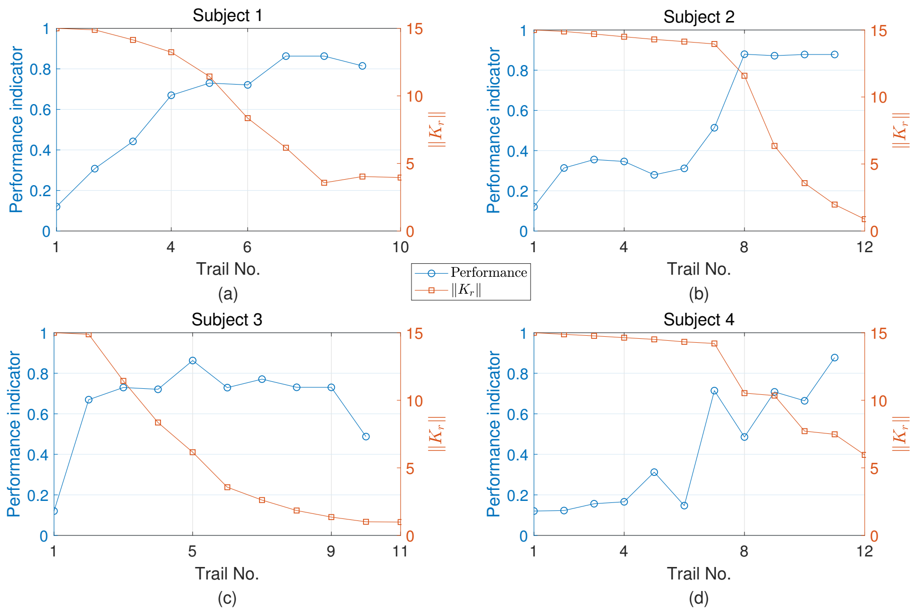

Figure 8.11: Performance output of fuzzy evaluation and $\|K_r\|$ vs trials.

property can be found during first trial since P_i is initialized and the SE=0.0032. Due to the progress of individual learning, the learned K_r is dispersed among subjects with a maximum SE=2.7025.

As discussed in Section 7.4.2, the forgetting factor γ plays a vital role in the learning of K_r. To validate the piecewise function defined in (8.38), the detailed progressive learning process of K_r is presented in Figure 8.12 which contains S1 to S4. Note that the initial trial is also included which means the updating of K_r is a step ahead the performance indicator P_i. It is clear that S2 and S4 ((b) and (d)) show a slow performance improvement in the early stage of training. To help them further familiarize the training contents, the controller will maintain a small change of K_r that keep the robot assistant at a certain amount. Both of them achieve a satisfactory performance ($P_i > 0.5$) during 7^{th} trial, the learning ratio has a significant increment that speeds up the reduction of K_r. Relatively speaking, S1 and S3 are two quick learner that able to achieve a satisfactory performance within four and two trials, respectively. Relatively speaking, S1 and S3 are two quick learner that able to achieve a satisfactory

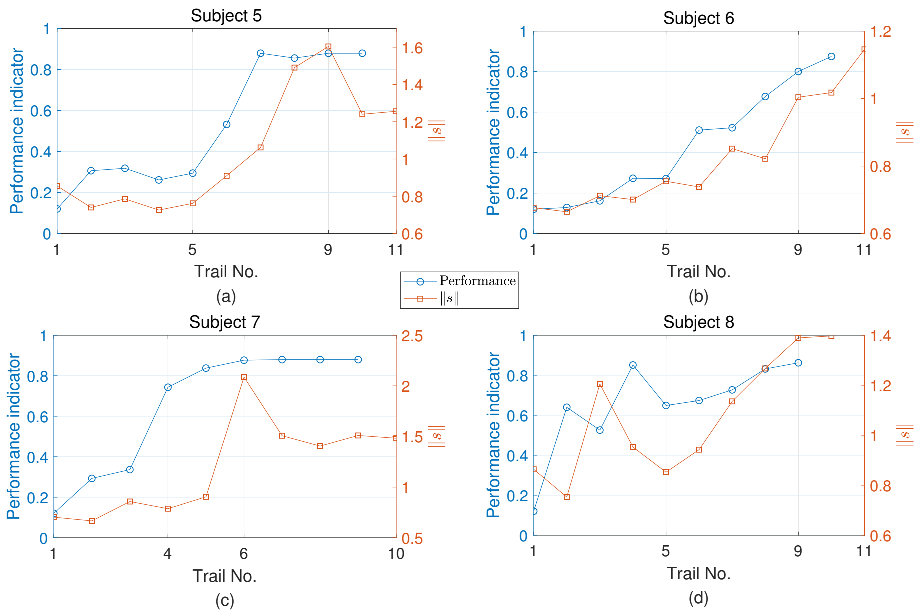

Figure 8.12: Performance output of fuzzy evaluation and $\|s\|$ vs trials.

performance within four and two trials, respectively. To keep them actively engage the training, the K_r is declined rapidly while less robot assistance is provided. Note that the piecewise function is continuously active, if subjects are enable to keep their performance, they also have opportunity to "retry" the task with almost unchanged K_r, e.g. 9^{th} trial for S4. In addition, the learning process of $\|s\|$ is also given in Figure 8.11 which contains S5 to S8. Similarly, individual differences are obvious in terms of error bound variation. The increase and decrease of the error bound is clearly verified in Figure 8.11(b) and (d). Moreover, for S5 and S7, subjects both maintain a comparative good performance ($P_i > 0.83$) from 7^{th} trial and the T_h for each subject is [5.35,5.62,4.93] and [5.67,5.55,5.32], respectively. With rather similar T_h, the change of K_r is small according to (8.37) while the weight control becomes the minimization of (8.22), i.e., minimizing the sliding error s.

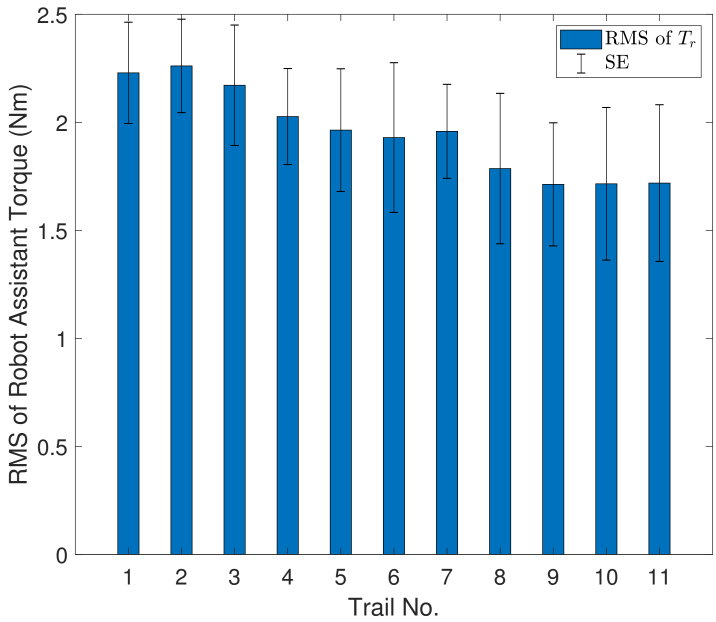

Figure 8.13: RMS and SE of robot assistant torque vs trials.

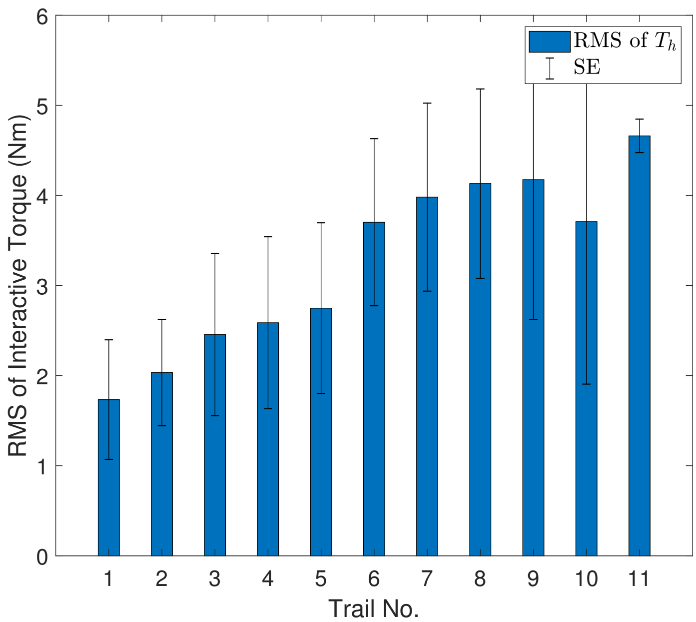

Figure 8.14: RMS and SE of T_h vs trials.

8.5.3 Robot Assistance and Interactive torque

To show the dynamic interaction between the CARR and subjects, Figure 8.13 and 8.14 demonstrate the RMS and SE of robot assistant torque and interactive torque over the entire training. It can be seen that the robot assistant torque has an obvious decreasing tendency, which is reduced by 22.89 % (from 2.229 Nm to 1.719 Nm). Correspondingly, the interactive torque is increased for achieving the given task which is increased by 62.82 % (from 1.733 Nm to 4.661 Nm). Results illustrate that the progressive learning controller can reduce the amount of robot assistance based on the subjects' performance. As long as the given task within the capabilities of subjects, they are promoted to actively contribute to the training. So far, the main properties of the designed controller have been tested and its ability of promoting participation is validated. Next, the individual training performance of S10 is presented, the CARR actually perform 10 trials while only 7 trials are recorded in the above statistical analysis. Two more trials without interaction are recorded and the control performances are given in Figure 8.15. It can be seen in Figure 8.8, S10 achieves satisfactory performance within two trials and the K_r maintains a fast deceleration. The tracking performance and interactive information are given in Figure 8.15(a) and (b). It can be observed that instability happens at 8^{th} trial and the research ask S10 to stop interaction for her safety concerns. Two trials (red block) are specified in Figure 8.15(c) and (d), while the tracking error is evidently large and $T_h \approx 0$. Due to the decrease of K_r, the error compensation of the CARR is limited while external torque (human provided) is expected for completing the task. From Figure 8.15(e) and (f), the decrease of interactive torque during last two trials are shown. As expected, the robot assistance is still increased which results in a poor tracking performance. Without active interaction, the highest performance output will not exceed "N" according to constructed fuzzy rules (Table 8.1). Therefore, due to the design of γ, the CARR keep same motion during these two trials. On the other hand, the sudden removal of interaction also indicates that the stability of the proposed progressive learning controller.

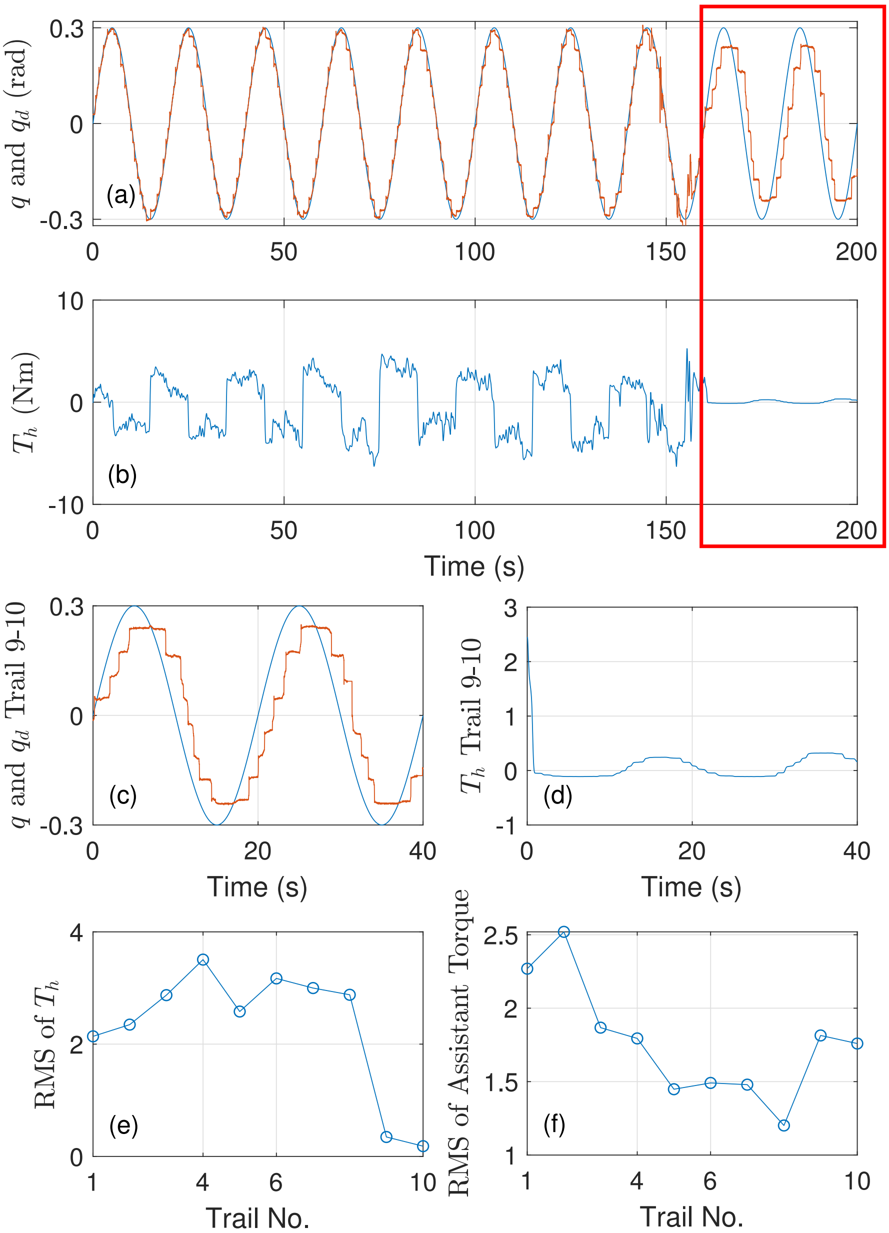

Figure 8.15: Test trial with suddenly stopped interaction. (a) Desired trajectory q_d and actual trajectory q; (b) T_h over entire training; (c) q_d and q without interaction; (d) T_h without interaction; (e) RMS of T_h vs trials; (f) RMS os robot assistant torque vs trials.

8.6 Conclusion

This chapter proposes a progressive learning framework with fuzzy logic based performance evaluation and an ILC-based scheme. The baseline controller is first given and error bound modification concept is introduced. To quantitatively evaluate the training performance, three indicators that include kinematic and dynamic information are selected and primary experiments are conducted for constructing the fuzzy system. The performance output of the fuzzy logic is used to iteratively update the stiffness matrix of the robot controller. A cost function is designed to be minimized and the ultimate bounds of the controller are given by Lyapunov theory. Experiments with ten healthy subjects validate the efficacy of the proposed scheme. The individual difference can be specified during training and active participants are promoted by 62.86 %.

8.7 Chapter Summary

As another important content in rehabilitation, promoting participation is considered in this chapter for reinforcing the outcome of the fourth objective. The clinical scoring mechanism is converted into a fuzzy logic for performance evaluation and the robot assistances are designed to be gradually decrease during training. The experiments verify the feasibility of the designed framework, while more participants are suggested for comprehensive validation.

Chapter 9

Conclusion and Future Work

This chapter summarizes the main outcomes and contributions of studies presented in this thesis. A series of ILC strategies are developed for robot-aided ankle rehabilitation and validated on the CARR prototype. In particular, the data-driven adaptive ILC and the constrained robust ILC are proposed for improving the tracking accuracy, control robustness and training safety during ROM exercises, while iterative impedance learning and performance-based progressive learning strategies are developed for enhanced ankle strength training. Moreover, this chapter inspects the shortcomings of current works and provides potential improvements for further study.

9.1 Outcomes and Contributions

This thesis begins with an introductory chapter that provides readers with an overview of the significance of this research and the outline. To effectively incorporate robotic devices with ankle rehabilitation, proper robot construction and advanced control strategies are essential. To better understand how robot controllers adapt to the ankle training during different periods of recovery, control strategies with "adaption" or "learning" concepts for both ankle passive and active training are reviewed in Chapter 2. In virtue of the repetitive nature of training, ILC shows great potential in ankle rehabilitation and unsolved research gaps are summarized.

Table 9.1: Summarised outcomes and contributions of this research.

No.		Outcomes and Contributions
1	Robot development	CARR for isolated and three-dimensional ankle treatment with position and interactive feedback
2	Trajectory tracking	Nonlinearity, modelling difficulty Data-driven model + Adaptive ILC
3		Uncertainties, state constraints Robust feedback + Barrier function based ILC
4	HRI training	Unknown human model, complaint interaction Iterative impedance learning + Torque control
5		Personalized training evaluation, encourage participant Fuzzy performance evaluation + Progressive learning

The first outcome, in constructing the CARR prototype is presented in Chapter 3. As a parallel mechanism, the CARR aligns the rotation centre of the robot with the ankle via an actuated-from-above layout that avoids lower limb collaborations during training. Compliant and three DoFs ankle treatments can be delivered with position and interactive feedback. However, the applied PM actuators bring additional burdens on controller design. For subsequent control designs, the detailed derivations of the CARR kinematics and dynamics are also given. To address the modelling difficulty of PM, the second outcome, presented in Chapter 4, is the design of a data-driven adaptive ILC to achieve precise ROMs training of the CARR. Since PM uncertainties and operational safety are not considered, to realize PM dynamics, Chapter 5 introduces, identifies and validates a phenomenological PM model with a three-element form. The third outcome in Chapter 6 develops a robust constrained ILC based on the established PM model in Chapter 5, PM state constraints, parametric and nonparametric uncertainties are conjointly considered. The fourth major outcome is the implementation of ILC based active training strategies on the CARR. In Chapter 6, the iterative impedance learning algorithm is introduced to deal with the unknown ankle dynamics for an enhanced interaction performance. Meanwhile, a force distribution algorithm is introduced for maintaining the PM in tension. However, it is still difficult to determine a unified interactive profile due to individual differences. Therefore, an online fuzzy performance evaluation block is developed with multiple training indicators in Chapter 7. The stiffness of the CARR is progressively updated by previous trial performance and active participants are encouraged via error bound modification technique. To make the major outcomes and contributions of this research clear, Table 9.1 is presented and details are provided in the following subsections.

9.1.1 Compliant Ankle Rehabilitation Robot

The first contribution is the development of a compliant ankle rehabilitation robot. For conducting isolated ankle training, the CARR is an appropriate construction that can deliver three-dimensional ankle movements without the lower extremity coordination. Meanwhile, kinematic and dynamic measures are both implemented that support the robot controller design under passive and active ankle training phases.

Existing parallel mechanisms for ankle rehabilitation [1, 5, 185] have misaligned rotation centre with the patient ankle that requires synergetic lower limb movement. The CARR utilizes an actuated-from-above layout that enables the patient to fully relax their shank during training. Similar designs have been proposed in the previous works of our group by Tsoi [186] and Jamwal [44]. However, electrical motors are employed in [186] which make the robot motion nonbackdrivable and rigid. Moreover, the robot adopts a vertical construction without shank support such that a standing posture is required during training. To resolve these issues, PMs are adopted in [44] and adjustable robot posture is designed. Nevertheless, the interaction force measure is obtained by a single-axis load cell placed in series with each PM. Due to the PM length variation during training, the uncertain decomposition of forces affects the measurement accuracy. The CARR inherits its advantages and upgrades the interactive measure with a six-axis load cell that is mounted between the moving platform and end-effector. Since the origin of the sensor and ankle are close, accurate measurements can be obtained by coordinate transformation. As a suitable robot construction for ankle rehabilitation, the CARR will also be used to validate the following ILC-based control strategies.

9.1.2 Data-Driven Adaptive Iterative Learning Control

The second contribution is to propose a data-driven ILC scheme for enhancing the trajectory tracking performance during ankle ROMs training. The performance degradation is tackled by designing adaptive control law and transient learning behaviour is guaranteed via monotonic error convergence.

Motor-driven ankle robots [1, 31, 61] normally use PD/PID controllers for trajectory tracking. However, the CARR utilizes PMs with nonlinear behaviour such that PD/PID have limited performance [36, 82]. Taking full advantage of the repetitive nature of rehabilitation tasks, two typical attempts include the iterative fuzzy controller in [34] and the IFT scheme in [35]. However, the iterative fuzzy controller uses a rule-based fuzzy logic that usually suffers from formulation difficulty and long processing time, and the performance of IFT is also limited by its PID-based nature. In terms of ILC-based schemes, existing results can be found in two motor-driven ARRs [56, 75]. However, these ILC schemes use a fixed control structure that causes performance degradation in the later period of learning. Moreover, only asymptotic error convergence can be achieved that results in poor transient learning behaviour. To address these issues, the data-driven CFDL model is first introduced to represent the PM dynamics without omitting any high-order terms. Adaptive ILC laws are then designed and an estimation algorithm is constructed for iteratively updating the PM pressure input. Rigorous mathematical proof is given to guarantee the convergence and the boundedness of the algorithm. Experimental studies on the CARR first test the tracking performance without human participants for different ROMs and DOFs, and two therapist-resembled movements are then selected with ten human participants. The PID controller is set as a baseline and conventional P-ILC is also implemented for comparison, results illustrate that the proposed DDAILC has significant improvement on the tracking performance which the maximum tracking error is 9% of the desired trajectory. Meanwhile, the observation of degraded performance for P-ILC has been avoided by constructing adaptive learning law.

9.1.3 Robust Constrained Iterative Learning Control

The third contribution is to propose a robust constrained ILC for the safe state tracking of PM. Unknown parameters and unmodelled uncertainties are tackled with robust control design and predefined state constraints are satisfied by incorporating the BLF approach.

In PM controller design, parametric and nonparametric uncertainties have been separately studied for improving its tracking accuracy [95, 96, 124]. For handling both uncertainties, NDOs are incorporated with dynamic surface control [97] and proxy-based sliding mode control [98]. However, in these controllers, nonparametric uncertainties are assumed to be bounded by some known values which are hard to justify. Besides, the state constraints of the PM that regard the training safety of the CARR is rarely considered in the controller design. To address these issues, parametric uncertainties are specified to pressure-dependent spring and damping coefficients in virtue of the three-element model established in Chapter 5. By introducing the CEF framework, perturbations raised nonparametric uncertainties under LLC conditions and parametric uncertainties can be gradually eliminated via ILC laws and the additional robust control term. Besides, to guarantee PM states are within the predefined bounds, BLF is incorporated with CEF that solves state constraints by restricting corresponding state errors. With proper error bounds selection, uniform convergence of state tracking errors are guaranteed and state constraints will not be violated over the entire learning cycle. Experimental validations on a PM platform indicate that the proposed scheme can effectively avoid violation of state constraint and the maximum error after convergence is 2.5% of the reference trajectory. Subsequently, the proposed RCILC is implemented on the CARR with a predefined ROM constraint. The comparisons with PD-ILC indicate that RCILC can effectively restrict the robot movement and the tracking performance is enhanced by 18%.

9.1.4 Iterative Impedance Learning Control

The fourth contribution is to propose ILC-based strategies for conducting active ankle training while optimizing interaction performance is first considered. An iterative impedance learning scheme is proposed with a force distribution algorithm. Task completion and interaction performance are jointly considered to be minimized and distributed torque control is designed to continuously tense the PM.

Impedance control has been widely applied in AARs for conducting active ankle training [1, 7, 36, 43, 46, 82]. To achieve different interaction performances, single or multiple sets of impedance parameters are designed in [1, 7, 46, 82]. However, it has been reported that the human ankle is dynamically configuring its impedance during locomotion or conducting tasks [45]. Therefore, such adaptation brings difficulty for using fixed impedance parameters to guarantee consistent interaction performance. Variable impedance [43] and admittance control [36] are proposed via tracking error adaption and computational ankle passive torque. Nevertheless, task completion and joint torque are separately considered which may degrade the overall effectiveness of ankle training [40]. Therefore, an impedance learning scheme is introduced that iteratively learn an optimal set of time-varying impedance parameters by minimizing both tracking error and interaction torque. Incorporating force distribution with model-based torque control, the desired interaction performance can be achieved and PMs are guaranteed to be continuously in tension. Compared to the conventional impedance control scheme, experimental validations indicate that the tracking error can be reduced by 0.02 rad which is 8% of the reference trajectory and the compliant interaction performance is retained in the presence of passive ankle stiffness.

9.1.5 Progressive Learning with Fuzzy Performance Evaluation

In addition to the compliance of training, promoted engagement is another important factor for ankle recovery. Therefore, a multi-input fuzzy logic is constructed for comprehensively assessing ankle recovery. Subsequently, the progressive learning law is proposed for promoting patients' engagement in light of individual training performance.

Extensive studies [14, 17, 25, 40, 80] have demonstrated that active participant is the key to motor recovery. For this purpose, different control strategies are proposed for ankle [47, 65] and upper limb rehabilitation [54, 163, 173] that only provides necessary robot assistance during training. The training performance, i.e., task completion [47, 54, 65] and interaction force [163, 173] are used to determine the quantity of robot assistance. However, individual performance indicator with either kinematic or dynamic measure is not reliable due to individual differences [40, 41]. Besides, existing studies only focus on minimizing the robot tracking error [47, 54, 65], as validated in [53, 163, 173], progressively reducing the robot stiffness can further promote engagement. Therefore, fuzzy logic for online performance evaluation is presented with three quantitative measures include both kinematic and dynamic information. To determine the range of membership functions of the fuzzy system, primary experiments are conducted with a baseline controller. Subsequently, the performance output of fuzzy logic is used to iteratively update the stiffness matrix of the robot. The effect of including a cost function for minimizing both the robot tracking error and stiffness is analysed by Lyapunov method and discussions on control ultimate bounds indicate that improved performance will lead to a large allowable tracking error and maintain a progressively decreasing tendency of the robot stiffness, thus, promoting patients' engagement. Ten healthy subjects are included in the experiments, it was found that the progressive learning strategy can effectively promote subjects' participant. The robot assistance torque is reduced by 22.89 % and active ankle torque is increased by 62.82 %.

9.2 Future Work

9.2.1 Optimization of the CARR

In terms of the mechanical design, the CARR as a prototype leaves some room for optimization. First of all, PMs are currently connected to the moving platform and the fixed platform by cables. In some workspace, the contraction force of the PM cannot be effectively transmitted to the robot joint. To avoid possible instability during training, the spherical hinge is recommended for reconstructing the connection. Secondly, due to the selection of PMs which have an original length of 400 mm, the distance between the moving platform and the fixed platform is relatively large. This leads to the fact that the DoF along Z-axis cannot be effectively obtained in practice. Although individual ankle A/A movement is not recommended in ankle rehabilitation [1, 7], some joint movements, such as pronation and supination, require control feasibility along the Z-axis. Finally, the reconfigurability of the CARR needs to be considered. Although the CARR can be adjusted to fit patients with different heights and leg lengths, the PM connections on the fixed and moving platform should also be reconfigurable. In that case, the workspace and torque generation of the CARR can be varied for specific training scenarios.

9.2.2 Convergence Speed of the DDAILC

Convergence speed is one of the most important factors in the ILC design. In terms of its implementation on the CARR, the convergence speed of the controller is highly related to the number of task repetitions. As shown in Chapter 4, the DDAILC requires 5 iterations to converge the tracking error to the baseline (PID) and 10 iterations are needed for a converged tracking error. A faster convergence speed can provide the controller with more feasibilities on different rehabilitation scenarios. Therefore, there are two possible ways for speeding up the convergence of the DDAILC and can be considered as future work. Firstly, DDAILC can be incorporated with a baseline controller which has a relatively stable and accurate tracking performance. A switchable control structure can be established that utilizes the control results of the baseline controller during the first few iterations, while the follow-on control tasks will be handled by the DDAILC. Alternatively, some high-order algorithms can be designed for constructing the cost function (4.7) as follow

$$J(p_{i,k}(t), \alpha) = |\sum_{m=1}^{M} \alpha_m (l_i^*(t) - l_{i,k-m+1}(t+1))|^2 + \lambda |p_{i,k}(t) - p_{i,k-1}(t)|^2 \tag{9.1}$$

where M is a positive integer and $\alpha_m \in (0, 1]$ contains the factors that determine the weight of tracking error in previous $M - 1$ iterations. Due to the usage of high-order tracking error that comes from earlier iterations, it is expected that the algorithm will have a faster convergence speed. Note that the memory size and computational efficiency have to be considered for constructing such high-order ILC scheme.

9.2.3 Universality of the RCILC and integral-type BLF

In Chapter 5, RCILC relaxes the GLC condition on nonparametric uncertainties by LLC condition. In practice, except the friction that has been considered in current design, there are two other types of nonparametric uncertainties [187], i.e.,

- Norm-bounded by a known function $\rho(x, t)$: $\|\eta(x_1, x_2, t)\|_2 \leq \rho(x_1, x_2, t)$
- Norm-bounded with unknown coefficient φ: $\|\eta(x_1, x_2, t)\|_2 \leq \varphi\rho(x_1, x_2, t)$

Moreover, the uncertainties raised by iteration-dependent terms are not considered as well. To make the controller more universal, different types of uncertainty and its iteration-dependent variations have to be considered in the practical usage of PMs.

Besides, an error-based BLF is used to restrict the PM states in Chapter 5. Although its effectiveness has been verified via experiments, theoretically, the control law is conservative due to the specified error bounds $k_{c,1}$ and $k_{c,2}$. Some new results on the integral-type BLF [188, 189] that directly deal with system constraints by restricting corresponding states are worthy of further study.

9.2.4 Impedance learning for Resistance Training

For the impedance learning controller, the open parameters α_B, α_K and the weight matrix $C(t)$ have significant effects on the entire learning process. Further studies should focus on parameter tuning and experimental validations with different weight matrices. Furthermore, due to the individual differences, the impedance learning controller with unoptimized parameters have unpredictable performance on different subjects. Although for healthy subjects, as verified in Chapter 6, have similar passive torque during movement, it still requires a suitable training task for the specific usage of the impedance learning scheme. Resistance training is suggested for further study, while an achievable interaction force can be specified along the whole training process. The interactive torque can be monitored and feedback to the users, while the training interface can be used to represent the task as same as Chapter 7.

9.2.5 Optimization of the Progressive Learning Scheme

Along with promoted participant, human motor adaption [42] is an important factor during training. A slight lack of concentration of subjects may let the robot controller take over the performance of the training. Therefore, the overall weight factor P_c can also be adapted for adjusting the challenge level of training. To avoid unreliable decisions made by single-trial performance, a multiple trials based challenge level adaption can be considered as the future work, such as

$$P_i = \begin{cases} P_1 \\ P_2 \\ \vdots \\ P_n \end{cases} \quad \rightarrow \quad \chi = f(\sum_{1}^{k} P_k, P^*) \quad \rightarrow \quad P_{c,adapted} = g(\chi) \tag{9.2}$$

where k is the selected trial number and P^* is the normalized performance within k trials. The function $f(\cdot)$ and $g(\cdot)$ are designed for determine the challenge level over k trials and adapt the new weight $P_{c,adapted}$. Besides, the designed fuzzy membership function should be adapted with individual training results. Therefore, future work will also be focus on the establishment of the database which only requires the maximum and minimum values of three selected indicators.

9.3 Summary

This chapter summarises the major outcomes and contributions achieved in this research, and points out some potential work that can be further explored. In general, this research goes into the effectiveness and feasibility of the ILC-based control strategies in conducting ankle rehabilitation. The major contributions are 1) designing the CARR prototype for effective ankle treatment; 2) proposing ILC-based schemes for improving the tracking accuracy, control robustness and training safety during ankle ROMs training and 3) exploring the impedance learning scheme and progressive leaning framework for enhancing the interaction performance and active engagement from patients during ankle strength training. Endows ARR with capabilities of gradual error correction and automatic assistance level modification, the burden on the therapist could be further reduced and the full-automated ankle rehabilitation could be in the near future.

Appendix A

Ethical Approval for Human-involved Studies

The Secretariat
University of Leeds
Leeds, LS2 9JT
Tel: 0113 3434873
Email: ResearchEthics@leeds.ac.uk

UNIVERSITY OF LEEDS

Qian Kun
School of Electronic and Electrical Engineering
University of Leeds
Leeds, LS2 9JT

MaPS and Engineering joint Faculty Research Ethics Committee (MEEC FREC)
University of Leeds

30 November 2021

Dear Qian Kun

Title of study **Three dimensional ankle functional assessment via motion capture system and sensors.**
Ethics reference **MEEC 18-001**

I am pleased to inform you that the application listed above has been reviewed by the MaPS and Engineering joint Faculty Research Ethics Committee (MEEC FREC) and following receipt of your response to the Committee's initial comments, I can confirm a favourable ethical opinion as of the date of this letter. The following documentation was considered:

Document	Version	Date
MEEC 18-001 Application_Form_Kun_Qian_V1.2.doc	4	12/11/2018
MEEC 18-001 Recruitment_emails_example_Kun_Qian_V1.1.docx	1	12/11/2018
MEEC 18-001 Participant_Information_Sheet_Kun_Qian_V1.1.doc	1	13/08/2018
MEEC 18-001 Participant_consent_form_Kun_Qian_V1.1.doc	1	13/08/2018

Please notify the committee if you intend to make any amendments to the information in your ethics application as submitted at date of this approval as all changes must receive ethical approval prior to implementation. The amendment form is available at http://ris.leeds.ac.uk/EthicsAmendment.

Please note: You are expected to keep a record of all your approved documentation and other documents relating to the study, including any risk assessments. This should be kept in your study file, which should be readily available for audit purposes. You will be given a two week notice period if your project is to be audited. There is a checklist listing examples of documents to be kept which is available at http://ris.leeds.ac.uk/EthicsAudits.

We welcome feedback on your experience of the ethical review process and suggestions for improvement. Please email any comments to ResearchEthics@leeds.ac.uk.

Yours sincerely

Jennifer Blaikie
Senior Research Ethics Administrator, the Secretariat
On behalf of Dr Dawn Groves, Chair, MEEC FREC

CC: Student's supervisor(s)

Figure A.1: Approval of School Ethic Committee (Reference MEEC 18-001).

Appendix B

List of Materials

Functionality	Components	Specification	Quantity
Actuation	PM	Festo DMSP-20-400N-RM-CM	4
	PPR	Festo VPPM-6L-L-1-G18- 0L6H	4
Sensing	Rotary encoder (position)	AS5048A	3
	Single-axis load cell (force)	Futek LCM 300 250Ib	4
		Futek CSG110 amplifier	4
	Six-axis load cell (force)	ATI Omega85	1
		ATI 9105-DAQ	1
Control	Real-time controller	NI Compact RIO-9022	1
	Signal I/O	Digital I/O NI-9401	1
		Analog Input NI-9205	1
		Analog Output NI-9263	1
		Synchronization NI USB-6210	1

Bibliography

[1] Jody A Saglia, Nikos G Tsagarakis, et al. Control strategies for patient-assisted training using the ankle rehabilitation robot (ARBOT). *IEEE/ASME Trans. Mechatron.*, 18(6):1799–1808, 2012.

[2] Anatomical planes, medicine 107. Available at: https://medicine107.wordpress.com/2014/12/24/anatomical-planes/, 2014.

[3] Ge Wu, Sorin Siegler, Paul Allard, and Chris Kirtley. ISB recommendation on definitions of joint coordinate system of various joints for the reporting of human joint motion-part i: ankle, hip, and spine. *J. Biomech.*, 35(4):543–548, 2002.

[4] Ankle rehabilitation stage 1 and 2 by oxford university hospitals. Available at: https://www.ouh.nhs.uk, 2014.

[5] Judith E Deutsch, Jason Latonio, et al. Post-stroke rehabilitation with the rutgers ankle system: a case study. *Presence: Teleoperators & Virtual Environments*, 10 (4):416–430, 2001.

[6] Daniel P Ferris, Joseph M Czerniecki, and Blake Hannaford. An ankle-foot orthosis powered by artificial pneumatic muscles. *J. Appl. Biomech.*, 21(2):189–197, 2005.

[7] Anindo Roy, Hermano Igo Krebs, et al. Robot-aided neurorehabilitation: a novel robot for ankle rehabilitation. *IEEE Trans. Robot.*, 25(3):569–582, 2009.

[8] Ahmetcan Erdogan, Besir Celebi, et al. ASSISTON-ANKLE: a reconfigurable ankle exoskeleton with series-elastic actuation. *Auton. Robots*, 41(3):743–758, 2017.

[9] Haoyong Yu, Sunan Huang, et al. Human-robot interaction control of rehabilitation robots with series elastic actuators. *IEEE Trans. on Robotics*, 31(5): 1089–1100, 2015.

[10] Sorin Siegler, Jie Chen, et al. The three-dimensional kinematics and flexibility characteristics of the human ankle and subtalar jointsâ€”part i: Kinematics. 1988.

[11] Chantal S Parenteau, David C Viano, et al. Biomechanical properties of human cadaveric ankle-subtalar joints in quasi-static loading. 1998.

[12] Mingming Zhang, Jinghui Cao, et al. Reconfigurable workspace and torque capacity of a compliant ankle rehabilitation robot (CARR). *Robot. Auton. Syst.*, 98:213–221, 2017.

[13] Philip Procter and JP Paul. Ankle joint biomechanics. *J. Biomech.*, 15(9):627–634, 1982.

[14] Marian G Alvarez-Perez, Mario A Garcia-Murillo, et al. Robot-assisted ankle rehabilitation: a review. *Disabil. rehabilitation. Assist. Technol.*, 15(4):394–408, 2020.

[15] National Health Service. Therapeutic ultrasound for acute ankle sprains-NHS evidance. Available at: https://arms.evidence.nhs.uk, 2013.

[16] State of the Nation 2018 by Stroke Association. Available at: https://www.stroke.org.uk, 2018.

[17] Bleakley and Chris M. Effect of accelerated rehabilitation on function after ankle sprain: randomised controlled trial. *Bmj*, 340, 2010.

[18] Inaki Diaz, Jorge Juan Gil, et al. Lower-limb robotic rehabilitation: literature review and challenges. *J. Robot.*, 2011, 2011.

[19] Mingming Zhang, T Claire Davies, et al. Effectiveness of robot-assisted therapy on ankle rehabilitation-a systematic review. *J. NeuroEng. Rehabil.*, 10(1):1–16, 2013.

[20] Pawel Maciejasz, Jorg Eschweiler, Kurt Gerlach-Hahn, Arne Jansen-Troy, and Steffen Leonhardt. A survey on robotic devices for upper limb rehabilitation. *JNER*, 11(1):1–29, 2014.

[21] OM Rutherford and DA Jones. The role of learning and coordination in strength training. *Eur. J. Appl. Physiol.*, 55(1):100–105, 1986.

[22] Philip D Chilibeck, Aaron W Calder, et al. A comparison of strength and muscle mass increases during resistance training in young women. *Eur. J. Appl. Physiol.*, 77(1):170–175, 1997.

[23] Qing Miao, Mingming Zhang, et al. Towards optimal platform-based robot design for ankle rehabilitation: The state of the art and future prospects. *J. Healthc. Eng.*, 2018, 2018.

[24] Li-Qun Zhang and William Zev Rymer. Simultaneous and nonlinear identification of mechanical and reflex properties of human elbow joint muscles. *IEEE. Trans. Biomed. Eng.*, 44(12):1192–1209, 1997.

[25] Laura Marchal-Crespo and David J Reinkensmeyer. Review of control strategies for robotic movement training after neurologic injury. *J. Neuroeng. Rehabil.*, 6 (1):1–15, 2009.

[26] Shou-Han Zhou, Justin Fong, et al. Learning control in robot-assisted rehabilitation of motor skills-a review. *J. Control. Decis*, 3(1):19–43, 2016.

[27] Carl G Mattacola and Maureen K Dwyer. Rehabilitation of the ankle after acute sprain or chronic instability. *J. Athl. Train.*, 37(4):413, 2002.

[28] Mindy Lipson Aisen, H Igo Krebs, et al. The effect of robot-assisted therapy and rehabilitative training on motor recovery following stroke. *Arch. Neurol.*, 54(4): 443–446, 1997.

[29] Zhihao Zhou, Yuan Zhou, et al. A proprioceptive neuromuscular facilitation integrated robotic ankle-foot system for post stroke rehabilitation. *Robot. Auton. Syst.*, 73:111–122, 2015.

[30] You-jou Hung. Neuromuscular control and rehabilitation of the unstable ankle. *World J. Orthop.*, 6(5):434, 2015.

[31] Li-Qun Zhang, Sun G Chung, et al. Intelligent stretching of ankle joints with contracture/spasticity. *IEEE Trans. Neural Syst. Rehabil. Eng.*, 10(3):149–157, 2002.

[32] Giuseppe Bucca, Alberto Bezzolato, et al. A mechatronic device for the rehabilitation of ankle motor function. *J. Biomech. Eng.*, 131(12), 2009.

[33] Jan F Veneman, Ralf Ekkelenkamp, et al. A series elastic-and bowden-cable-based actuation system for use as torque actuator in exoskeleton-type robots. *Int. J. Rob. Res.*, 25(3):261–281, 2006.

[34] Sheng Quan Xie and Prashant Kumar Jamwal. An iterative fuzzy controller for pneumatic muscle driven rehabilitation robot. *Expert Syst. Appl.*, 38(7):8128–8137, 2011.

[35] Wei Meng, Sheng Quan Xie, et al. Robust iterative feedback tuning control of a compliant rehabilitation robot for repetitive ankle training. *IEEE/ASME Trans Mechatron.*, 22(1):173–184, 2016.

[36] Mingming Zhang, Sheng Q Xie, et al. Adaptive patient-cooperative control of a compliant ankle rehabilitation robot (CARR) with enhanced training safety. *IEEE Trans. Ind. Electron.*, 65(2):1398–1407, 2017.

[37] Chitranjan S Ranawat, Amar S Ranawat, et al. Total knee arthroplasty rehabilitation protocol: Whatmakes the difference? *J. Arthroplasty*, 18(3):27–30.

[38] Roger M Enoka. *Neuromechanics of human movement.* 2008.

[39] Barbro B Johansson. Brain plasticity and stroke rehabilitation: the willis lecture. *Stroke*, 31(1):223–230, 2000.

[40] H Igo Krebs, Neville Hogan, et al. Robot-aided neurorehabilitation. *IEEE Trans. Neural Syst. Rehabil. Eng.*, 6(1):75–87, 1998.

[41] David Joyce and D Lewindon. Sports injury prevention and rehabilitation. page 2016, 2015.

[42] Jeremy L Emken, Susan J Harkema, et al. Feasibility of manual teach-and-replay and continuous impedance shaping for robotic locomotor training following spinal cord injury. *IEEE. Trans. Biomed. Eng.*, 55(1):322–334, 2007.

[43] James Arnold and Hyunglae Lee. Variable impedance control for phri: Impact on stability, agility, and human effort in controlling a wearable ankle robot. *IEEE Robot. Autom. Lett.*, 6(2):2429–2436, 2021.

[44] Prashant K Jamwal, Sheng Q Xie, et al. An adaptive wearable parallel robot for the treatment of ankle injuries. *IEEE ASME Trans Mechatron.*, 19(1):64–75, 2012.

[45] Hyunglae Lee and Neville Hogan. Time-varying ankle mechanical impedance during human locomotion. *IEEE Trans. Neural Syst. Rehabil. Eng.*, 23(5):755–764, 2014.

[46] Prashant K Jamwal, Shahid Hussain, et al. Impedance control of an intrinsically compliant parallel ankle rehabilitation robot. *IEEE Trans. Ind. Electron.*, 63(6):3638–3647, 2016.

[47] Mingming Zhang, Andrew McDaid, et al. Adaptive trajectory tracking control of a parallel ankle rehabilitation robot with joint-space force distribution. *IEEE Access*, 7:85812–85820, 2019.

[48] John W Krakauer. Motor learning: its relevance to stroke recovery and neurorehabilitation. *Curr. Opin. Neurol.*, 19(1):84–90, 2006.

[49] Lisa M Muratori, Eric M Lamberg, et al. Applying principles of motor learning and control to upper extremity rehabilitation. *J. Hand Ther.*, 26(2):94–103, 2013.

[50] Nancy H McNevin, Gabriele Wulf, et al. Effects of attentional focus, self-control, and dyad training on motor learning: implications for physical rehabilitation. *Phys. Ther.*, 80(4):373–385, 2000.

[51] Gergory T Thielman, Catherine M Dean, et al. Rehabilitation of reaching after stroke: task-related training versus progressive resistive exercise. *Arch. Phys. Med. Rehabil.*, 85(10):1613–1618, 2004.

[52] Yuanjie Fan and Yuehong Yin. Active and progressive exoskeleton rehabilitation using multisource information fusion from EMG and force-position epp. *IEEE. Trans. Biomed. Eng.*, 60(12):3314–3321.

[53] Hermano Igo Krebs, Jerome Joseph Palazzolo, et al. Rehabilitation robotics: Performance-based robot-assisted therapy. *Auton. Robots*, 15(1):7–20, 2003.

[54] Ali Utku Pehlivan, Dylan P Losey, and Marcia K O'Malley. Minimal assist-as-needed controller for upper limb robotic rehabilitation. *IEEE Trans. Robot.*, 32 (1):113–124, 2015.

[55] Jean-Jacques E Slotine, Weiping Li, et al. *Applied nonlinear control*, volume 199. 1991.

[56] Zhongbo Sun, Feng Li, et al. An adaptive iterative learning control approach for lower limb rehabilitation robot in noisy environments. In *2019 IEEE 9th Annual*

International Conference on CYBER Technology in Automation, Control, and Intelligent Systems (CYBER), pages 905–910, 2019.

[57] Vincent S Huang and John W Krakauer. Robotic neurorehabilitation: a computational motor learning perspective. *J. NeuroEng. Rehabil.*, 6(1):1–13, 2009.

[58] Beverley French, Lois H Thomas, et al. Repetitive task training for improving functional ability after stroke. *Cochrane Database Syst. Rev.*, (11), 2016.

[59] Gert Kwakkel, Roland van Peppen, et al. Effects of augmented exercise therapy time after stroke: a meta-analysis. *stroke*, 35(11):2529–2539, 2004.

[60] Leonard E Kahn, Michele L Zygman, et al. Robot-assisted reaching exercise promotes arm movement recovery in chronic hemiparetic stroke: a randomized controlled pilot study. *J. NeuroEng. Rehabil.*, 3(1):1–13, 2006.

[61] Anindo Roy, Hermano I Krebs, et al. Measurement of passive ankle stiffness in subjects with chronic hemiparesis using a novel ankle robot. *J. Neurophysiol.*, 105(5):2132–2149, 2011.

[62] Vijaykumar Rajasekaran, Joan Aranda, et al. An adaptive control strategy for postural stability using a wearable robot. *Robot. Auton. Syst.*, 73:16–23, 2015.

[63] Victor Arnez-Paniagua, Hala Rifai, et al. Adaptive control of an actuated ankle foot orthosis for foot-drop correction. *IFAC-PapersOnLine*, 50(1):1384–1389, 2017.

[64] R Lopez-Gutierrez, H Aguilar-Sierra, et al. Adaptive control in passive rehabilitation routines using ELLTIO. *Rev. Mex. Ing. Biomed.*, 38(2):458–478, 2017.

[65] Juan C Perez-Ibarra, Adriano AG Siqueira, et al. Adaptive impedance control applied to robot-aided neuro-rehabilitation of the ankle. *IEEE Robot. Autom. Lett.*, 4(2):185–192, 2018.

[66] Weiguang Huo, Victor Arnez-Paniagua, et al. Adaptive proxy-based controller of an active ankle foot orthosis to assist lower limb movements of paretic patients. *Robotica*, 37(12):2147–2164, 2019.

[67] Qingsong Ai, Chengxiang Zhu, et al. Disturbance-estimated adaptive backstepping sliding mode control of a pneumatic muscles-driven ankle rehabilitation robot. *Sensors*, 18(1):66, 2018.

[68] Barkan Ugurlu, Corinne Doppmann, et al. Variable ankle stiffness improves balance control: Experiments on a bipedal exoskeleton. *IEEE/ASME Trans. Mechatron.*, 21(1):79–87, 2015.

[69] Wei Sun, Jhih-Wei Lin, et al. Reduced adaptive fuzzy decoupling control for lower limb exoskeleton. *IEEE Trans. Cybern.*, 51(3):1099–1109, 2020.

[70] Kaiyang Yin, Muye Pang, et al. Fuzzy iterative learning control strategy for powered ankle prosthesis. *Int. J. Intell. Robot.*, 2(1):122–131, 2018.

[71] Mustafa Sinasi Ayas, Ismail Hakki Altas, et al. Fractional order based trajectory tracking control of an ankle rehabilitation robot. *Trans. Inst. Meas. Control*, 40 (2):550–564, 2018.

[72] Jeffrey R Koller, Daniel A Jacobs, et al. Learning to walk with an adaptive gain proportional myoelectric controller for a robotic ankle exoskeleton. *J. Neuroeng. Rehabil.*, 12(1):1–14, 2015.

[73] Thomas Seel, Cordula Werner, and pthers. Iterative learning control of a drop foot neuroprosthesisâ€”generating physiological foot motion in paretic gait by automatic feedback control. *Control Eng. Pract.*, 48:87–97, 2016.

[74] Renquan Lu, Zhijun Li, et al. Development and learning control of a human limb with a rehabilitation exoskeleton. *IEEE Trans. Ind. Electron.*, 61(7):3776–3785, 2013.

[75] Fares J Abu-Dakka, Angel Valera, Juan A Escalera, Mohamed Abderrahim, Alvaro Page, and Vicente Mata. Passive exercise adaptation for ankle rehabilitation based on learning control framework. *Sensors*, 20(21):6215, 2020.

[76] Niall Maclean, Pandora Pound, et al. A critical review of the concept of patient motivation in the literature on physical rehabilitation. *Soc. Sci. Med.*, 50(4): 495–506, 2000.

[77] Ann M Simon, R Brent Gillespie, et al. Symmetry-based resistance as a novel means of lower limb rehabilitation. *J. Biomech.*, 40(6):1286–1292, 2007.

[78] Heike Vallery, Edwin HF Van Asseldonk, et al. Reference trajectory generation for rehabilitation robots: complementary limb motion estimation. *IEEE Trans. Neural Syst. Rehabil. Eng.*, 17(1):23–30, 2008.

[79] Bram Koopman, Edwin HF Van Asseldonk, et al. Selective control of gait subtasks in robotic gait training: foot clearance support in stroke survivors with a powered exoskeleton. *J. Neuroeng. Rehabil.*, 10(1):1–21, 2013.

[80] Prashant K Jamwal, Shahid Hussain, et al. Musculoskeletal model for path generation and modification of an ankle rehabilitation robot. *IEEE Trans. Hum. Mach. Syst.*, 50(5):373–383, 2020.

[81] Di Ao, Rong Song, et al. Movement performance of human-robot cooperation control based on EMG-driven hill-type and proportional models for an ankle power-assist exoskeleton robot. *IEEE Trans. Neural Syst. Rehabil. Eng.*, 25(8): 1125–1134, 2016.

[82] Quan Liu, Aiming Liu, Wei Meng, et al. Hierarchical compliance control of a soft ankle rehabilitation robot actuated by pneumatic muscles. *Front. Neurorobot.*, 11:64, 2017.

[83] Ronald N Goodman, Jeremy C Rietschel, et al. Increased reward in ankle robotics

training enhances motor control and cortical efficiency in stroke. *J. Rehabil. Res. Dev.*, 51(2).

[84] Grigore C Burdea, Daniel Cioi, et al. Robotics and gaming to improve ankle strength, motor control, and function in children with cerebral palsyâ€”a case study series. *IEEE Trans. Neural Syst. Rehabil. Eng.*, 21(2):165–173, 2012.

[85] Larry W Forrester, Anindo Roy, et al. Task-specific ankle robotics gait training after stroke: a randomized pilot study. *J. Neuroeng. Rehabil.*, 13(1):1–6, 2016.

[86] Neville Hogan. Impedance control: An approach to manipulation: Part iâ€”theory. 1985.

[87] Mark W Spong and Mathukumalli Vidyasagar. *Robot dynamics and control.* 2008.

[88] Morikazu Takegaki and Suguru Arimoto. A new feedback method for dynamic control of manipulators. 1981.

[89] Hyunglae Lee, Elliott J Rouse, et al. Summary of human ankle mechanical impedance during walking. *IEEE J. Transl. Eng. Health Med.*, 4:1–7, 2016.

[90] Jonas Buchli, Freek Stulp, et al. Learning variable impedance control. *Int. J. Rob. Res.*, 30(7):820–833, 2011.

[91] Fanny Ficuciello, Luigi Villani, et al. Variable impedance control of redundant manipulators for intuitive human-robot physical interaction. *IEEE Trans. Robot.*, 31(4):850–863, 2015.

[92] Mojtaba Sharifi, Amir Zakerimanesh, et al. Impedance variation and learning strategies in human-robot interaction. *IEEE Trans. Cybern.*, 2021. doi: 10.1109/TCYB.2020.3043798.

[93] John J Craig. *Introduction to robotics: mechanics and control, 3/E.* 2009.

[94] Quan Liu, Jie Zuo, et al. Design and control of soft rehabilitation robots actuated by pneumatic muscles: State of the art. *Future Gener. Comput. Syst.*, 113:620–634, 2020.

[95] Lijun Zhu, Xianyi Shi, et al. Adaptive servomechanism of pneumatic muscle actuators with uncertainties. *IEEE Trans. Ind. Electron.*, 64(4):3329–3337, 2016.

[96] Daohui Zhang, Xingang Zhao, et al. Active model-based control for pneumatic artificial muscle. *IEEE Trans. Ind. Electron.*, 64(2):1686–1695, 2016.

[97] Jun Wu, Jian Huang, et al. Nonlinear disturbance observer-based dynamic surface control for trajectory tracking of pneumatic muscle system. *IEEE Trans. Control Syst. Technol.*, 22(2):440–455, 2013.

[98] Yu Cao, Jian Huang, et al. Adaptive proxy-based robust control integrated with nonlinear disturbance observer for pneumatic muscle actuators. *IEEE/ASME Trans. Mechatron.*, 25(4):1756–1764, 2020.

[99] D. P. Romilly, C. Anglin, et al. A functional task analysis and motion simulation for the development of a powered upper-limb orthosis. *IEEE Trans. Neural Syst. Rehabil. Eng.*, 2(3):119–129, 1994.

[100] Jinghui Cao, Sheng Quan Xie, et al. Mimo sliding mode controller for gait exoskeleton driven by pneumatic muscles. *IEEE Trans. Control Syst. Technol.*, 26 (1):274–281, 2017.

[101] Douglas A Bristow, Marina Tharayil, et al. A survey of iterative learning control. *IEEE Control Syst. Magazine*, 26(3):96–114, 2006.

[102] Chris T Freeman, A-M Hughes, et al. Iterative learning control of fes applied to the upper extremity for rehabilitation. *Control Eng. Pract.*, 17(3):368–381, 2009.

[103] Christopher T Freeman. Upper limb electrical stimulation using input-output linearization and iterative learning control. *IEEE Trans. Control Syst. Technol.*, 23(4):1546–1554, 2014.

[104] Wenkang Xu, Bing Chu, et al. Iterative learning control for robotic-assisted upper limb stroke rehabilitation in the presence of muscle fatigue. *Control Eng. Pract.*, 31:63–72, 2014.

[105] Sivakumar Balasubramanian, Ruihua Wei, et al. RUPERT: An exoskeleton robot for assisting rehabilitation of arm functions. In *2008 virtual rehabilitation*, pages 163–167, 2008.

[106] Qing Miao, Ho Shing Lo, et al. Iterative learning control method for improving the effectiveness of upper limb rehabilitation. In *2016 23rd International Conference on Mechatronics and Machine Vision in Practice (M2VIP)*, pages 1–5, 2016.

[107] Xuefeng Zhu, Jianhui Wang, et al. Nonlinear iterative learning control of 5 dof upper-limb rehabilitation robot. In *2015 IEEE International Conference on Robotics and Biomimetics (ROBIO)*, pages 793–798, 2015.

[108] Xuhui Bu, Qiongxia Yu, et al. Model free adaptive iterative learning consensus tracking control for a class of nonlinear multiagent systems. *IEEE Trans. Syst. Man*, 49(4):677–686, 2017.

[109] Zhanshan Wang, Lei Liu, et al. Neural network-based model-free adaptive fault-tolerant control for discrete-time nonlinear systems with sensor fault. *IEEE Trans. Syst. Man*, 47(8):2351–2362.

[110] Xiangnan Zhong, Haibo He, et al. Model-free adaptive control for unknown nonlinear zero-sum differential game. *IEEE Trans. Cybern.*, 48(5):1633–1646, 2017.

[111] Ronghu Chi, Yu Hui, et al. Discrete-time extended state observer-based model-free adaptive control via local dynamic linearization. *IEEE Trans. Ind. Electron.*, 67(10):8691–8701, 2019.

[112] Abdellatif Demnati and JNK Rao. Linearization variance estimators for survey data. *Surv. Methodol.*, 30(1):17–26, 2004.

[113] Bernard Charlet, Jean Levine, et al. On dynamic feedback linearization. *IEEE Control Syst. Lett.*, 13(2):143–151, 1989.

[114] Denis Dochain, Jean-Pierre Babary, et al. Modelling and adaptive control of non-linear distributed parameter bioreactors via orthogonal collocation. *Automatica*, 28(5):873–883.

[115] Jian Huang, Yu Cao, et al. An echo state gaussian process-based nonlinear model predictive control for pneumatic muscle actuators. *IEEE Trans. Autom. Sci. Eng.*, 16(3):1071–1084, 2018.

[116] Pamela W Duncan, Larry B Goldstein, et al. Similar motor recovery of upper and lower extremities after stroke. *Stroke*, 25(6):1181–1188, 1994.

[117] Qingsong Ai, Da Ke, et al. High-order model-free adaptive iterative learning control of pneumatic artificial muscle with enhanced convergence. *IEEE Trans. Ind. Electron.*, 67(11):9548–9559, 2019.

[118] Ching-Ping Chou and Blake Hannaford. Measurement and modeling of mckibben pneumatic artificial muscles. *IEEE Robot. Autom. Lett.*, 12(1):90–102, 1996.

[119] Marc Doumit, Atef Fahim, et al. Analytical modeling and experimental validation of the braided pneumatic muscle. *IEEE Trans. Robot.*, 25(6):1282–1291, 2009.

[120] Bertrand Tondu. Modelling of the mckibben artificial muscle: A review. *J. Intell. Mater. Syst. Struct.*, 23(3):225–253, 2012.

[121] Darwin G Caldwell, Gustavo A Medrano-Cerda, et al. Control of pneumatic muscle actuators. *IEEE Control Syst.*, 15(1):40–48, 1995.

[122] Robb W Colbrunn, Gabriel M Nelson, et al. Modeling of braided pneumatic actuators for robotic control. In *Proceedings 2001 IEEE/RSJ International Conference on Intelligent Robots and Systems. Expanding the Societal Role of Robotics in the the Next Millennium*, volume 4, pages 1964–1970, 2001.

[123] DBa Reynolds, DWb Repperger, CAa Phillips, et al. Modeling the dynamic characteristics of pneumatic muscle. *Annu. Rev. Biomed. Eng.*, 31(3):310–317, 2003.

[124] Ning Sun, Dingkun Liang, et al. Adaptive control for pneumatic artificial muscle systems with parametric uncertainties and unidirectional input constraints. *IEEE Trans. Ind. Inform.*, 16(2):969–979, 2019.

[125] JL Serres, DB Reynolds, et al. Characterisation of a phenomenological model for commercial pneumatic muscle actuators. *Comput. Methods Biomech. Biomed. Eng.*, 12(4):423–430, 2009.

[126] Dominik Schindele and Harald Aschemann. Ilc for a fast linear axis driven by pneumatic muscle actuators. In *2011 IEEE International Conference on Mechatronics*, pages 967–972. IEEE, 2011.

[127] George Andrikopoulos, George Nikolakopoulos, et al. Piecewise affine modeling and constrained optimal control for a pneumatic artificial muscle. *IEEE Trans. Ind. Electron.*, 61(2):904–916, 2013.

[128] Suguru Arimoto, Sadao Kawamura, et al. Bettering operation of robots by learning. *J. Robot. Syst.*, 1(2):123–140, 1984.

[129] Abdelhamid Tayebi. Adaptive iterative learning control for robot manipulators. *Automatica*, 40(7):1195–1203, 2004.

[130] Sadeq Ali Qasem Mohammed, Anh Tuan Nguyen, et al. Improved iterative learning control strategy for surface-mounted permanent magnet synchronous motor drives. *IEEE Trans. Ind. Electron.*, 67(12):10134–10144, 2020.

[131] Jian-Xin Xu and Jing Xu. On iterative learning from different tracking tasks in the presence of time-varying uncertainties. *IEEE Trans. Syst. Man Cybern.*

[132] Yong-Lae Park, Bor-rong Chen, et al. Design and control of a bio-inspired soft

wearable robotic device for ankle-foot rehabilitation. *Bioinspir. Biomim.*, 9(1): 016007, 2014.

[133] Keng Peng Tee, Shuzhi Sam Ge, et al. Barrier lyapunov functions for the control of output-constrained nonlinear systems. *Automatica*, 45(4):918–927, 2009.

[134] Xu Jin. Iterative learning control for non-repetitive trajectory tracking of robot manipulators with joint position constraints and actuator faults. *Int. J. Adapt. Control Signal Process.*, 31(6):859–875, 2017.

[135] Ivan Stephen Sokolnikoff, Raymond M Redheffer, et al. Mathematics of physics and modern engineering. *J. Electrochem. Soc.*, 105(9):196C, 1958.

[136] Melih Turkseven and Jun Ueda. Model-based force control of pneumatic actuators with long transmission lines. *IEEE/ASME Trans. Mechatron.*, 23(3):1292–1302, 2018.

[137] Yuan Yuan, Yang Yu, et al. Nonlinear active disturbance rejection control for the pneumatic muscle actuators with discrete-time measurements. *IEEE Trans. Ind. Electron.*, 66(3):2044–2053, 2018.

[138] Ronghu Chi, Xiaohe Liu, et al. Constrained data-driven optimal iterative learning control. *J. Process Control*, 55:10–29, 2017.

[139] Mircea-Bogdan Radac and Radu-Emil Precup. Model-free constrained data-driven iterative reference input tuning algorithm with experimental validation. *Int. J. Gen. Syst.*, 45(4):455–476, 2016.

[140] Chris T Freeman and Ying Tan. Iterative learning control with mixed constraints for point-to-point tracking. *IEEE Trans. Control Syst. Technol.*, 21(3):604–616, 2012.

[141] Richard W Longman. Iterative learning control and repetitive control for engineering practice. *Int. J. Control*, 73(10):930–954, 2000.

[142] Alexander Duschau-Wicke, Joachim Von Zitzewitz, et al. Path control: a method for patient-cooperative robot-aided gait rehabilitation. *IEEE Trans. Neural Syst. Rehabil. Eng.*, 18(1):38–48, 2009.

[143] Kian Jalaleddini, Ehsan Sobhani Tehrani, et al. A subspace approach to the structural decomposition and identification of ankle joint dynamic stiffness. *IEEE. Trans. Biomed. Eng.*, 64(6):1357–1368, 2016.

[144] Stephen P Buerger and Neville Hogan. Complementary stability and loop shaping for improved human-robot interaction. *IEEE Trans. Robot.*, 23(2):232–244, 2007.

[145] Federica Ferraguti, Nicola Preda, et al. An energy tank-based interactive control architecture for autonomous and teleoperated robotic surgery. *IEEE Trans. Robot.*, 31(5):1073–1088, 2015.

[146] Chenguang Yang, Guangzhu Peng, et al. Neural networks enhanced adaptive admittance control of optimized robot-environment interaction. *IEEE Trans. Cybern.*, 49(7):2568–2579, 2018.

[147] Elaheh Arefinia, Heidar Ali Talebi, et al. A robust adaptive model reference impedance control of a robotic manipulator with actuator saturation. *IEEE Trans. Syst. Man*, 50(2):409–420, 2017.

[148] Lin Liu, Steffen Leonhardt, et al. Impedance-controlled variable stiffness actuator for lower limb robot applications. *IEEE Trans. Autom. Sci. Eng.*, 17(2):991–1004, 2019.

[149] Rajiv V Dubey, Tan Fung Chan, et al. Variable damping impedance control of a bilateral telerobotic system. *IEEE Control Syst.*, 17(1):37–45, 1997.

[150] Mustafa Suphi Erden and Aude Billard. Robotic assistance by impedance compensation for hand movements while manual welding. *IEEE Trans. Cybern.*, 46 (11):2459–2472, 2015.

[151] H-P Huang and S-S Chen. Compliant motion control of robots by using variable impedance. *Int. J. Adv. Manuf. Syst.*, 7(6):322–332.

[152] Ali Taherifar, Gholamreza Vossoughi, et al. Optimal target impedance selection of the robot interacting with human. *Adv. Robot.*, 31(8):428–440, 2017.

[153] Hamidreza Modares, Isura Ranatunga, et al. Optimized assistive human-robot interaction using reinforcement learning. *IEEE Trans. Cybern.*, 46(3):655–667, 2015.

[154] Fotios Dimeas and Nikos Aspragathos. Fuzzy learning variable admittance control for human-robot cooperation. In *IROS*, pages 4770–4775, 2014.

[155] Zhijiang Du, Wei Wang, et al. Variable admittance control based on fuzzy reinforcement learning for minimally invasive surgery manipulator. *Sensors*, 17(4): 844, 2017.

[156] Boo-Ho Yang and Haruhiko Asada. Progressive learning and its application to robot impedance learning. *IEEE Trans. Neural Netw. Learn. Syst.*, 7(4):941–952, 1996.

[157] Yanan Li and Shuzhi Sam Ge. Impedance learning for robots interacting with unknown environments. *IEEE Trans. Control Syst. Technol.*, 22(4):1422–1432, 2013.

[158] Toshiharu Sugie and Toshiro Ono. An iterative learning control law for dynamical systems. *Automatica*, 27(4):729–732, 1991.

[159] Mahir Hassan and Amir Khajepour. Analysis of bounded cable tensions in cable-actuated parallel manipulators. *IEEE Trans. Robot.*, 27(5):891–900, 2011.

[160] Andreas Pott, Tobias Bruckmann, and Lars Mikelsons. Closed-form force distribution for parallel wire robots. In *Comput. Mech.*, pages 25–34. 2009.

[161] Jingqing Han. From pid to active disturbance rejection control. *IEEE Trans. Ind. Electron.*, 56(3):900–906, 2009.

[162] Allen W Heinemann, David Tulsky, et al. Issues in participation measurement in research and clinical applications. *Arch. Phys. Med. Rehabil.*, 91(9):S72–S76, 2010.

[163] Lincong Luo, Liang Peng, et al. A greedy assist-as-needed controller for upper limb rehabilitation. *IEEE Trans. Neural Netw. Learn. Syst.*, 30(11):3433–3443, 2019.

[164] Louis N Awad, Jaehyun Bae, Kathleen O donnell, et al. A soft robotic exosuit improves walking in patients after stroke. *Sci. Transl. Med.*, 9(400), 2017.

[165] Xiang Li, Yongping Pan, et al. Adaptive human-robot interaction control for robots driven by series elastic actuators. *IEEE Trans. Robot.*, 33(1):169–182, 2016.

[166] Neville Hogan and Hermano I Krebs. Interactive robots for neuro-rehabilitation. *Restor. Neurol. Neurosci.*, 22(3-5):349–358, 2004.

[167] Mustafa Sinasi Ayas and Ismail Hakki Altas. Fuzzy logic based adaptive admittance control of a redundantly actuated ankle rehabilitation robot. *Control Eng. Pract.*, 59:44–54, 2017.

[168] Etienne Burdet, Rieko Osu, et al. The central nervous system stabilizes unstable dynamics by learning optimal impedance. *Nature*, 414(6862):446–449, 2001.

[169] Chenguang Yang, Gowrishankar Ganesh, et al. Human-like adaptation of force and impedance in stable and unstable interactions. *IEEE Trans. Robot.*, 27(5): 918–930, 2011.

[170] Yanan Li, Gowrishankar Ganesh, et al. Force, impedance, and trajectory learning for contact tooling and haptic identification. *IEEE Trans. Robot.*, 34(5):1170–1182, 2018.

[171] Chao Zeng, Chenguang Yang, et al. Bio-inspired robotic impedance adaptation for human-robot collaborative tasks. *Sci. China Inf. Sci.*, 63(7):1–10, 2020.

[172] Juanjuan Zhang and Chien Chern Cheah. Passivity and stability of human-robot interaction control for upper-limb rehabilitation robots. *IEEE Trans. Robot.*, 31 (2):233–245, 2015.

[173] Ran Cao, Long Cheng, et al. Iterative assist-as-needed control with interaction factor for rehabilitation robots. *Sci. China Technol. Sci.*, 64(4):836–846, 2021.

[174] Xiang Li, Yun-Hui Liu, et al. Iterative learning impedance control for rehabilitation robots driven by series elastic actuators. *Automatica*, 90:1–7, 2018.

[175] David J Gladstone, Cynthia J Danells, et al. The fugl-meyer assessment of motor recovery after stroke: a critical review of its measurement properties. *Neurorehabil. Neural Repair*, 16(3):232–240, 2002.

[176] Eugenia Papaleo, Loredana Zollo, et al. Patient-tailored adaptive robotic system for upper-limb rehabilitation. In *2013 IEEE International Conference on Robotics and Automation*, pages 3860–3865, 2013.

[177] Stephen G Lisberger. The neural basis for learning of simple motor skills. *Science*, 242(4879):728–735, 1988.

[178] Zuha Warraich and Jeffrey A Kleim. Neural plasticity: the biological substrate for neurorehabilitation. *Pm&r*, 2(12):S208–S219, 2010.

[179] Zhi Liu and Han-Xiong Li. A probabilistic fuzzy logic system for modeling and control. *IEEE Trans. Fuzzy Syst.*, 13(6):848–859, 2005.

[180] Ebrahim H Mamdani and Sedrak Assilian. An experiment in linguistic synthesis with a fuzzy logic controller. *Int. j. Man-Mach. Stud.*, 7(1):1–13, 1975.

[181] Qing Miao, Zhijun Li, et al. Performance-based iterative learning control for task-oriented rehabilitation: a pilot study in robot-assisted bilateral training. *IEEE Trans. Cogn. Develop. Syst.*, 2021. doi: 10.1109/TCDS.2021.3072096.

[182] Abidemi Bolu Ajiboye and R Fff Weir. A heuristic fuzzy logic approach to emg pattern recognition for multifunctional prosthesis control. *IEEE Trans. Neural Syst. Rehabil. Eng.*, 13(3):280–291, 2005.

[183] Thomas A Runkler. Selection of appropriate defuzzification methods using application specific properties. *IEEE Trans. Fuzzy Syst.*, 5(1):72–79, 1997.

[184] Sutbeyaz S, Yavuzer G, et al. Mirror therapy enhances lower-extremity motor recovery and motor functioning after stroke: A randomized controlled trial. *Arch. Phys. Med. Rehabil.*, 88(5):555–559, 2007.

[185] Congzhe Wang, Yuefa Fang, et al. Multi-objective optimization of a parallel ankle rehabilitation robot using modified differential evolution algorithm. *Chin. J. Mech. Eng.*, 28(4):702–715, 2015.

[186] Yun-Ho Tsoi, Shane Q Xie, and Andrew E Graham. Design, modeling and control of an ankle rehabilitation robot. In *Design and Control of Intelligent Robotic Systems*, pages 377–399. 2009.

[187] Jian-Xin Xu. A survey on iterative learning control for nonlinear systems. *Int. J. Control*, 84(7):1275–1294, 2011.

[188] Fengyi Yuan, Yan-Jun Liu, et al. Adaptive neural consensus tracking control for nonlinear multiagent systems using integral barrier lyapunov functionals. *IEEE Trans. Neural Netw. Learn. Syst.*, 2021. doi: 10.1109/TNNLS.2021.3112763.

[189] Yong-Hua Liu, Yang Liu, et al. Adaptive fuzzy control with global stability guarantees for unknown strict-feedback systems using novel integral barrier lyapunov functions. *IEEE Trans. Syst. Man*, 2021. doi: 10.1109/TSMC.2021.3094975.